BRNO UNIVERSITY OF TECHNOLOGY

VYSOKÉ UČENÍ TECHNICKÉ V BRNĚ

CENTRAL EUROPEAN INSTITUTE OF TECHNOLOGY BUT

STŘEDOEVROPSKÝ TECHNOLOGICKÝ INSTITUT VUT

TOWARDS HIGHLY-DOPED GE AND ZNO NANOWIRES: GROWTH, CHARACTERIZATION AND DOPING LEVEL ANALYSIS

VYSOCE DOPOVANÁ GE A ZNO NANOVLÁKNA: RŮST, CHARAKTERIZACE A ANALÝZA ÚROVNĚ DOPOVÁNÍ

DOCTORAL THESIS

DIZERTAČNÍ PRÁCE

AUTHOR
AUTOR PRÁCE

Ing. Tomáš Pejchal

SUPERVISOR
ŠKOLITEL

doc. Ing. Miroslav Kolíbal, Ph.D.

BRNO 2021

Abstract

Highly-doped semiconductor nanowires represent a promising class of nanostructures with prospective applications in electronics, optoelectronics or bio-sensing. This thesis is focused on the growth and in-depth characterization of germanium and zinc oxide nanowires, with the aim of acquiring high doping levels.

The first part of the thesis deals with the growth of germanium nanowires via the vapour–liquid–solid (VLS) process. Several factors impacting the nanowire growth and morphology are described – the composition of the catalytic particle, the role of surface adsorbates and the incorporation of atoms from the catalyst into the nanowire. The nanowires are grown from gold nanoparticles either in ultra-high vacuum (the MBE-like process) or in the presence of atomic-hydrogen vapour (mimicking the CVD process), resulting in dissimilar nanowire morphology and growth direction. The combined effect of atomic hydrogen adsorption and gold catalyst spreading is revealed – being the key element explaining the difference in nanowire morphology when MBE and CVD growth techniques are utilised.

Further, the Ge nanowire growth from group-III-containing catalysts is studied, with the intention of doping the nanowires via the incorporation of atoms from the catalyst droplet. The in-situ prepared alloyed Au–Ga catalyst is found to be applicable for germanium out-of-plane nanowire growth – although the catalyst stability is lower than for pure Au. Despite a high dopant concentration in the catalyst, no gallium incorporation into the nanowire is observed. Hence, this method of nanowire doping is proved unsuitable for the material system selected.

The third part of the thesis covers the characterization of ZnO nanowires and the development of a protocol for their diffusional doping with gallium. The impact of nanowire annealing on the concentration of oxygen vacancies (V_O) is demonstrated – annealing in H_2O_2 gas decreases the V_O concentration, compared with annealing in high vacuum. Further, Ga incorporation into ZnO nanowires is documented with in-situ SEM when annealed above 350 °C. Moreover, gallium-induced decomposition of ZnO nanowires is observed above 450 °C. The concentration and spatial distribution of Ga within the nanowires is assessed using STEM EDS and a theoretical model for Ga diffusion. The correlation between the V_O concentration and the Ga incorporation into ZnO is found. Gallium concentration in the order of 10^{21} cm^{-3} is reached in the nanowires – demonstrating the suitability of the presented diffusional-doping method for achieving high Ga doping levels needed for prospective bio-sensing applications in the IR region.

Key words

Nanowire, germanium, vapor–liquid–solid growth, faceting, hydrogen, zinc oxide, doping, diffusion.

Abstrakt

Vysoce dopovaná polovodičová nanovlákna představují nadějnou třídu nanostruktur pro budoucí aplikace v elektronice, optoelektronice nebo bio-senzorice. Tato práce se zaměřuje na přípravu a charakterizaci nanovláken germania a oxidu zinečnatého s cílem dosáhnout vysoké úrovně dopování.

Úvodní část dizertační práce se zabývá přípravou germaniových nanovláken metodou VLS (pára – kapalina – pevná látka). Nejprve jsou popsány faktory ovlivňující růst nanovláken a jejich morfologii – složení katalytické částice, vliv adsorbovaných atomů či molekul a potenciální inkorporace atomů katalyzátoru do objemu nanovláken. Nanovlákna připravená ze zlatých katalytických nanočástic v podmínkách ultravysokého vakua (tzv. MBE metodou) a za přítomnosti atomárního vodíku (proces napodobující podmínky CVD metod) vykazují odlišnou morfologii a směr růstu. Tyto rozdíly odhalují kombinovaný účinek adsorpce atomárního vodíku a šíření zlatého katalyzátoru na stěny nanovláken. Tento efekt je klíčový pro vysvětlení rozdílů ve výsledné morfologii nanovláken připravených MBE a CVD metodami.

Další část práce se věnuje přípravě Ge nanovláken z katalyzátorů obsahujících prvky III. skupiny a studiu jejich případné inkorporace, která by mohla vést k dopování nanovláken. Bylo zjištěno, že in-situ připravené směsné Au–Ga nanočástice lze úspěšně využít pro růst germaniových nanovláken, přestože stabilita katalyzátoru je nižší než v případě čistého zlata. I přes vysokou koncentraci gallia v katalytické částici nebyla pozorována inkorporace gallia do objemu nanovlákna. Tato metoda dopování nanovláken se tedy pro uvedenou materiálovou kombinaci ukázala jako nevhodná.

Ve třetí části práce jsou popsány výsledky charakterizace ZnO nanodrátů a vývoj metody jejich difuzního dopování galliem. Je prokázán vliv žíhání nanodrátů na koncentraci kyslíkových vakancí (V_O) – ve srovnání s žíháním v podmínkách vysokého vakua se koncentrace V_O snižuje žíháním v plynném peroxidu vodíku. Dále je zdokumentována inkorporace gallia do ZnO nanodrátů při teplotě nad 350 °C – pozorováno pomocí in-situ SEM. Při teplotě nad 450 °C dochází ke galliem indukované dekompozici ZnO nanodrátů. K určení koncentrace a prostorového rozložení Ga atomů v nanovláknech je využito teoretického difuzního modelu a STEM EDS měření nanovláken. Byla nalezena korelace mezi koncentrací kyslíkových vakancí a inkorporací gallia do objemu ZnO nanovláken. Koncentrace gallia dosahuje řádově 10^{21} cm^{-3}, což dokazuje vhodnost použité metody pro dosažení vysokých úrovní dopování, které jsou potřebné pro budoucí bio-senzorické aplikace v infračervené oblasti.

Klíčová slova

Nanovlákna, germanium, VLS růst, fazety nanokrystalů, vodík, oxid zinečnatý, dopování, difuze.

I declare that this thesis was composed by myself under the supervision of doc. Miroslav Kolíbal, Ph.D. The work contained herein is my own except where explicitly stated otherwise in the text. Parts of this work have been published in [77].

Ing. Tomáš Pejchal

Acknowledgement

Firstly, I would like to give thanks to Miroslav Kolíbal – not only for supervising this thesis but primarily for his friendship, openness, inspiration and leading by example. He has tutored me throughout my whole academic career. I have a great colleague, teacher and friend in him.

Secondly, I appreciate the reader for reading through this thesis. I sincerely hope you have found the few quips I inserted into the thesis in order to lighten the reading.

Also, I appreciate the staff from the Institute of Physical Engineering and CEITEC for all the support they tirelessly provide to the students – let me thank namely to Prof. Tomáš Šikola.

Next, I kindly acknowledge the collaboration with all the colleagues, whose measurements either appeared in this thesis or enabled it: I give thanks to Lukáš Kachtík and Kristýna Bukvišová for TEM and STEM EDS analysis, to Daniel Citterberg for the help with Raman, PL and transport measurements, to Stella Vallejos for preparation of ZnO nanowire samples, to Martin Kovařík for KPFM analysis of Ge nanowires and to Tomáš Musálek for being a fellow worker in MBE growth of nanowires.

Further, I give thanks to the group of Prof. Alois Lugstein (Institute of Solid State Electronics, TU Vienna) for sharing their know-how on electrical transport measurements of individual nanowires.

Last but not least, I deeply appreciate the long-lasting support of my family, friends and my wife.

Amen.

![Brno University of Technology logo]

![CEITEC Central European Institute of Technology, Brno, Czech Republic logo]

TOWARDS HIGHLY-DOPED Ge AND ZnO NANOWIRES: GROWTH, CHARACTERIZATION AND DOPING LEVEL ANALYSIS

VYSOCE DOPOVANÁ Ge A ZnO NANOVLÁKNA: RŮST, CHARAKTERIZACE A ANALÝZA ÚROVNĚ DOPOVÁNÍ

DOCTORAL THESIS
DIZERTAČNÍ PRÁCE

AUTHOR   Ing. TOMÁŠ PEJCHAL
AUTOR PRÁCE   ORCID iD: 0000-0002-5093-3023

SUPERVISOR   doc. MIROSLAV KOLÍBAL, Ph.D.
VEDOUCÍ PRÁCE   ORCID iD: 0000-0002-2751-5608

BRNO 2021

Table of Contents

1 Introduction

Semiconductor nanowires

Growth and characterization of semiconductor nanowires is an established field of scientific research. Nanowires represent a new class of highly attractive materials, which are intensively studied for their superior functional properties being quite different from their bulk counterparts [1]. Together with nanotubes, they exhibit a large surface-to-volume ratio, being beneficial for applications such as sensing or catalysis, where intense interaction with the environment is needed. Furthermore, thanks to their precise geometry, they represent technologically promising building blocks for future electronic and optoelectronic devices. The nanowire-based architecture allows building three-dimensional devices, significantly outperforming conventional planar technology.

In various state-of-the-art and prospective application areas, doped semiconductor nanowires represent a promising class of materials for improving the performance of present-day devices and also for designing novel architectures and devices-to-be. In modern electronics, semiconductor nanowires are already being used as conductive channels in the cutting-edge transistor fabrication, with a prospect of gate-all-around transistors. Another exciting concept is to utilize the nanowires as active sensing elements. For bio-sensing applications, doped semiconductors seem highly promising because their doping level and hence their electronic properties can be tuned and controlled, which is not possible with metals. Specifically, the plasmon resonance frequency can be tuned by the amount of activated dopants. Furthermore, multiple differently-doped segments can be built into a single nanowire, acting as separate sensing elements [2].

Doping of semiconductor nanowires

For cutting-edge and prospective applications, highly-doped semiconductor nanowires are required. The doping levels needed are predicted to be as high as 10^{20} cm^{-3} for most semiconductors (including silicon and germanium [3]). This is close to or even beyond the solubility limit of known dopants; it is difficult to achieve such levels with conventional semiconductors and doping techniques. Therefore, novel strategies and processes for effective doping are being searched for. A promising class of semiconductor materials are the transparent conductive oxides, which can be doped to high levels (up to 10^{21} cm^{-3}) by alloying with group-III metals [4]. A representative of such a material is e.g. zinc oxide (ZnO).

Currently, the doping of thin films and nanostructures is usually done by introducing a dopant-containing precursor gas into the chamber in CVD or by co-evaporation of dopant atoms in MBE during growth. According to the literature, the doping of nanowires is generally not homogeneous. There is a non-uniform doping profile – the dopant incorporation is enhanced close to the nanowire surface. This is caused by two independent effects [5]: (i) direct vapour–solid deposition of dopants onto the nanowire sidewalls [6] and (ii) preferential incorporation of dopants via VLS process close to the triple-phase boundary, where the liquid–solid interface is faceted and the supersaturation is the highest [7]. The former process can be affected by using a different gas precursor or by altering the diffusion length of dopant adatoms. For the latter one, the catalyst–nanowire interface is decisive, depending on the catalyst composition and growth kinetics. Besides the doping homogeneity, the crucial difficulty of nanowire doping is achieving high doping levels necessary for the aforementioned applications. The main obstacle is the solubility limit of dopants in conventional semiconductors (Si,

Ge, III-Vs). Furthermore, additional detrimental effects take place at high dopant concentrations; the doping efficiency decreases above a certain doping level.

For nanowires, the incorporation of dopants is no longer ruled by thermodynamics only (even if the growth and doping are performed close to thermodynamic equilibrium). Instead, it is governed mostly by kinetic effects of atom adsorption and diffusion on different facets, thus being dependent on nanowire morphology and surface termination [8]. For this reason, it proves difficult to reach the solubility limit itself, not to mention even higher dopant concentrations. On the other hand, nanowires can easily accommodate a significant amount of strain originating from impurities (including dopants) and differences in lattice constants. This lowers the number of defects, allowing the nanowires to be grown even defect-free, thus allowing higher dopant concentration to be reached.

Thesis objectives

The global objective of the thesis is the preparation and extensive characterization of germanium and zinc oxide nanowires – representing group-IV and II-VI classes of semiconductors – in both undoped and highly-doped state. The aim correlates with the global scientific efforts to produce and characterize highly-doped nanowires suitable for future applications, investigating novel approaches to nanowire doping. The thesis focuses on three main research areas:

(i)

Germanium nanowires grown from Au catalyst represent a simple material system, well covered in the literature. However, detailed growth mechanism is still not completely understood yet – regarding in particular the material transfer from the catalyst into/onto the nanowire and the impact of adsorbates passivating the sidewalls during growth onto nanowire growth and morphology. These phenomena are studied in the first part of the thesis; they are covered in section 2.2. Extensive characterization of the nanowire morphology is performed with transmission and scanning electron microscopy (SEM, TEM); surface chemistry of the nanowire is studied with spatially-resolved Auger electron spectroscopy (AES).

(ii)

Growth of germanium nanowires from dopant-containing catalysts and the possibility of incorporation of catalyst atoms into the nanowire are investigated in section 2.3. The process of catalyst incorporation – if proved – could be innovatively utilized for nanowire doping, provided that the catalyst contains proper doping elements. As the nanowire growth and material incorporation are non-equilibrium processes, the achievable doping level could even exceed the equilibrium dopant solubility in the nanowire [9; 10], thus outperforming current doping strategies. The growth from alloyed catalysts may well turn out to be an ideal technique for the preparation of highly-doped nanowires. The crystal structure and composition of such-prepared nanowires are examined by STEM EDS (energy-dispersive X-ray spectroscopy), investigating possible atom incorporation from the catalyst into the nanowire.

(iii)

Zinc oxide can be doped with aluminium or gallium to high concentration levels (up to 10^{21} cm^{-3}) [4], which could lead to plasmon-resonance-frequency shift of ZnO nanostructures up to the near-infrared region (NIR). This behaviour could be utilised e.g. for the direct detection of biomolecules. The thesis' third objective is to characterize the nominally undoped ZnO nanowires grown via the aerosol-assisted CVD method at atmospheric pressure (AACVD), and then to develop a doping

protocol and characterization procedures for ZnO nanowires diffusionally doped with gallium. The results are presented and discussed in chapter 3. Methods used for characterization (of individual nanowires as well as nanowire ensembles) are high-resolution SEM and TEM, real-time SEM imaging, Raman spectroscopy, X-ray photo electron spectroscopy (XPS), photoluminescence measurements (PL), AES and transport measurements of individual nanowires. Dopant incorporation into the nanowire is monitored directly by STEM EDS.

The reader may notice a dissimilar style of writing in chapters 2 and 3. The research subject of chapter 2 – Ge nanowires, their growth and characterization – has been well-established in the research group of the author's supervisor [11–13]. Therefore, the focus of this chapter (and section 2.2 in particular) is aimed at presenting the novel findings of the author in a concise form of factual and sober results. On the contrary, ZnO nanowires were a brand-new material system for our group. Their characterization was started by the thesis' author himself, building up the necessary know-how – and also instrumentation – to be utilized by other members of our research group as well. Accordingly, chapter 3 is written in a more story-telling style. Besides the results obtained, it also presents some obstacles encountered, dead ends and the experimental planning which had to be rethought repeatedly based on preceding results – as this is an integral part of scientific research as well.

Further, the conclusion of the doctoral thesis is presented in chapter 4. Last but not least, a gallery in the bonus chapter 5 shows a glimpse of the unusable results acquired along the way. They – despite being virtually unpublishable – possess a certain aesthetical value I humbly want to share with the respected reader, offering them pleasure and reward after reading through the scientific work. The author's publications and conference contributions are summarized at the end of the thesis.

2 Germanium nanowires

The growth of Ge nanowires from gold and other catalysts under various experimental conditions is discussed in this chapter. It is comprised of several parts: A literature review with present-day knowledge on the topic is given in section 2.1. The findings about the synergic effect of atomic hydrogen adsorption and Au catalyst spreading on the growth orientation of Ge nanowires are presented and discussed in section 2.2. Preparation of alloyed catalysts containing group-III elements for Ge nanowire growth (and potential doping) and the results of the growth itself are described in section 2.3.

2.1 Literature review

Vapour–liquid–solid growth

The most documented and widely-used technique for the growth of semiconductor nanowires is a vapour–liquid–solid growth (VLS), the name of which denotes the material pathway that gives rise to growth [14]. First, metal nanoparticles (gold in most cases) are deposited onto the substrate. After that the substrate is heated up above the eutectic temperature of the metal–semiconductor combination used (see the phase diagram in Fig. 1, position denoted A). Subsequently, a precursor gas containing the element of interest is let into the growth chamber (the case of chemical vapour deposition – CVD) or vapour atoms are deposited by evaporation from a solid source (molecular beam epitaxy – MBE). The metal droplet on the substrate now acts as a catalyst for thermal decomposition of precursor gas molecules or as a collector of diffusing adatoms, respectively [15]. The atoms are dissolved in the metal particle, which sooner or later reaches the near-eutectic composition [16] – see position B in Fig. 1. As the material supply continues, the system is driven out of equilibrium as the catalyst becomes rich with the semiconductor material (position C). The only possibility for the catalyst to reduce the semiconductor concentration (and hence to reach equilibrium again) is via nucleation of the solid semiconductor below the droplet. This is feasible once the critical concentration (also called supersaturation) is reached. The nucleation usually occurs at a triple-phase boundary (where solid, liquid and vapour phase meet) [15]; after a stable nucleus is formed it rapidly grows in two dimensions along the solid–liquid interface until the full monolayer is completed (so-called step-flow growth). This behaviour has been indeed observed using in-situ growth in TEM [17–20]. After the monolayer crystallization, the catalyst is depleted of the semiconductor material and for another monolayer to grow the critical supersaturation is to be reached again. Since the material is solidified below the droplet only, it grows in a form of a nanowire with the catalyst droplet at the tip, having roughly the same diameter as the droplet, as long as the catalyst stays stable on the nanowire tip (see the inset in Fig. 1).
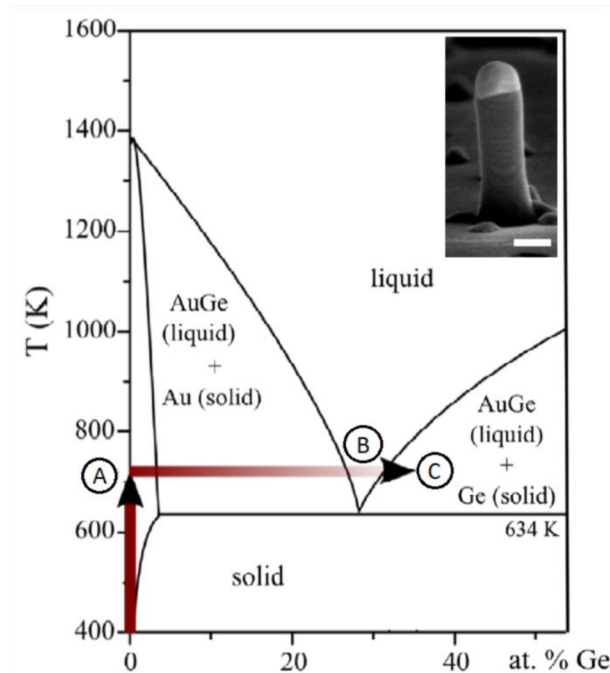
Fig. 1: Au–Ge phase diagram showing the temperature and composition of the catalyst particle at the very beginning of the growth process (indicated by the thick arrows). First, the metal particle is heated above the eutectic temperature (mark A). Then it gradually collects germanium atoms until it gets completely liquid (B) and eventually supersaturated with germanium (C), which is necessary for nanowire nucleation. In the inset: scanning electron microscopy image of a germanium nanowire (scale bar 100 nm) with a solidified Au catalyst droplet at the tip. Image courtesy of M. Kolíbal.

Importantly, the nanowires prepared by this method do not always grow perpendicularly to the substrate. Depending on the experimental conditions and materials used, the nanowire (still with the catalyst droplet on top) can grow along different crystallographic orientations. The growth direction of VLS-grown semiconductor nanowires and its control is a complex task attracting a lot of attention [21]. It has been demonstrated that group-IV nanowires preferentially grow in the <111> direction, irrespective of the substrate crystallographic orientation [22–24]. Schmidt et al. analysed the nanowire growth considering surface free energies of the growth interface and nanowire sidewalls [25]. They realized that the nanowire growth direction is not resulting from energy minimization of the whole nanowire–catalyst system, but originates from the energy balance between the catalyst–nanowire growth interface and a small nanowire segment below the catalyst where atom ordering during solidification takes place [26]. This concept based solely on thermodynamics introduced two possibilities to control the nanowire growth direction – either by catalyst engineering (thus potentially changing the solid–liquid interface energy) [27; 28] or by passivating nanowire sidewalls with different adsorbates (thus changing the solid–vapour interface energy) [29–31]. Another success of Schmidt's model is that it explained an intriguing experimental observation that small-diameter nanowires (usually less than 20 nm) prefer to grow in the <110> direction, while the larger-diameter ones grow in the <111> direction [32]. This behaviour has been observed in many material systems, including Si [25], III–Vs [33], II–VIs [34] and also Ge nanowires grown from molecular hydride precursors in CVD [35]. However, the model does not seem to reproduce well the experiments on Ge nanowires grown from atomic vapour in MBE, which tend to grow in the <110> growth direction for a wide range of diameters.

Gold vs. non-traditional catalysts for VLS growth

Choice of the catalyst droplet has a profound impact on nanowire growth, as it significantly changes the energy balance of the system (via the surface free energy of vapour–liquid and liquid–solid interfaces) as well as kinetics (via different equilibrium concentrations and semiconductor solubilities). Different experimental conditions to achieve nanowire growth when using different catalyst materials have been widely reported in the growth-related studies [36–39]. The catalyst droplet affects the optimum growth temperature, the nanowire–substrate epitaxial relation, the nanowire growth direction and morphology etc. Surprisingly, different crystal phases, including those unseen in bulk, have been reported when different materials have been used as catalysts [40]. This is namely the case of III-V semiconductors, which ordinarily adopt a zinc-blend (ZB) phase; yet also a wurtzite (WZ) phase has been reported in the nanowires [41]. Although the impact of the catalyst has been demonstrated in a variety of studies, the exact explanation is still being discussed. However, the catalyst droplet engineering represents a promising way to meet the requirements for future nanowire-based applications.

The most utilized catalyst for nanowire growth is indisputably gold. The growth of nanowires using Au catalyst was reported not only for group-IV and III-V semiconductors but also for ternary compounds [42] or even oxides, such as ZnO [43]. Along with its universality, the biggest advantages of gold are its chemical stability and reasonably low eutectic temperature of its compounds with the materials of interest (Ge, Si, III–Vs etc.). On the other hand, gold is inappropriate for use in current semiconductor electronics, as it could induce undesired electronic states in semiconductors [6; 44]. Another disadvantage is a relatively high semiconductor content in the catalyst droplet at the eutectic concentration (19 at.% of Si and 28 at.% of Ge as an example). This behaviour, often called the reservoir effect, limits gold for the growth of axial heterostructures, where a sharp interface (originating from negligible reservoir effect) is required. It seems that elements exhibiting low semiconductor solubility at eutectic concentration, such as Ga, In, Sn or Sb could represent an appropriate alternative to gold. Moreover, they are the proper doping elements for most of the semiconductors, which makes them even more intriguing for the catalyst-incorporation studies (see below).

Group-IV nanowire growth using Al catalyst has already been demonstrated [9; 45–50]. The growth from other group-III elements is rather difficult or unsuccessful due to the droplet instability (originating from their low surface free energy) [51] and low supersaturation in the droplet, which needs to be kept high by plasma-enhanced precursor decomposition to promote the growth [52–56]. The reports on the nanowire growth from group-V catalysts are scarce [10; 57–60], facing similar problems to group-III elements. Note again that the use of group-III and V elements as catalysts for nanowire growth has not been primarily driven by the intention of doping, but with the aim of utilizing the low solubility of semiconductor material in the droplet, which is promising for the growth of heterostructures with sharp interfaces.

A promising approach is to use alloyed catalysts, where one of the components is a low-reservoir-effect element (a prospective dopant) and the other is chosen to stabilize the droplet and increase (or otherwise manipulate) the solubility of the semiconductor material. Out of a variety of alloyed catalysts, only some material combinations have been reported to successfully initiate the growth of Si/Ge nanowires, e.g. Au–Ga [61–65], Au–Sn [66; 67], Au–Al [68] or In–Sn [10].

Incorporation of catalyst atoms into nanowires

The presence of a metal catalyst in the VLS growth process raises the question of catalyst-atom incorporation into the nanowire volume during growth. In case of gold – the most commonly used catalyst – such incorporation would represent a principal drawback for nanowire-based electronics due to a detrimental effect of Au-induced electronic states acting as a deep trap/acceptor or as a recombination centre [6]. However, the reports on the Au incorporation into the nanowire provide contradictory results [6; 69; 70]. Interestingly, massive catalyst-atom incorporation has been reported in Al–Si, In/Sn–Si, Sn–Ge and Ga–Ge material systems [9; 10; 67; 71–73]. Surprisingly enough, reported concentrations of catalyst atoms exceed the solubility limit by even two orders of magnitude. By contrast, no Sb atoms have been detected in the Sb-catalysed Ge nanowires examined within another study [57]. Based on existing reports, the incorporation of catalyst atoms into the nanowire seems to be material-dependent.

Nonetheless, the catalyst-incorporation effect, albeit applicable to specific material combinations only, may become a milestone in achieving extremely high doping levels of nanowires, provided the catalyst particle is made of – or contains – the dopant itself. In that case, the original drawback would turn into a new and promising field of study. It is important to note that the detailed mechanism of atom incorporation remains unclear. According to the currently accepted step-flow growth model [9; 10], the kinetics of catalyst atom incorporation into the growth front is dependent on critical supersaturation for nucleation and surface free energy of the droplet. Both quantities are primarily determined by the catalyst composition.

Role of surface adsorbates

The growth of nanowires is governed by the interplay between thermodynamics (in terms of free energy of the surfaces and interfaces present, droplet supersaturation and optimal growth temperature) and kinetics (the rate of atom adsorption and desorption, diffusion lengths, the incorporation of atoms into the droplet and the nanowire itself, the (non-)equilibrium concentrations and solubilities). Generally, for the growth of all kinds of nanowires, much effort has been made to find the optimal temperature and fluxes of precursor gases, to determine the proper supersaturation and to study the impact of the catalyst and the substrate–nanowire relation on the nanowire growth.

However, both the energy balance and kinetics of a growing nanowire can be strongly modified by the presence of different surface adsorbates and induced reconstructions, thus widening the process diversity and enabling the growth of new nanostructure morphologies. The role of these effects is surprisingly disregarded in current nanowire-growth studies. The reason is presumably the dominant role of CVD techniques, where the precursor gas carrying the growth element acts simultaneously as a source of hydrogen and hydrocarbons adsorbing on nanowire sidewalls, thus potentially changing nanowire morphology.

The real-time monitoring of the adsorbed species by FTIR (Fourier transform infrared spectroscopy) during CVD growth of Ge nanowires has been performed e.g. by Sivaram et al. [74]. They showed that the nanowire sidewalls are covered with adsorbed hydrogen during growth from hydride precursors. Gamalski et al. [75] demonstrated that the adsorbed by-products of digermane decomposition passivate the surface during growth and inhibit diffusion of Au on nanowire sidewalls

– thus significantly affecting Ge nanowire morphology. Such studies emphasize the importance of adsorbed species – hydrogen in particular – during the growth.

In contrast to CVD, where the effect of adsorbates is difficult to study, MBE growth allows separate control over the supply of the growth element and selected molecules for adsorption. The knowledge of how different adsorbates affect the nanowire growth and the surface free energies is a key to further increase the catalyst droplet stability at the tip of a nanowire by choosing appropriate surface chemistry (see Fig. 2).
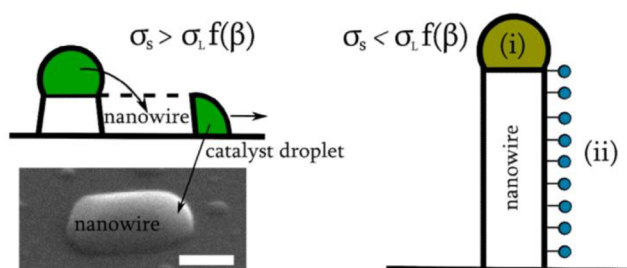

Fig. 2: According to the Nebolsin criterion [76], the stability of the droplet at the tip of a nanowire is dependent on the surface free energy of the solid (σ_S), liquid (σ_L) and the droplet contact angle β. Left: The nanowire growth with a pure liquid metal catalyst often fails, resulting in nanowires crawling across the surface (SEM image, Ge nanowire grown utilizing Ga catalyst, scale bar 200 nm). Right: Two plausible strategies to control the droplet stability: (i) manipulation of σ_L by engineering the catalyst composition, and (ii) manipulation of σ_S by controlled adsorption of appropriate molecules. Image courtesy of M. Kolíbal.

2.2 Revealing the synergic effect of atomic hydrogen adsorption and Au catalyst spreading on the growth orientation of Ge nanowires

As discussed in section 2.1, significant differences exist between Ge nanowires grown by vapour-phase techniques (CVD) and by atom evaporation from a solid source (MBE); the reasons have not been explained in a satisfactory and thorough way yet. Specifically, while the former exhibit <111> growth direction irrespectively of the substrate orientation and saw-tooth faceted morphology, the latter grow preferentially along <110> direction with smooth facets and different overall morphology. During CVD growth of Au-catalysed Ge nanowires, the nanowire sidewalls are covered with adsorbed hydrogen coming from the hydride precursors [74]; moreover, the adsorbed hydrogen (or other precursor gas fragments) significantly affect Ge nanowire morphology [75]. For MBE growth however (in experiments where atomic vapour is utilized for NW growth), the partial pressure of atomic hydrogen is quite low (<< 10^{-3} Pa) – this is most probably the key element making the difference between these two growth techniques.

Within this section 2.2, the evaporation from a solid Ge source with the optional assistance of atomic hydrogen has been used. The optimal conditions for the growth of Au-catalysed Ge nanowires prepared under vacuum conditions and with the assistance of atomic hydrogen have been found. What is important, the growth direction of Ge nanowires can be changed to <111> when prepared with atomic hydrogen assistance, thus mimicking nanowire growth from hydride precursors in terms of nanowire morphology and growth direction. Furthermore, in-situ spectroscopic evidence of dissimilar gold presence on the nanowire sidewalls has been observed and its role in determining the nanowire growth direction has been demonstrated and explained.

A detailed study presenting these findings, including also in-situ growth of the nanowires in SEM and a demonstration of intentional nanowire kinking, has been published based on results presented in

this thesis [77]. The study emphasizes and explains the key role of the synergic effect of atomic hydrogen adsorption and Au catalyst spreading on the growth orientation of Ge nanowires, especially during nanowire nucleation and initial stages of growth. In the following part of the thesis, a concise summary of the methods and the most important results are presented.

Methods, instrumentation

Ensembles of Ge nanowires were synthesized in an ultrahigh vacuum chamber (UHV, base pressure $< 3 \cdot 10^{-7}$ Pa) coupled to a Scanning Auger Microscope system (SAM, Omicron). In order to obtain a uniform and non-conglomerate distribution of catalyst particles, Ge(111) and Ge(110) substrates were cleaned by ultrasonic treatment in acetone and isopropanol and subsequently covered with gold nanoparticles (40 nm in diameter) by dipping the sample in a 450:1 mixture of a colloidal gold solution with HCl (5%). After reaching the growth temperature in the UHV chamber, the growth was carried out by deposition from an effusion cell (Ge flux oriented 30° to the sample surface) at a typical operation pressure of $5 \cdot 10^{-7}$ Pa in case of no hydrogen gas delivery (i.e. at ultrahigh vacuum). Note that the same set of experiments has also been performed under high vacuum conditions only (operation pressure $2 \cdot 10^{-4}$ Pa), giving identical results with respect to the studied subject. For the growth in the presence of atomic hydrogen, it was generated by cracking molecular hydrogen (introduced to the chamber by a leak valve, $p_{H2} = 2 \cdot 10^{-3}$ Pa) on a heated tungsten wire, placed in the vicinity of the sample (~ 2–3 cm).

Based on the knowledge of substrate orientation and crystal structure of the nanowire material, the information about the crystal orientation of the sidewalls and nanowire growth direction can be derived from SEM imaging. Its significant advantage is the possibility of changing the viewing angle in a wide range, thus allowing to focus on different features of the nanowire (e.g. top view, side view, alignment with different nanowire facets). Multiple examples on the use of SEM for determining the nanowire growth mode and morphology are presented hereafter.

Another technique used is Auger electron spectroscopy (AES), which can provide spatially resolved information on the chemical composition of a nanowire surface. Due to the very short mean free path of Auger electrons in the material [78], this method is extremely surface-sensitive, which makes it ideal for studying the processes on nanowire surface, such as catalyst spreading along the sidewalls. On the other hand, the extreme surface sensitivity is also the biggest disadvantage of this method due to contamination issues. In order to avoid contamination, the growth was performed in-situ in the vacuum chamber connected to the AES system; the samples were then transferred under UHV conditions for immediate measurement. The effect of contamination would become evident in the Auger spectra by (i) detecting C peak from hydrocarbons, (ii) diminishing of the peaks of desired elements and (iii) change of the overall spectrum shape.

To examine the crystal structure and chemical composition of the nanowires, a high-resolution TEM was used. The nanowires were scratched off the sample onto a standardized TEM grid (carbon foil on a copper support grid), localized using SEM and loaded into ThermoFisher Titan Themis 60-300 HR-TEM for imaging.
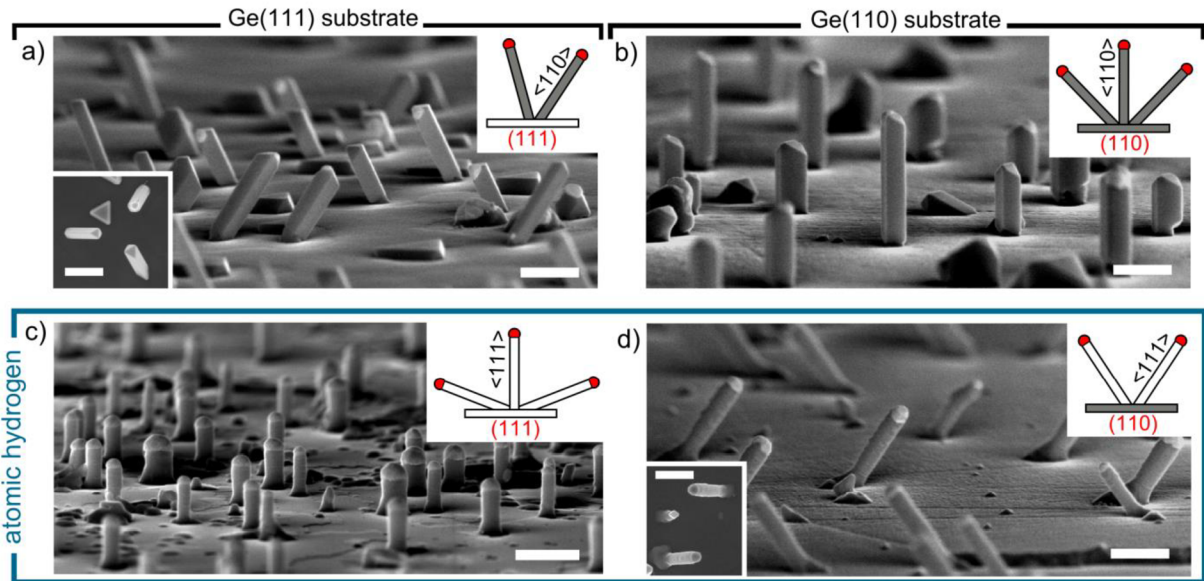
Fig. 3: SEM images of germanium nanowires grown in high vacuum (a,b) and with atomic hydrogen (c,d) on Ge(111) (a,c) and Ge(110) (b,d) substrates. The growth temperature was 425 °C in (a,b) and 385 °C in (c,d). Viewing directions are close to (a) [-110], (b) [-112], (c) [1-10] and (d) [-110] (the samples are tilted by 85° to the surface normal and by 5° to the designated viewing direction). The insets in (a) and (d) are top-view SEM images of the sample; the schematics illustrate the possible degenerate nanowire growth orientations (grey - <110>, white - <111>). Scale bars 400 nm. Published [77].
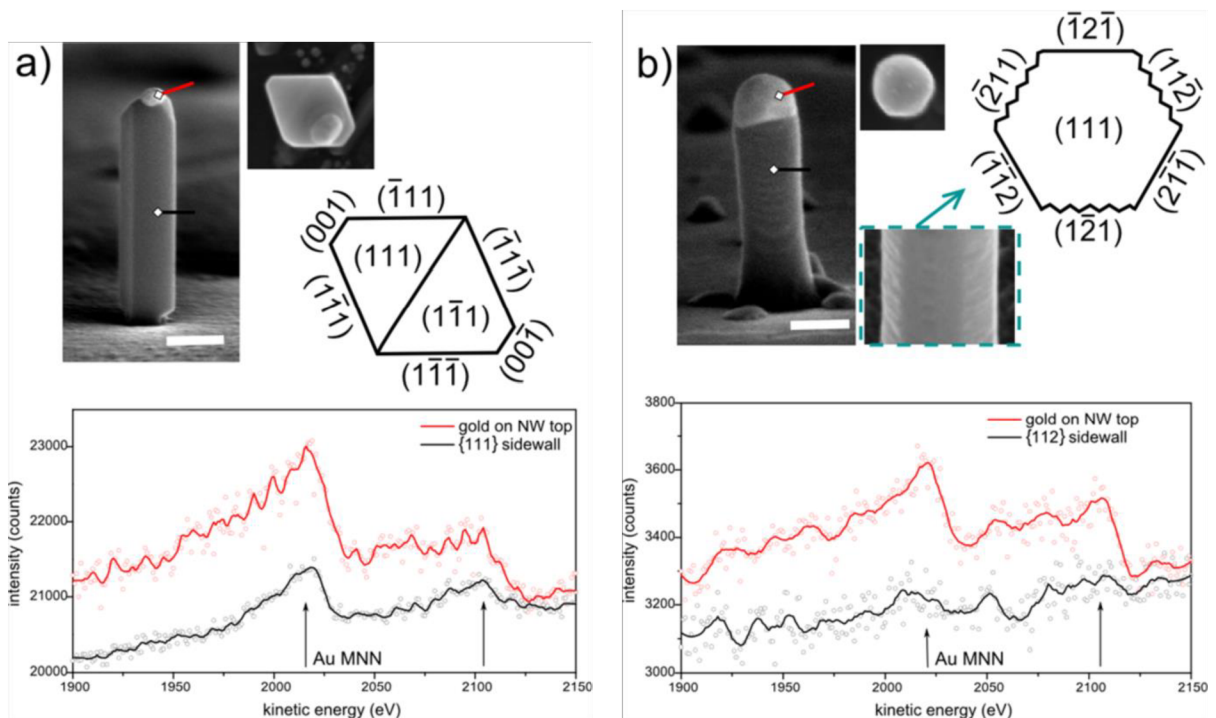

Fig. 4: Morphology of nanowires grown (a) in high vacuum on the (110) substrate and (b) with atomic hydrogen on the (111) substrate as observed ex-situ by SEM. Sketched top views show crystallographic orientations of the sidewalls and top facets; in (b) the sidewalls with pronounced sub-faceting are highlighted by zig-zag lines. A detailed view of <111> nanowire sidewalls is shown in (b), with the viewing direction marked by the green arrow. The coloured marks indicate locations where the Auger spectra were taken. The positions of the main Au MNN peaks (2015 eV and 2101 eV) are designated by the arrows. (a) Scale bar 200 nm. (b) Scale bar 100 nm. Published [77].

Growth in (ultra-)high vacuum

The substrate temperature window for Ge nanowire growth by evaporation under high (or ultrahigh) vacuum conditions was found to be quite narrow (385 °C – 455 °C), limited from the lower end by surface diffusion of germanium atoms across the substrate and NW sidewalls, and from the upper end by their desorption [40; 41]. All the nanowires within this temperature range grow in the <110> direction, irrespective of the substrate crystallographic orientation and nanowire diameter (40 nm – 200 nm), as shown in Fig. 3a,b. The assignment of the growth direction was made by assuming the diamond cubic lattice structure and determining an angle between the growth axis and the substrate; additionally, it was verified by a detailed TEM analysis (see Fig. 6). It is interesting to note that the <110> oriented nanowires on the (110) substrate grow only perpendicular to the substrate and not in the other four possible (crystallographically equivalent) inclined <110> directions (Fig. 3b). This is different from the (111) substrate, where all three equivalent <110> growth directions are observed (see the inset in Fig. 3a). The nanowires grown under (ultra-)high vacuum have mostly a truncated rhombohedral cross section, with four major {111} and two truncating {001} sidewalls – see Fig. 4a. The latter are often overgrown and the cross section changes to rhombohedral. The growth interface is formed by two inclined (mutually tilted) {111} facets.

Growth in the presence of atomic hydrogen

The presence of atomic hydrogen in the chamber during growth changes the growth direction of nanowires to <111> (Fig. 3c,d) as well as nanowire morphology (Fig. 4b). However, this change does not apply to the whole temperature growth window. The nanowires shown in Fig. 3c,d and Fig. 4b were grown at 385 °C. At higher temperatures, increased roughening of the sidewall facets is observed; finally, at temperatures above 435 °C the <110>-oriented nanowires with clearly-defined {111} sidewalls grow despite the presence of atomic hydrogen in the chamber – see Fig. 5. This effect can be ascribed to rapid desorption of atomic hydrogen from NW sidewalls with increasing temperature, thus mimicking the high-vacuum growth. The morphology of the nanowires grown in high vacuum remains the same for a wide range of Ge deposition rate (0.075 Å·s^{-1} to 0.225 Å·s^{-1}). However, the nanowires grown at low temperature (385 °C) in the presence of atomic hydrogen adopt the morphology shown in Fig. 4b only for the lowest deposition rate (~ 0.075 Å·s^{-1}). With increasing flux of Ge atoms (deposition rate up to 0.225 Å·s^{-1}), pronounced faceting is observed (similarly to the effect of raising temperature), while the growth direction remains <111>.

For the nanowires grown in the presence of atomic hydrogen, not all the degenerate <111> growth directions on the (111) substrate are equal, as the one perpendicular to the substrate is observed solely (Fig. 3c). In contrast to NWs grown under high vacuum conditions, all the NWs still have catalytic gold droplets on their top (visible in Fig. 3 due to different contrast). The <111> NWs grown at low temperatures with atomic hydrogen have a planar (111) growth interface (possible truncation as reported previously [38] is not visible due to droplet presence) and hexagonal cross-section (Fig. 4b). The {211}-oriented sidewalls exhibit different roughness on opposite facets (strongly resembling the sawtooth faceting of Si NWs grown by CVD) [81]. The sawtooth faceting of Ge nanowires has not been discussed in literature properly yet, although it has been already observed, especially above 300 °C [74; 75; 82; 83]. In case of gold-catalyzed Si nanowires, the partially Au-decorated sawtooth facets stabilize the growth in the <111> direction [84]. In order to confirm or exclude the presence of Au on Ge nanowire sidewalls, the nanowires were analysed by spatially-resolved Auger electron spectroscopy. The spectra taken on the nanowire sidewalls clearly indicate the presence of

a significant amount of Au on nanowires grown under the high vacuum conditions (Fig. 4a) and, in contrast, the absence of Au on sidewalls of <111>-oriented nanowires grown at low temperature with atomic hydrogen (Fig. 4b). Slight differences between the two types of {211} sidewalls of the <111> nanowires have been detected, being indicative of a trace amount of gold present on certain facets, but the signal was too weak to be conclusive.
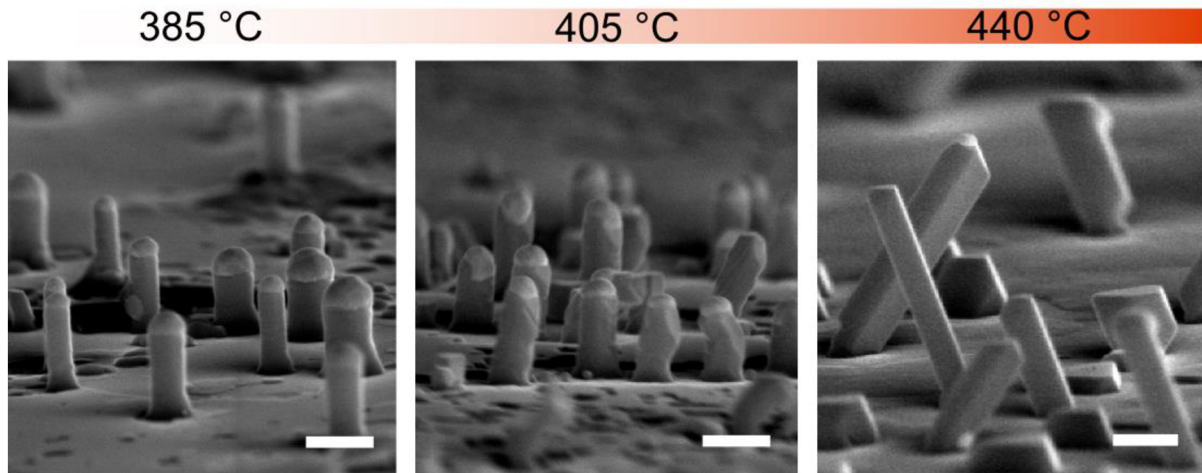

Fig. 5: Morphology and growth direction change of Ge NWs grown with atomic hydrogen at higher temperatures. The samples were grown under the same growth conditions (p_{H2} = 2·10^{-3} Pa) except the temperature, which is indicated in the figure. The nanowires grown at the lowest temperature of the available growth window exhibit relatively smooth {211} sidewalls with sub-faceting as indicated in Fig. 4b. With increasing growth temperature the faceting of nanowire sidewalls gets more significant, as {111}-oriented larger facets are often observed. Also, catalyst droplet losses become more frequent. At temperatures higher than 435 °C the nanowires change the growth direction to <110> despite the presence of atomic hydrogen in the chamber environment. Scale bars 200 nm. Published [77].

Growth in the presence of other molecular species

Experiments with other gases (molecular hydrogen, O_2, Ar and CH_4) introduced into the chamber during growth have been performed as well. However, no effect of changing the nanowire growth direction or morphology with respect to the growth under vacuum conditions has been observed. Hence this effect seems to be related specifically to atomic hydrogen.

TEM characterization of <110> and <111> Ge nanowires

According to the results presented above, the sidewalls of nanowires grown in high vacuum are covered with a thin layer of gold. Indeed, Au clusters were observed using TEM imaging (areas of different contrast and crystal structure on the nanowire surface, not shown here). What's more, a single-crystalline nature of Ge nanowires was confirmed for both <110> and <111> nanowires (grown in high vacuum and with atomic hydrogen, respectively) – see the TEM analysis in Fig. 6. The growth direction of the nanowires and the sidewall crystallographic orientation – previously inferred from SEM analysis – were confirmed by the TEM characterization as well.
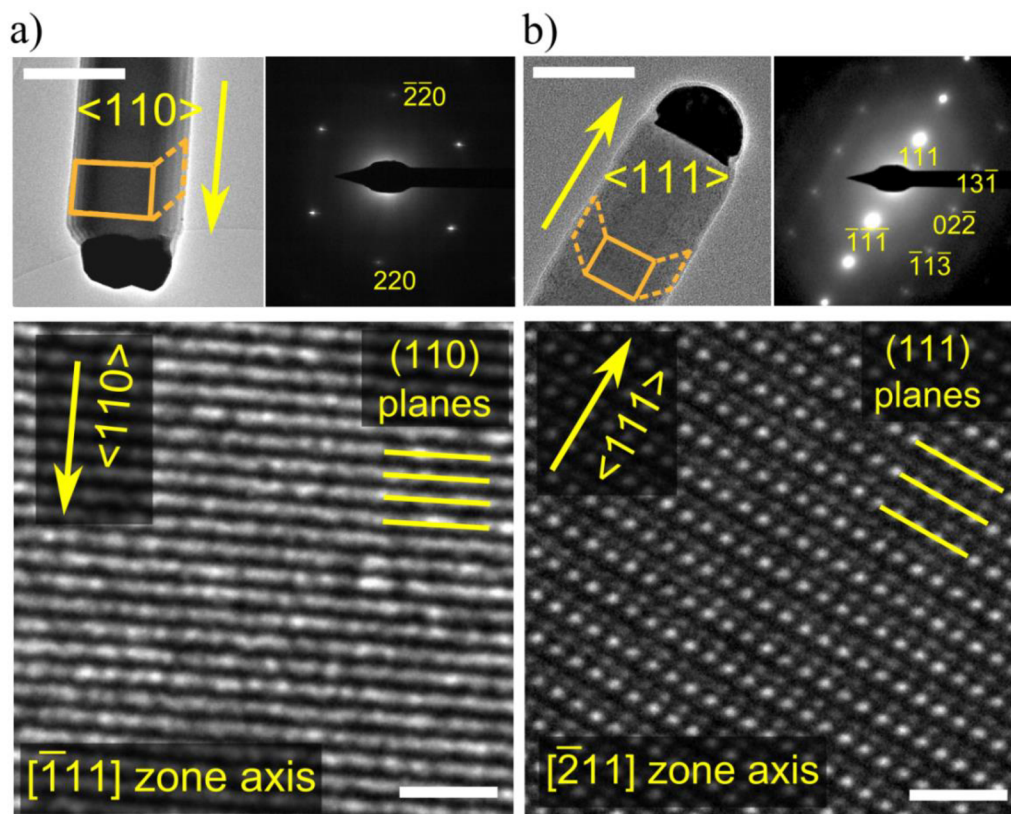
Fig. 6: TEM analysis of (a) <110> and (b) <111> nanowires grown in high vacuum and with atomic hydrogen, respectively. The lattice-plane resolved images (scale bars 1 nm) allow verifying the growth directions of both types of nanowires as determined by SEM. Additionally, selective area diffraction patterns (SAED) taken with the electron beam perpendicular to the nanowire sidewall confirm the sidewall crystallographic orientation, being {111} for <110>-oriented nanowires and {112} for <111>-oriented ones (the sidewall configuration is marked schematically in orange; the sidewall perpendicular to the electron beam is outlined with the solid line). The scale bars in overview images (always top left) are 200 nm and 100 nm in (a) and (b), respectively. TEM imaging: L. Kachtík. Published in supporting information of [77].

Discussion & Summary

The results presented so far implicate that (i) atomic hydrogen prevents gold from diffusing out of the catalyst along the sidewalls and (ii) gold promotes the formation of {111}-oriented sidewall facets. The presence of hydrogen adsorbed on germanium nanowire sidewalls up to 330 °C in case of nanowires grown from hydride precursors has been already confirmed by Sivaram et al. [74] Here, atomic hydrogen is generated more efficiently by thermal cracking of molecular hydrogen on a heated filament at high partial pressures (p_{H2} = $2 \cdot 10^{-3}$ Pa), which results in a very high adsorption rate r_{ads} (dependent on the incoming flux). The nanowire sidewalls are thus flooded with atomic hydrogen which allows to efficiently replenish adsorbed hydrogen despite the high desorption rates at enhanced temperatures used in the growth experiments. The surface diffusion of gold atoms is critically dependent on the adsorbates [85]; it has been shown by Gamalski et al. [75] that by-products of digermane decomposition passivate the surface during growth and inhibit diffusion of Au on nanowire sidewalls.

The effect of gold on germanium faceting is demonstrated in Fig. 7. As the surface energies of bare Ge facets of different crystallographic orientations are similar, the equilibrium crystal shapes are complex, exposing many different facets [86]. A stress-free homoepitaxy of Ge on Ge(111) and Ge(110) surfaces results in germanium island shapes strongly resembling those obtained using the

14

Wulff construction (Fig. 7a,c). Experimental studies of flat Ge surfaces suggest that low-index planes are stabilized after exposure to atomic hydrogen due to (1×1)-H reconstruction [87–89]. Thus for nanowire growth at low temperatures, the sidewalls are Au-free; probably passivated with atomic hydrogen [74]. Nanowires then exhibit nearly cylindrical [22] or hexagonal cross sections as the growth is not constrained by any preferential sidewall orientation. The presence of Au on the sidewalls under conditions promoting Au diffusion (e.g. high vacuum or high temperature) dramatically changes the surface free energies in favour of {111} facets (Fig. 7b,d).
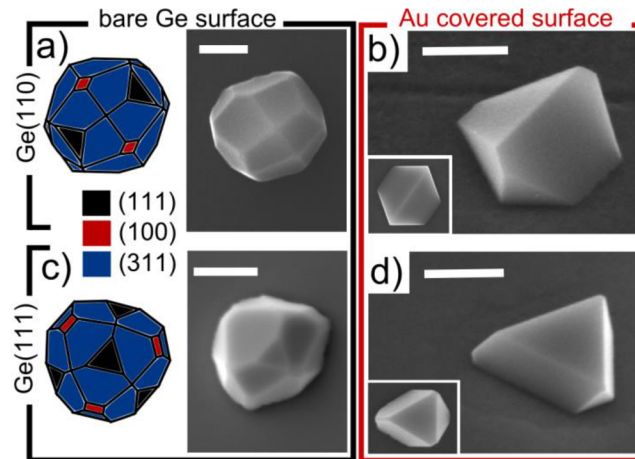

Fig. 7: Homoepitaxial growth of Ge on bare (600 °C) and gold-covered (400 °C) Ge(110) (a,b) and Ge(111) (c,d) surfaces in high vacuum. In (a) and (c) equilibrium crystal shapes are depicted (after Stekolnikov et al. [86]). The SEM images in (b,d) are tilted by 52°; (a,c) and insets in (b,d) are top views. All the scale bars are 200 nm, except in (c) (500 nm). Published [77].

To conclude, the results presented and discussed in this section show that the synergic effect of adsorbed atomic hydrogen and Au catalyst spreading is critical for determining the nanowire sidewall orientation and, consequently, the growth direction and morphology of Ge nanowires. For more details, see the published results [77].

2.3   Dopant-containing catalysts for Ge nanowire growth

Growth of germanium nanowires from Au catalyst droplet by means of evaporation is well documented in the literature (see the review in section 2.1) and has also been successfully performed by our research group [11–13; 90]. Besides, some of its aspects were investigated and presented within the previous section 2.2. The novel finding is that the combined effect of atomic hydrogen adsorption and gold out-diffusion from the catalyst particle radically changes the nanowire morphology and growth direction. The surface chemistry of the substrate and the nanowires is but one example of the wide range of parameters controlling nanowire growth in general. Another key aspect is the chemical composition of the catalyst particle itself – as it governs a plethora of physical quantities important in the nanowire growth (such as the chemical potentials, wetting angle on the nanowire material, semiconductor solubility in the catalyst, eutectic composition and temperature, diffusion and overall kinetics of the process and many others).

In contrast to gold, Ge nanowire growth from pure group-III catalysts has been reported to be difficult due to their low surface tension and the co-called Nebol'sin criterion [76]:

For the VLS growth of semiconductor nanowires to be stable, only a limited range of liquid droplet's contact angles φ is thermodynamically plausible, depending on the ratio $\frac{\gamma_{SV}}{\gamma_{LV}}$, where γ_{SV} is the surface

15

energy of the solid–vapour interface and γ_{LV} is the surface energy of the liquid droplet (see the schematics in Fig. 8a,b). For nanowire growth, the stability region is defined as follows [76]:

$$\frac{\gamma_{SV}}{\gamma_{LV}} < \frac{\sin\varphi + \cos\varphi}{\cos\delta - \sin\delta} \qquad (2.1)$$

The angle δ is depicted in Fig. 8b – it is the angle between the conical nanowire surface and the growth axis; for constant-radius nanowires $\delta = 0$. For illustration, the inequality (2.1) is plotted in Fig. 8c for silicon nanowires growing from Au–Si liquid droplet (non-tapered nanowire, see curve 1) [76]. In regions I and III, the inequality is not met and whisker growth is unlikely. Instead, the reverse process takes place – silicon etching and vaporization (region I and III, respectively). Region II delimits the stable growth conditions. In contrast to gold, for the low-surface-tension materials (such as Ga, Al, In, Sn) it is much more difficult to satisfy the inequality (2.1) due to their lower γ_{LV}. Then, the range of energetically favourable contact angles is narrow or diminishes completely. For conical nanowires though, the range of contact angles suitable for growth is broader, see curve 2 in Fig. 8c. It is for this reason that short conical crystals are often observed, not followed, however, by a stable nanowire growth stage [76]. In short, stable nanowire growth occurs for the catalyst droplets of high values of surface energy γ_{LV}.
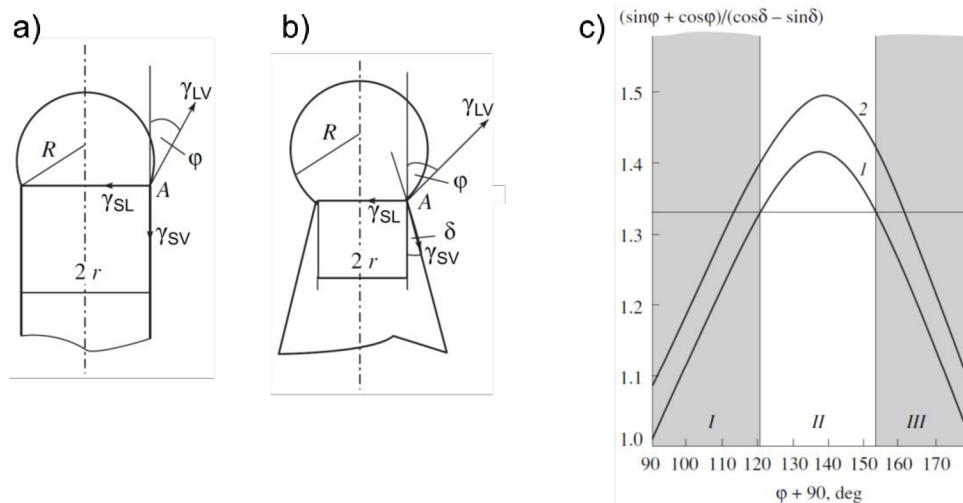

Fig. 8: Geometry of the nanowire growth: a) constant-radius nanowire ($\delta = 0$); b) tapered nanowire ($\delta > 0$). c) Plots of $\frac{\sin\varphi + \cos\varphi}{\cos\delta - \sin\delta}$ against the contact angle of the melt droplet atop the nanowire: (1) constant radius ($\delta = 0$), (2) tapered nanowire ($\delta > 0$). Shaded areas I, III are regions of whisker etching and vaporization, respectively, by the SLV mechanism; region II allows steady-state nanowire growth by the VLS mechanism. Adopted from [76].

A possible way to overcome this limitation is to modify the surface energy of the solid nanowire (as schematically depicted already in Fig. 2). Interestingly, Yu et al. [51] presented successful growth of Sn-catalysed Si nanowires, despite the low surface tension of tin. Their analysis revealed the existence of an ultrathin sidewall-spreading catalyst layer that helps to stabilize the catalyst droplet atop the nanowire during growth by modifying the effective γ_{SV} value.

Also, Si nanowire growth from Al or In–Sn catalysts and Ge nanowire growth from Sn or Ga catalysts were successfully demonstrated and what's more, massive incorporation of catalyst's atoms into the nanowires was recorded [9; 10; 71; 72]. The question of catalyst-atom incorporation into the nanowires during growth has been already raised in the review section 2.1. Prospective benefits are

clear – the process of catalyst incorporation could be utilized for nanowire doping, even beyond the equilibrium solubility limits.

Further, other studies showed that sharp axial hetero-junctions are obtained when nanowires are grown from alloyed catalysts containing group-III element. Sharp Si–Ge interfaces were reported when grown from Au–Ga catalyst [63] or Au–Al catalyst [68] due to lower reservoir effect.

Therefore, the possibility of Ge nanowire growth from group-III-containing catalysts is studied in this section; with a special focus on potential dopant incorporation. As a first step, the results of the preparation of novel catalysts for nanowire growth are summarized. Then, the results of the nanowire growth are presented – concentrating on the morphology of the resulting structures and the analysis of possible dopant incorporation. First, alloyed Au–Ga mixture is studied as a catalyst for Ge nanowire growth. Further, pure gallium, pure aluminium and gold–indium mixture are investigated.

Alloyed Au–Ga catalyst

Gallium has very low surface tension compared to gold [28; 37; 53; 54]. Therefore, pure Ga catalyst droplet is unstable on nanowire top and only in-plane growth of Ge structures is observed, see our results below (Fig. 15). By alloying gallium with other metals – such as gold, for which the stable out-of-plane NW growth has been shown above – it should be possible to stabilize the droplet and thus facilitate the out-of-plane growth. The drawback of using alloyed catalyst is in general much higher complexity in terms of material chemistry. Instead of using a simple phase diagram (mixture of supply material and the catalyst, Au–Ge for example), a tertiary phase diagram shall be considered (Au–Ga–Ge in this case). Such diagrams are more difficult to calculate or determine experimentally and they are rarely published.

Still, stable nanowire growth from alloyed Au–Ga catalyst shall be of high interest, considering possible Ga incorporation during growth, leading to nanowire doping. Two approaches will be described below: (i) Preparation of alloyed Au–Ga catalyst on a plain Ge substrate, followed by Ge deposition; (ii) formation of Ge nanowire stem grown with pure Au catalyst, followed by deposition of a small amount of gallium during the growth process, thus forming mixed Au–Ga catalyst on top of an existing nanowire. The Ge deposition and nanowire growth then continue (given that the catalyst remains stable).

The SEM micrographs of Au–Ga catalyst of various relative compositions prepared on a plain Ge wafer are shown in Fig. 9, taken ex-situ at room temperature. Gold nanoparticles from colloidal solution (40 nm diameter) were drop-casted onto Ge (111)-oriented wafer. It was then loaded into a UHV chamber, where Ga was evaporated onto the heated sample. Its deposition rate was 0.17 monolayers per minute (ML/min); sample temperature was 475 °C, being above the eutectic temperature of Au–Ga, which is 449 °C. Au–Ga alloyed droplets were formed on the surface; no pure-Ga droplets are observed under these conditions. As seen in Fig. 9, Au/Ga ratio is controlled by Ga deposition time. After cooling down for ex-situ imaging at room temperature, the alloyed mixture has separated again into Au core and Ga shell, clearly seen in the SE contrast. Different size of Au core is due to clustering of original Au nanoparticles.
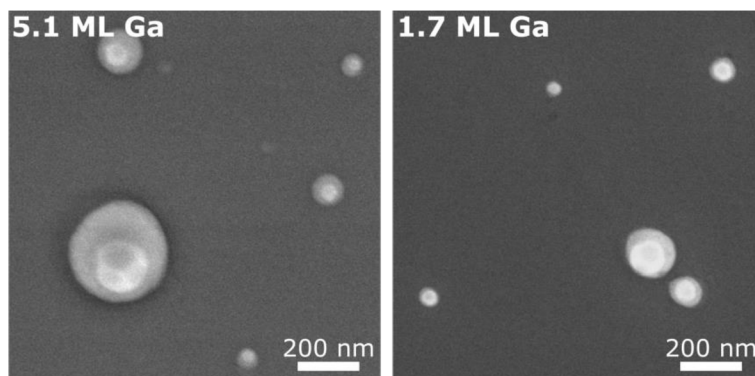
Fig. 9: SEM images of alloyed Au–Ga catalyst upon cooling down to room temperature. The images were taken ex-situ using the SE contrast. The size and composition of the catalyst particles are controlled by the amount of deposited gallium (inscribed in the images).

Keep in mind that the Au–Ga particles gradually incorporate germanium from the substrate as well, which might change the physical properties of the alloyed catalyst. (For more insight into this catalyst–substrate interaction and material uptake, being important especially during the initial stage of nanowire growth, read another paper of our research group [90].) In order to prove that the Au–Ga particles truly do alloy, a real-time in-situ SEM study was performed for such Au–Ga catalysts, see Fig. 10. Each row of images shows a different area on the sample. The sample temperature is indicated for each column. The SE contrast shows the bright Au core ringed with gallium. Indeed, the temperature series show the gradual alloying of catalyst particles.
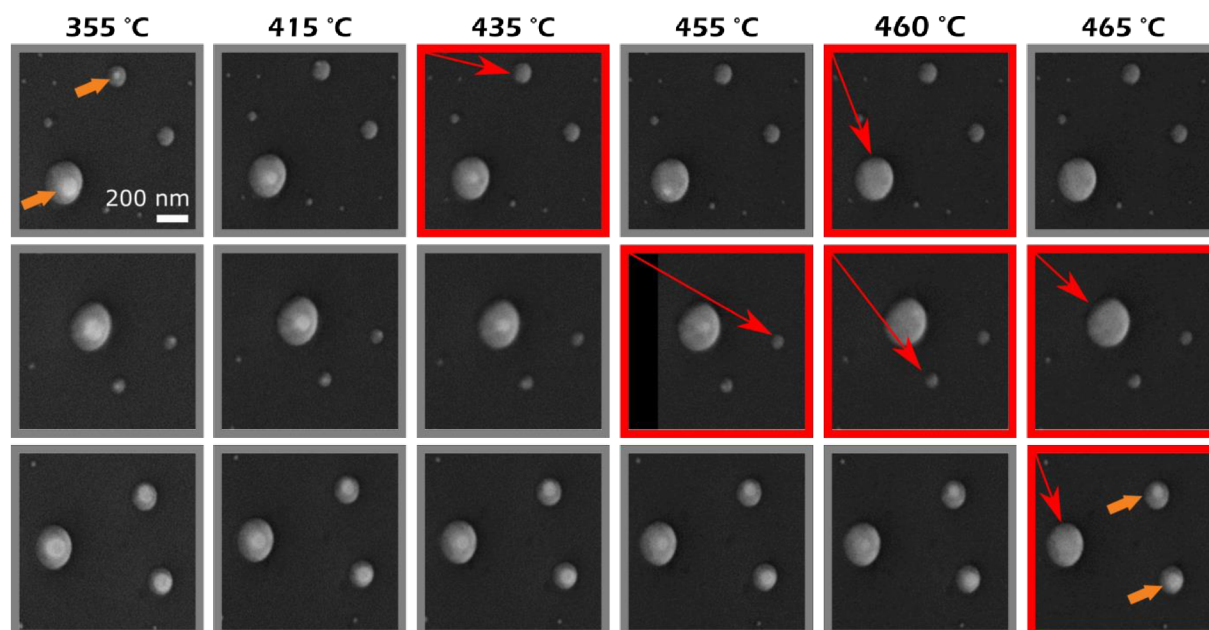

Fig. 10: Real-time in-situ SEM observation of Au–Ga alloying of catalyst particles. The annealing temperature is indicated for each column. Each row represents a different area on the sample. Red arrows indicate when the droplets become fully alloyed. Some of the droplets remain non-alloyed. The eutectic temperature of Au–Ga system is 449 °C [93].

Having demonstrated the preparation of suitable Au–Ga alloyed catalyst particles, the next step is Ge deposition onto the sample. In order to reveal the effect of catalyst composition (i.e. Ga amount in the alloyed catalyst) on nanowire growth, different amount of gallium was deposited onto the samples with Au particles prior to Ge evaporation – see the resulting morphologies in the SEM micrographs in Fig. 11. The optimal sample temperature for Ge nanowire growth from pure Au catalyst is 415 °C (Fig. 11a); it was applied to all samples shown. The amount of deposited Ge is the

same as well. The only variable parameter was the amount of Ga deposited – see the value inscribed in Fig. 11b-d. The increasing amount of gallium – albeit of sub-monolayer coverage – leads to catalyst instability and formation of truncated faceted Ge pyramids instead of out-of-plane nanowires. Note that for 0.085 ML and 0.17 ML coverage (Fig. 11b,c), some nanowires are still formed, but they are shorter and much less frequent than for pure Au catalyst (see the insets).
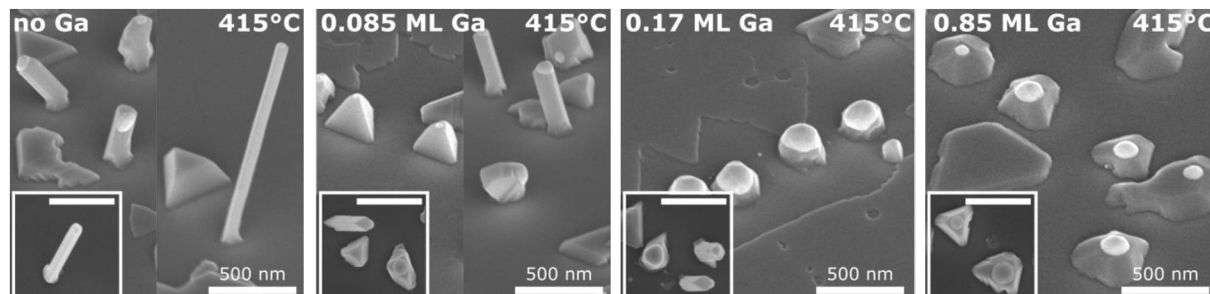

Fig. 11: Growth of Ge structures from alloyed Au–Ga catalyst of various composition. Au–Ga catalyst particles were prepared prior to Ge deposition; their composition is governed by the amount of gallium deposited (inscribed in the images). The sample temperature during Ge evaporation was 415 °C. The images were taken for sample tilted by 45°; the insets (scale bars 500 nm) show the top view.

The occurrence of Ge nanowires even for non-zero Ga coverage is a sign of possible stable growth from Au–Ga catalyst. Therefore, the effect of sample temperature during nanowire growth was studied, see Fig. 12. First, the alloyed catalyst was formed at 475 °C by deposition of 0.17 ML of gallium. After cooling down to growth temperature and its stabilization, Ge deposition was performed. Whereas the growth at 415 °C yields truncated Ge pyramids (Fig. 12a), decreasing the growth temperature to 409 °C or even 383 °C results in stable Ge nanowire growth (Fig. 12b,c). Note that the temperature of 383 °C is much lower than the optimum for the growth from pure Au catalyst (being 415 °C). In other words, even sub-monolayer Ga coverage decreases the temperature needed for Ge nanowire growth.
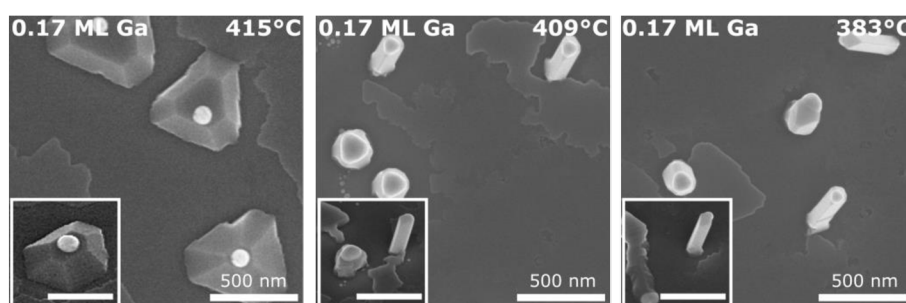

Fig. 12: Morphology of Ge structures grown from alloyed Au–Ga catalysts at various sample temperatures. Au–Ga catalyst particles were prepared prior to Ge deposition in an identical way; only the sample temperature during Ge deposition varied. The images show the top view; the insets (scale bars 500 nm) are tilted by 45°.

The catalyst stability might differ at the beginning of nanowire growth (i.e. during the formation of nanowire base) and during nanowire growth (when the droplet is pinned onto the growth facets). The latter situation will be studied hereafter. First, a Ge nanowire stem was grown from a pure Au catalyst. Then, a small amount of gallium was co-deposited in-situ during nanowire growth, i.e. without stopping Ge evaporation. Then, only the Ge deposition continued. Therefore, the catalyst composition and surface chemistry are changed in the middle of the nanowire growth, which may or may not continue. In Fig. 13, see the results for various amount of Ga deposited in the middle of Ge deposition. The growth temperature was 415 °C for all samples. For the highest Ga coverage

(0.085 ML), the catalyst becomes unstable, which results in losing the catalyst from the NW top and subsequent 3D over-growth of the nanowire with Ge material, see Fig. 13c. Interestingly, for 0.014 ML Ga coverage, some nanowires lose the catalyst as a result of its instability, whereas other nanowires change their diameter and continue growing in the original direction, see Fig. 13b. Interestingly, no kinks were observed. The diameter change observed for multiple nanowires indicates the moment when Ga was added into the catalyst. What is important, stable nanowire growth continued.
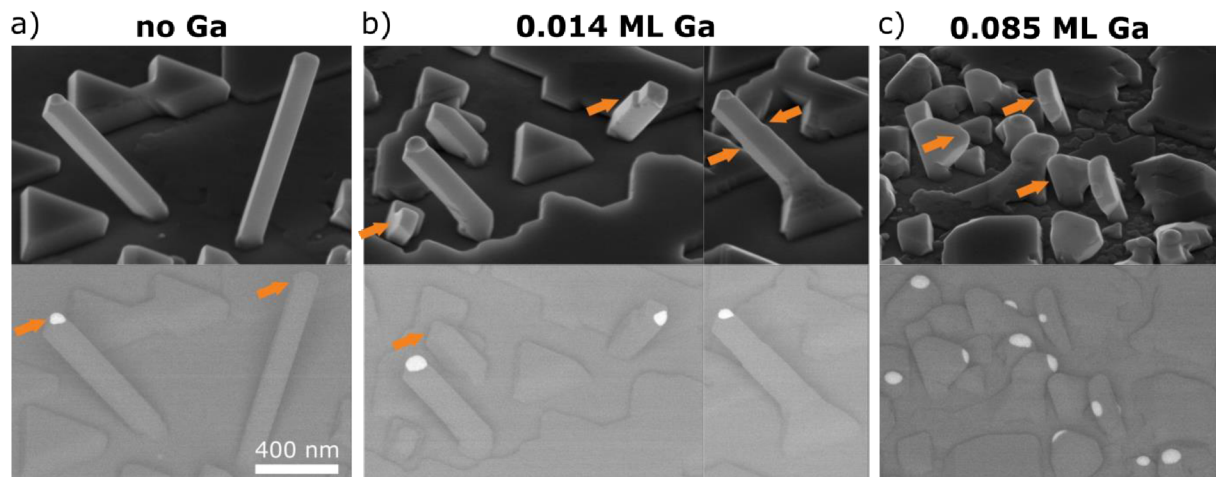

Fig. 13: Growth of Ge nanowires from Au–Ga catalyst formed during the growth. SEM images with SE contrast (top row) and BSE contrast (bottom row). The alloyed catalyst was formed by depositing gallium onto the sample with pure Au catalysts on top of previously grown Ge nanowires. The series shows the effect of deposition of different amount of gallium. The areas of interest are highlighted by orange arrows.

Further, the presence of gallium in the catalyst was confirmed by two independent methods – Auger electron spectroscopy (not shown here) and STEM EDS analysis, see Fig. 14. For this analysis, a nanowire with a slight diameter change from Fig. 13b was selected. The TEM BF and HAADF contrast images are shown in Fig. 14a,b respectively. Clearly, no crystal defects are present, despite the diameter change. Further, the EDS analysis was performed with the following results (see Fig. 14c): (i) It confirms high content of Ga in the catalyst particle (up to 4 at.%), although only 0.014 ML of Ga was deposited; (ii) the composition remains the same throughout the nanowire body, i.e. no compositional change is observed after Au–Ga catalyst formation; (iii) gallium incorporation from the catalyst into the nanowire was not proved. (The value of 0.2 at.% is below the detection limit.)
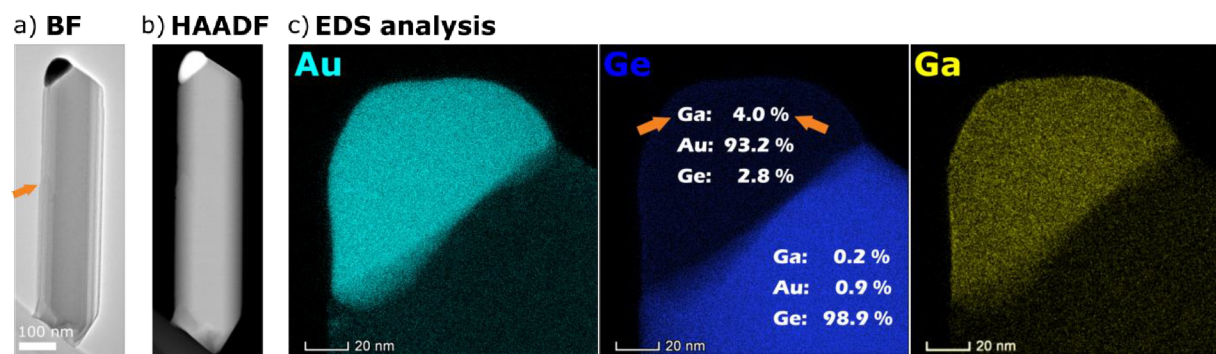
Fig. 14: a,b) TEM images (BF and HAADF contrast, respectively) of a Ge nanowire, for which an alloyed Au–Ga catalyst was formed in the middle of the growth (note the corresponding slight change in diameter, indicated by the orange arrow). A wire from the sample shown in Fig. 13b was used. c) STEM EDS analysis of this wire. The measured composition of catalyst droplet and nanowire body is inscribed. TEM imaging and EDS analysis: K. Bukvišová.

Pure Ga

Gallium catalyst particles were prepared on a plain Ge wafer by evaporation in UHV conditions (sample temperature 360 °C, Ga deposition rate 0.17 ML/min, deposition time 667 s, chamber pressure $2 \cdot 10^{-6}$ Pa). Under these conditions, the catalyst particles of diameter 80–120 nm were formed, see Fig. 15a. Then, germanium was deposited at sample temperature 370 °C or 415 °C, see Fig. 15b,c respectively. The germanium deposition rate was 2 Å·min^{-1}. Neither sample yielded nanowire formation, possibly for two reasons: (i) Based on the observation of a thick 2D germanium layer in between the catalysts, the diffusion length of Ge on the wafer decreases after Ga deposition. Therefore, the Ge supply towards the catalyst particles is not sufficient, see Fig. 15b. (ii) Having increased the sample temperature to 415 °C, the diffusion of Ge supply also increased. Under these conditions, however, the pure Ga catalyst is not stable atop the growing Ge structures, due to the low surface tension of gallium – see the reasoning in the introduction to section 2.3. Therefore, only irregular 3D Ge faceted crystallites are formed; with Ga catalyst unable to pin onto certain facets – see Fig. 15c. Therefore, Ge nanowires were not grown from pure Ga catalyst due to the combination of low Ge diffusion and low Ga catalyst stability.
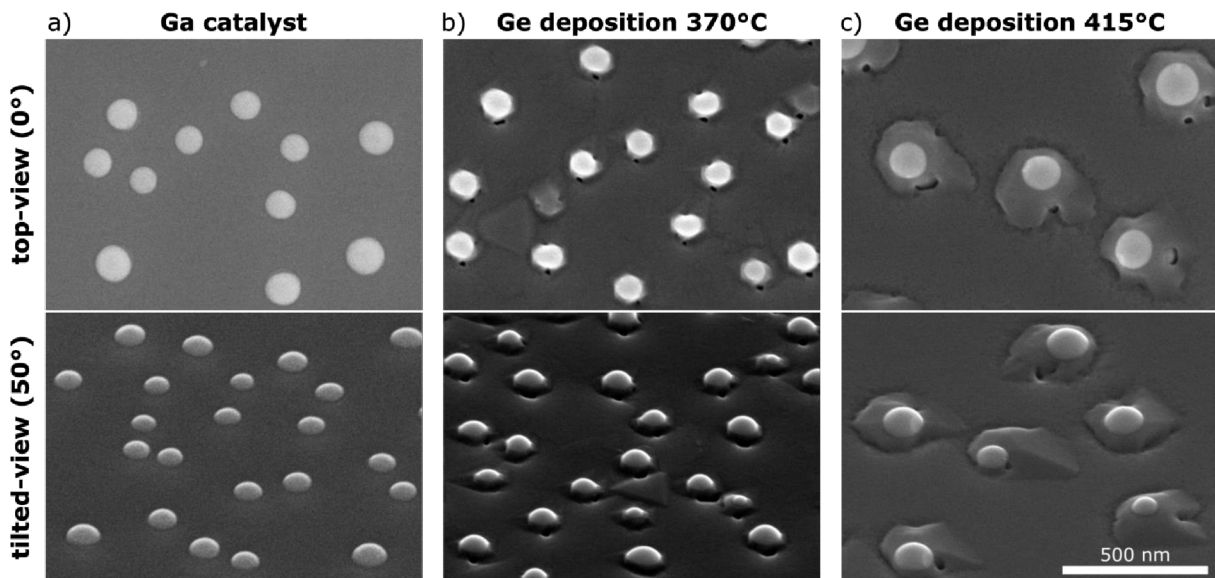
Fig. 15: a) Pure Ga catalyst droplets formed on Ge(111) wafer. b,c) SEM images of Ge structures grown from presented catalysts at sample temperature 370 °C and 415 °C, respectively.

Pure Al

Preparation of Ge nanowires from Al-containing catalyst shall be intriguing for the same reasons as for the gallium catalysts – namely for the possibility of Al incorporation into the nanowire during growth. Indeed, massive catalyst-atom incorporation has been observed for Si nanowires grown by CVD method from Al catalyst [9]. Further, Ke et al. reported [50] that for CVD-grown Si nanowires prepared from Al catalyst, hydrogen termination of the sidewalls increases the surface diffusion of aluminium, see Fig. 16. This is exactly the opposite behaviour than for our Ge/Au material system in the hydrogen atmosphere, presented in detail in section 2.2. These two aspects are the motivation for studying the aluminium catalyst for Ge nanowire growth within our experimental setup.

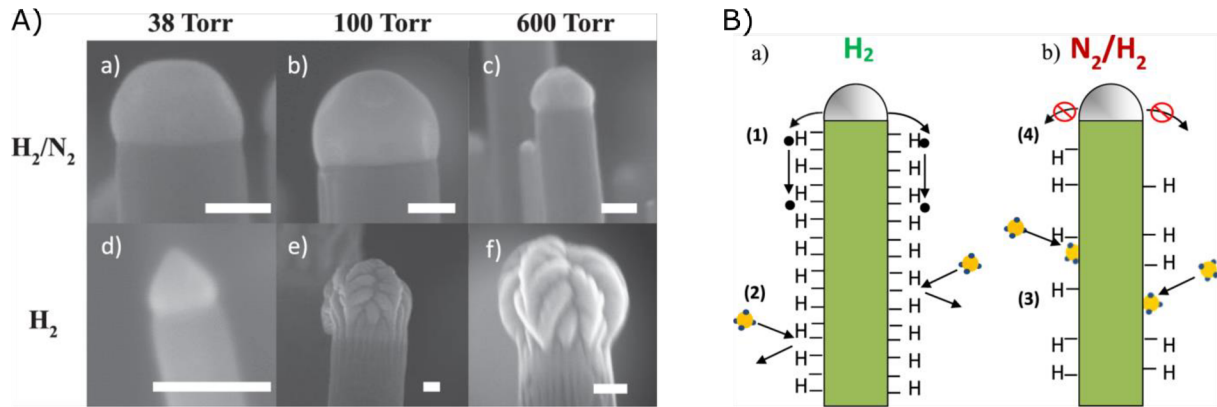**Fig. 16: A)** Top row: Cross-sectional SEM images of Al-catalysed Si nanowire tips grown in H_2/N_2 mix at various total pressure. Bottom row: Nanowire tips grown in H_2 at corresponding total pressure. All scale bars are 100 nm. **B) a)** Growth in hydrogen leads to extensive H-termination on the silicon sidewalls. This leads to significant aluminium diffusion (black dots) along the hydrogen-terminated nanowire sidewalls (1), and reduced thin film deposition (from yellow silane atoms) due to the increase in activation energy required (2). **(b)** Growth in N_2/H_2 mix leads to reduced H-termination. Subsequently thin film deposition is increased, because of the lower energy required (3). Aluminium diffusion is also inhibited due to the increased surface energy of sidewalls (4). Adopted from [50].

The aluminium catalyst particles on Ge wafer were prepared similarly to pure-Ga catalysts – i.e. by evaporation in UHV conditions. Based on the sample temperature, deposition rate and deposition time, the catalyst particles of various diameters were prepared, see Fig. 17.
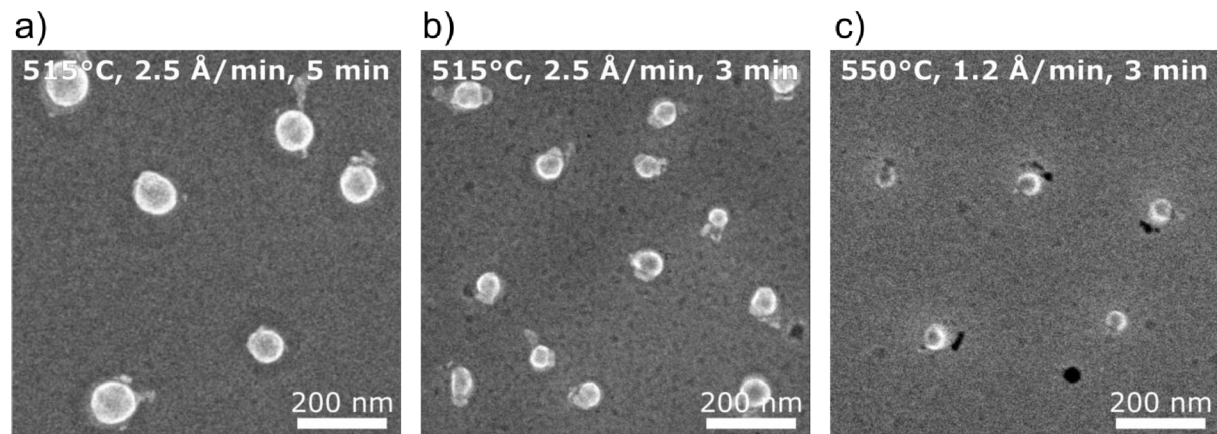
Fig. 17: SEM images of pure Al catalyst particles formed on Ge(111) wafer at various experimental conditions, controlling their size. Sample temperature during Al deposition, deposition rate and length of deposition are inscribed in each image.

For subsequent Ge deposition, catalyst preparation from Fig. 17b was chosen. Again, various Ge-deposition parameters combinations were set and studied – see the inscriptions in Fig. 18 (sample temperature, Ge deposition rate, Ge deposition duration). None of the experimental conditions led to nanowire growth though – see the SEM images in Fig. 18. The nanowire growth inhibitors are the same as described for pure Ga catalysts: The formation of 2D layer between the Al catalyst particles indicates inhibited Ge diffusion on Ge wafer due to aluminium presence. The diffusion-limited area of material supply is confirmed by the dips around the Ge crystallites. When the diffusion is promoted (by higher sample temperature or lower Ge deposition rate), faceted Ge pyramids with Al catalyst on top are formed. However, no nanowire growth was observed.

Fig. 18: SEM images of Ge structures grown from pure Al catalyst at various experimental conditions. The catalyst wa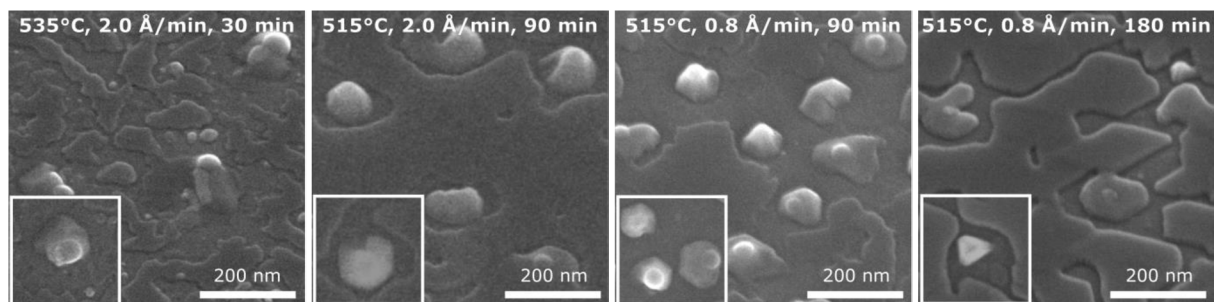s formed by a procedure shown in Fig. 17b. Then, germanium was deposited. Sample temperature during Ge deposition, Ge deposition rate and length of deposition are inscribed in each image.

Alloyed Au–In

Lastly, alloyed Au–In material was studied as a catalyst for Ge nanowire growth. Similarly to Au–Ga catalyst study presented above, two distinct approaches were used: (i) Ge nanowire stem catalysed by pure Au was grown first; then a small amount of indium was co-deposited to form alloyed Au–In catalyst on top of an existing nanowire. Then, Ge deposition and growth continued. (ii) Preparation of alloyed Au–In catalyst on a plain Ge substrate, followed by Ge deposition.

(i) The Ge nanowire stem grown with pure Au catalyst on Ge(111) wafer is shown in Fig. 19a (mind the BSE contrast, highlighting the catalyst material). The growth was performed at sample temperature 410 °C and chamber pressure $7 \cdot 10^{-8}$ Pa. This serves as a reference sample. The other sample was prepared in the same way at first. However, after growing the Ge nanowire stem, indium was co-deposited in the middle of the growth procedure, while Ge supply continued. The equivalent film thickness of deposited indium was 0.45 nm. A typical resulting structure is shown in Fig. 19b. As clearly seen from the SEM micrographs, indium deposition in the middle of the growth leads to catalyst instability. The nanowire loses the catalyst from its top and no longer continues to grow. Instead, a 3D pedestal starts to grow at the nanowire base. To conclude, adding indium to a stable Au catalyst leads to catalyst instability atop the nanowire. This prevents the nanowire from further stable growth from alloyed Au–In catalyst.

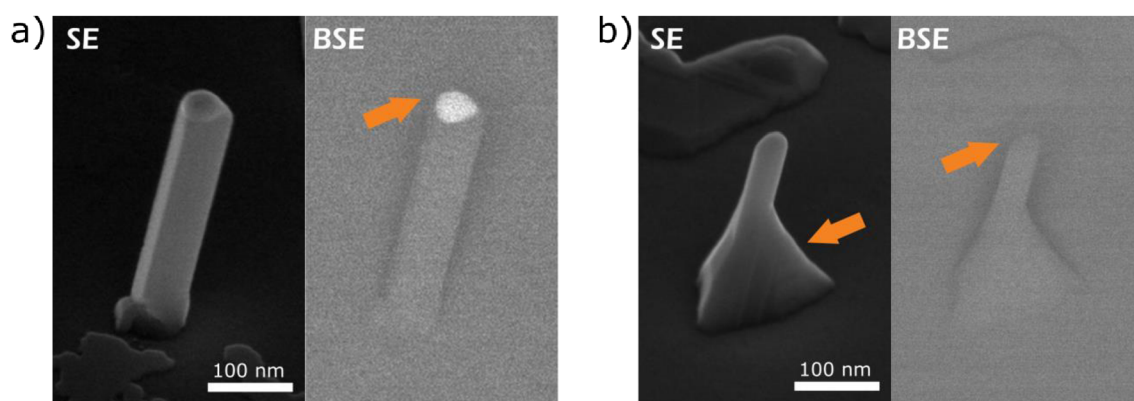**Fig. 19:** a) Ge nanowires grown from pure Au catalyst on Ge(111) wafer. b) Unsuccessful growth of Ge nanowires from alloyed Au–In catalyst. First, Ge nanowire stem was grown from pure Au (similar to Figure a). Without interrupting Ge deposition, 0.45 nm of indium was co-deposited to form an alloyed Au–In catalyst. The catalyst became unstable and moved away from the nanowire top, which leads to 3D growth of Ge at the nanowire base.

(ii) The second approach is to form alloyed Au–In catalyst first (on a plain Ge wafer) and only then to start Ge evaporation, potentially leading to nanowire formation. The catalysts were formed by drop-casting of Au nanoparticles (40 nm diameter) from colloidal solution onto the Ge wafer, followed by indium deposition onto the heated sample in UHV conditions. The catalyst composition is governed by the amount of deposited indium. To illustrate this process, see the SEM images of the catalysts in Fig. 20a. After cooling down for ex-situ imaging at room temperature, the alloyed mixture has separated into Au core and In shell. Different size of Au core is due to clustering of original Au nanoparticles.

The growth of Ge structures from the alloyed catalyst on (111)-oriented Ge wafer is illustrated in Fig. 20b. The catalyst was formed by deposition of 0.45 nm of indium at sample temperature 400 °C, the growth was performed at 380 °C. No nanowires were formed on the sample. Truncated Ge pyramids were grown from the catalysts, which remained on top of these structures. Also, a 2D Ge layer is observed in between the catalysts, indicating low Ge diffusion on the wafer. Therefore, the Ge supply towards the catalyst is inhibited and nanowire growth is not achieved. A number of other growth experiments with different combinations of sample temperature and indium amount were performed with similar results; none of them led to nanowire growth.

Interestingly, the growth from the same Au–In catalyst performed on (110)-oriented Ge wafer leads to the formation of in-plane Ge nanowires, see Fig. 20c. The bi-metallic catalyst remains stable, see the BSE-contrast image. The sample temperature during growth was 395 °C, chamber pressure $1 \cdot 10^{-9}$ Pa.
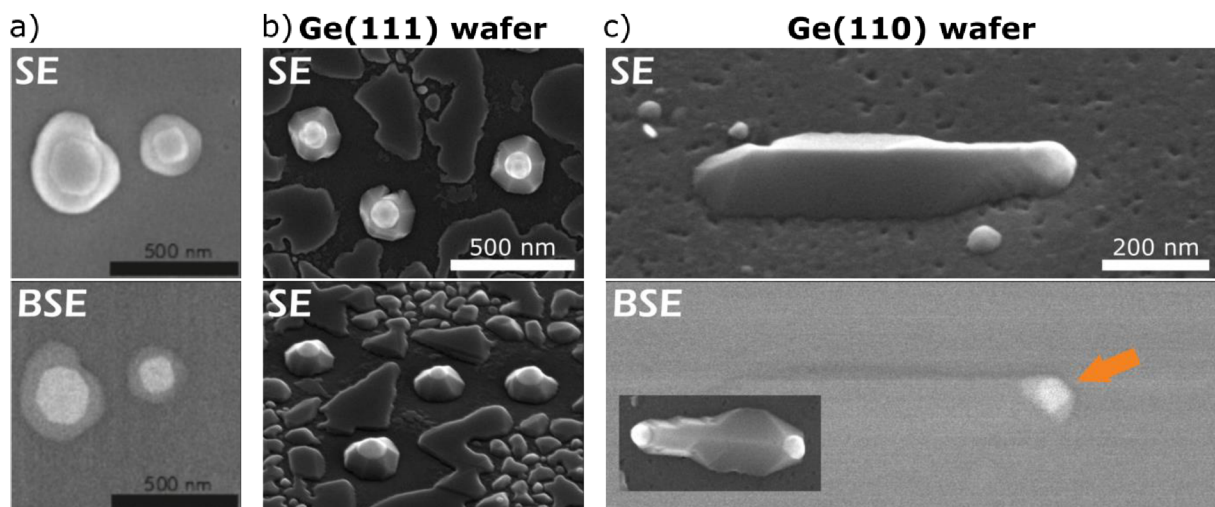
Fig. 20: a) SEM top-view images of bi-metallic Au–In catalyst formed on Ge(111) wafer. The images were taken after cooling down to room temperature, hence the material separation. b) SEM images of Ge structures grown from alloyed Au–In catalyst formed on Ge(111) wafer. Top: top view, bottom: tilted view (50° to surface normal). c) Ge nanowires grown from alloyed Au–In catalyst formed on Ge(110) wafer. The alloyed catalyst remains stable throughout the growth.

3 Preparation of doped ZnO nanowires

Zinc oxide is a direct-bandgap semiconductor material attracting long-lasting attention both in scientific research and industry. Its wide bandgap (3.37 eV at room temperature [94]) corresponds to the UV region (wavelength of 368 nm). It belongs to a class of transparent conductive oxides. Furthermore, it can be doped with group-III metals to very high doping levels. The electron concentration of such highly-doped n-type ZnO may reach up to 10^{21} cm^{-3} [4; 94–96]. Due to its electronic properties, zinc oxide is an attractive material for applications in electronics [59], piezoelectronics [94] and optoelectronics (e.g. UV detectors) [97]. Moreover, highly-doped ZnO nanowires represent a promising material system for bio-sensing applications, as their plasmon resonance frequency may be tuned with dopant concentration down to the near-infrared region [98]. The plasmon resonance frequency in the near-IR to mid-IR region is needed to detect molecular fingerprints in the spectra.

This chapter is dedicated to the characterization of the nominally undoped ZnO nanowires grown via the aerosol-assisted CVD method (AACVD) at atmospheric pressure; and subsequently, to diffusional doping of such nanowires with gallium. These nanowires are then characterized and gallium doping levels are analysed.

Chapter 3 consists of several parts. A literature review is presented in section 3.1, with emphasis on ZnO electronic properties and correct interpretation of its Raman and XPS spectra. The results of the AACVD method for the growth of ZnO nanowires are briefly introduced in section 3.2. Next, section 3.3 is focused on the characterization of the ZnO nanowires in their as-grown state and upon annealing in different oxidative environments. Finally, diffusional doping of the ZnO nanowires with gallium is addressed in section 3.4.

All of the measurements, imaging and data analysis presented in sections 3.3 and 3.4 were done by the author, if not stated otherwise. The exceptions are the TEM imaging and STEM EDS acquisition, EBL and I–V curve measurements and PL detection. However, the data analyses from these measurements were performed already by the author of the thesis himself.

3.1 Literature review

Structural properties

Zinc oxide evinces high radiation hardness and a low coefficient of thermal expansion. This material is non-toxic, biocompatible and biodegradable [99]. For easier understanding, let's summarize the very basic crystallographic terms used when discussing ZnO growth. Its wurtzite (WZ) crystal structure is schematically depicted in Fig. 21a, with lattice constants $c = 5.207$ Å and $a_w = 3.249$ Å [100]. The WZ structure is composed of two inter-penetrating hexagonal close-packed (hcp) sub-lattices, each of which consists of one type of atoms (Zn and O). These sub-lattices are displaced along the [0001] axis by the amount of u. In the non-distorted hcp structure, the c/a ratio is equal to $\sqrt{8/3}$ (≈ 1.633) and u equals $3/8 \cdot c = 0.375 \cdot c$. In most wide-bandgap (WBG) semiconductors such as ZnO and GaN, however, u departs from the $3/8$ value [101]. For ZnO, the reported measured parameters vary slightly in the following range: $c/a \approx 1.539$ to 1.604; $u \approx 0.383c$ to $0.386c$ [102].

25

ZnO is piezoelectric, based on the fact that its crystal structure is non-centrosymmetric. Further, ZnO is also pyroelectric – its WZ structure (contrary to zinc-blende) exhibits spontaneous polarization in equilibrium (i.e. a nonzero dipole moment P_{SP} per unit volume at zero strain) due to its polar character [99; 101]. (The direction of P_{SP} is determined by the orientation of the so-called unique polar axis, which for group-III-nitrides and ZnO is the $\langle 0001 \rangle$ axis.) Although the unit cell of ZnO is electrically neutral, the planes of cations (Zn) alternate with planes of anions (O) along the [0001] direction (also called c direction) – see Fig. 21b. By convention, the vector going from the metallic cation (empty circle in Fig. 21b) and pointing toward the anion (filled circle) defines the [0001] direction, i.e. the positive sense of the c-axis. A structure is said to be metal polar when its growth direction is [0001]. Reciprocally, a structure (growing in double-layers) is said to be anion polar when its growth direction is [000$\bar{1}$]. To get the plane designation straight: {0001} = c-plane (it is polar), {11$\bar{2}$0} = a-plane (non-polar); {1$\bar{1}$00} = m-plane (non-polar) – see Fig. 21b and the 3D sketch in Fig. 21c. There are of course more low-index planes, e.g. {10$\bar{1}$1} (polar; not common for ZnO) or {11$\bar{2}$2} (semi-polar). Semi-polar planes are defined as {$hkil$} planes with a nonzero h, k, or i and nonzero l Miller–Bravais index [101].
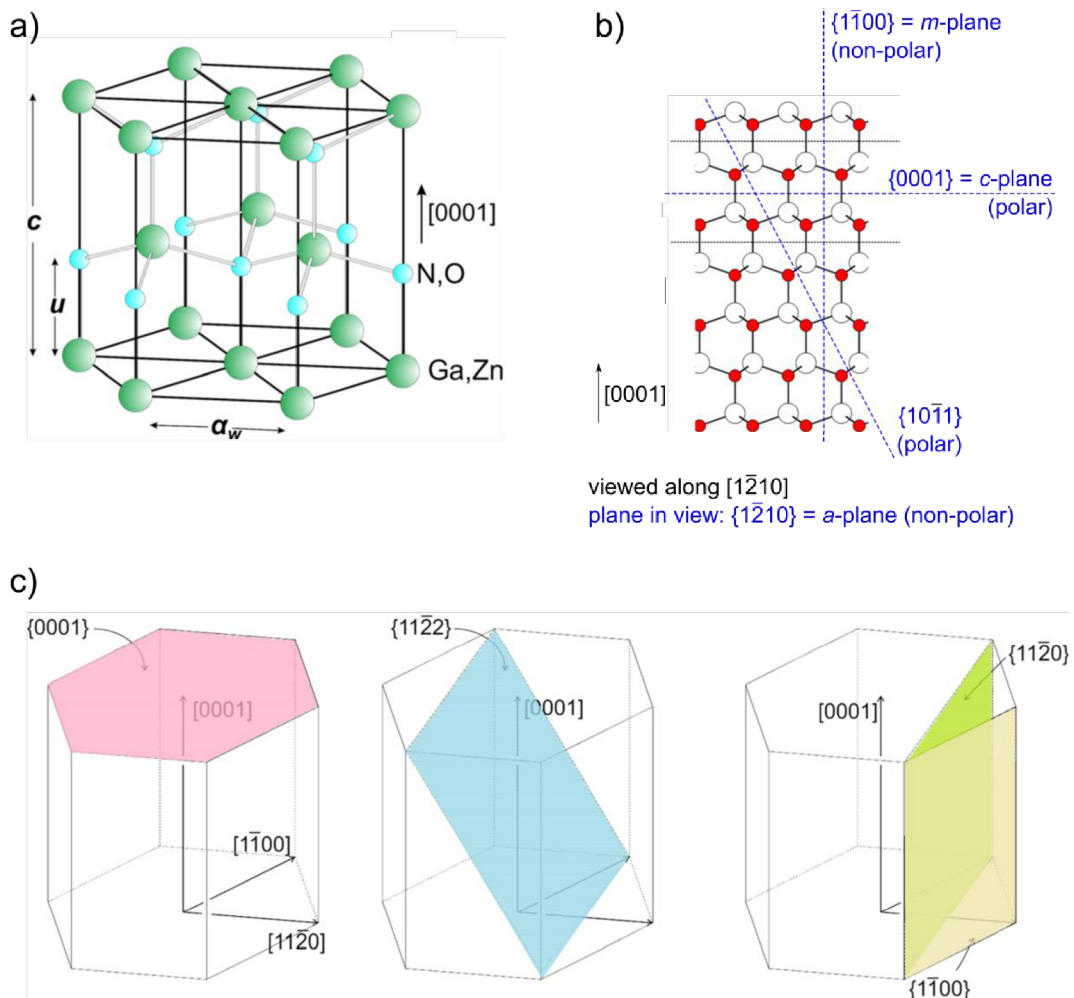
Fig. 21: ZnO crystallography. Adapted from [101]. a) Ball and stick model of the wurtzite ZnO (or GaN) structure. The a_W and c are the lattice constants; u is the displacement of the O- and Zn-sublattice along the [0001]-axis. b) Ball and stick model of wurtzite crystallographic planes. Open (filled) circles correspond to cations (anions), respectively. c) Schematic representation of selected low-index planes in the WZ crystal.

Note that there are two possible crystallographic notations: If the crystal planes in hexagonal systems are indexed using Miller indices, then the crystallographically equivalent planes have indices that appear dissimilar. To overcome this, the Miller–Bravais indexing system is used. See the comparison in Fig. 22 or an instructive animation in [103].
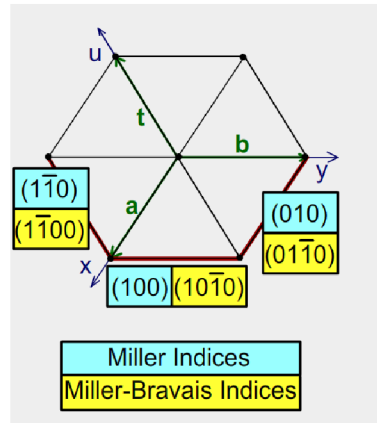

Fig. 22: Indexing of hexagonal crystals – comparison of Miller indices and Miller–Bravais indices for a set of crystallographically equivalent planes (highlighted by red colour). Adopted from [103].

Electronic characteristics

Zinc oxide is a II–VI semiconductor with a direct and wide bandgap in the near-UV region (3.37 eV at room temperature; 368 nm). Both spontaneous and stimulated emission has been demonstrated (UV lasing, blue and UV LEDs) [99; 104; 105]. The bandgap engineering of ZnO is possible via alloying with MgO or CdO (similar to Al or In effect in GaN) – see Fig. 23. ZnO highly doped with aluminium (AZO) or gallium (GZO) is used in electronics as electrodes (transparent conducting oxide applications) [95]. Degenerated ZnO semiconductor may be studied by APT, characterizing the dopant clustering [95]. Zinc oxide shows high electron mobility, high thermal conductivity and high exciton binding energy (60 meV, being promising for optoelectronics at/above room temperature) [99]. Regarding electronic and optoelectronic applications, ZnO is foreseen to supersede and outperform GaN once the challenge of its stable and reliable p-type doping is solved [94]. The thing is that ZnO shows asymmetric doping behaviour (frequent for WBG or II–VI semiconductors [95]) – it is intrinsically n-type, extrinsic n-type doping is easy up to high levels, p-type doping proves difficult but possible.
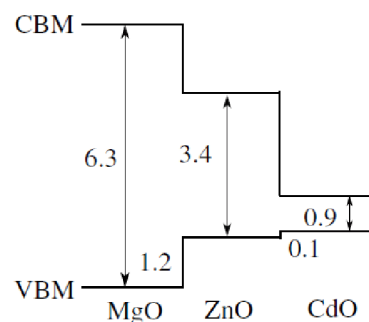
Fig. 23: Schematics for ZnO bandgap engineering – see the values for a bandgap of ZnO, MgO and CdO (in eV). Alloying ZnO with MgO or CdO leads to bandgap widening or narrowing, respectively. Adopted from [94].

The origin of the intrinsic n-type behaviour of ZnO has been a long-standing mystery. A common view in the past was (and a number of current papers claim as well) that it is caused by Zn interstitials or mainly by O vacancies acting as donors (see e.g. [106]). However, the DFT calculations and ODEPR

27

(optically detected electron paramagnetic resonance) measurements have shown that point defects (of any kind) are not likely to be responsible; O vacancy shall be a *deep* donor and Zn interstitials have high formation energy [94]. Janotti and Van de Walle (ibid.) point out that previous experimental reasoning was based on *indirect* evidence (like oxygen partial pressure during growth); however, other simultaneous effects can occur. For example, a decrease of oxygen pressure may lead to O vacancy formation or instead to easier H incorporation at O sites. Uncontrolled impurity incorporation during growth or annealing is suggested as a plausible cause of the intrinsic n-type behaviour. Particularly, hydrogen is suggested. It is inevitably present in the majority of growth and processing environments. (Indeed, both hydrothermally-grown and melt-grown ZnO single crystals are reported to contain at least 0.3 at.% of hydrogen, being often the highest-concentration impurity [107].) Hydrogen interstitials (H_i) are *shallow* donors based on DFT calculations; however, they are highly mobile and diffuse easily – therefore they cannot explain high-temperature unintentional n-type doping. On the other hand, substitutional hydrogen at O sites (H_O) – being a shallow donor as well – is much more stable than H_i up to 500 °C. Moreover, it can explain the dependence of conductivity on oxygen partial pressure (wrongly attributed to O vacancies) [94]. Note that, interestingly, there is a historical precedent for such paradigm shift in doping understanding for GaN (cited from [94]):

> *"It may still take some time for the community to adjust to this point of view, but the precedent of GaN may be informative. Until the early 1990s, the overwhelming consensus in the field was that GaN exhibited unintentional n-type conductivity due to nitrogen vacancies, and that p-type GaN would be extremely difficult or even impossible to achieve. Computational studies then showed that nitrogen vacancies are high-energy defects that are highly unlikely to occur in n-type GaN. Instead, n-type conductivity was attributed to unintentional impurities such as oxygen. This view proved to be correct and within a few years the perception of the role of point defects completely changed, and the focus was shifted to the importance of controlling impurity incorporation. ZnO will likely follow this historical precedent."*

Elsewhere [95], Ellmer and Bikowski rediscover *"forgotten knowledge from the 1950s, which have faded away"*, that hydrogen was viewed as a donor of ZnO. Experimentally, hydrogen has been proved to be a shallow donor by sputtering in Ar+H_2 atmosphere, with the benefits of resistivity decrease, passivation of interface and bulk defects (leading to improvement of electrical and optical properties), reducing depletion regions (especially at the grain boundaries). Still, the intrinsic n-type doping of ZnO is far from being completely understood with new papers emerging even in favour of O vacancies again. Often, the experiments show different results than the calculations. For a richer story, see also [96; 108–111]. Recently, also donor-like complexes involving point defects and unintentional impurities are suggested as an explanation – arguing for either (i) nitrogen-containing complexes [110; 112], or (ii) V_{Zn}–3H complexes (formation of three interstitial hydrogen atoms and a zinc vacancy; bringing the attention back to hydrogen yet again) [113] acting as shallow donors with low formation energies – the latter being corroborated by cathodoluminescence measurements, Raman spectroscopy and DFT calculations.

As mentioned earlier, *intentional* n-type doping of ZnO is a routine process, details of which depend on the particular growth method. This topic is widely covered both computationally and experimentally (see e.g. the reviews in [94; 95]). The most used dopants are aluminium, gallium and indium – they are incorporated into Zn lattice sites (substitutional doping). ZnO doped with Al, Ga

and In (or their combination in the co-doping strategies) exhibits low resistivity and high carrier concentration (up to 10^{21} cm^{-3}). At donor concentration above 10^{20} cm^{-3}, the electrical activation of the dopants is often less than 100 %, due to (i) the formation of dopant–defect complexes, (ii) the compensation of the electrons by acceptors (O_i, V_{Zn}) and (iii) the formation of secondary phases, for instance, Al_2O_3, Ga_2O_3 etc. Also, there is a strong dependence on different deposition methods and annealing conditions [95]. High dopant concentrations (even above the equilibrium solubility limit) are often reported [95; 114; 115].

The ZnO nanowires doping strategy to be applied in this thesis is similar to that described in [116]. There, undoped ZnO nanorods were grown first. Then they were over-deposited with aluminium thin film and subsequently annealed in high vacuum. At optimum conditions, the surface Al atoms completely diffused into ZnO nanorods, resulting in Al-doped ZnO nanorods. The thickness of Al thin film deposited was 2–8 nm; the nanorods were annealed at 500–600 °C for 4–6 hours under high-vacuum conditions (10^{-3} Pa). The Al concentration was reported to be estimated to 5 at.% from a STEM EDS spectroscopy, with uniform Al distribution and no crystal damage.

Regarding p-type doping of ZnO, it remains a challenging task with controversial results. As sharply pointed out by Ellmer and Bikowski [95], experiments are ahead of theory in this field:

> *"Though many DFT calculations can be found in literature, irrefutable conclusions from these calculations cannot be drawn. It seems that the experimental situation (defect complexes, self-compensation, phase separation etc.) is too complex to be described by the current (DFT) theory. The long-searched-for theory of doping of II–VI semiconductors is still missing."*

From the experimental point of view, most of the device applications requiring p-type ZnO (LEDs, LDs, photodiodes) have been realized by N- or Sb-doped ZnO or ZnMgO, which proves the feasibility of achieving ZnO p-type doping [110]. More and more, the dopant or dopant–defect complexes are suggested as a theoretical explanation of successful p-type doping. Also, co-doping is being investigated with promising results (in ADA, AA or AI arrangement; A = acceptor, D = donor, I = isovalent element) [110].

Electrical transport measurements

Plenty of transport measurements of ZnO nanostructures and nanowires has been published. In order to present a grasp of the experimental layout and the overall characteristics, measurement ranges, electrode materials etc., see e.g. [117; 118], the extract of which is shown in Fig. 24. Both authors use Ti/Au electrodes, which form Ohmic contacts with the n-type In-doped (a) and nominally undoped (intrinsically n-type) (b) ZnO nanowires. In Fig. 24a, a diameter dependence of I–V curves is seen. However, the specific resistivity (2.0·10^{-2} Ω·cm) remains independent of the nanowire dimensions [117]. The diameter of the nanowire in Fig. 24b is 62 nm. Note the different scale for doped and undoped nanowires. Regarding the electrode materials for either Ohmic or Schottky contacts formation with differently doped ZnO, a comprehensive review is presented in [119].
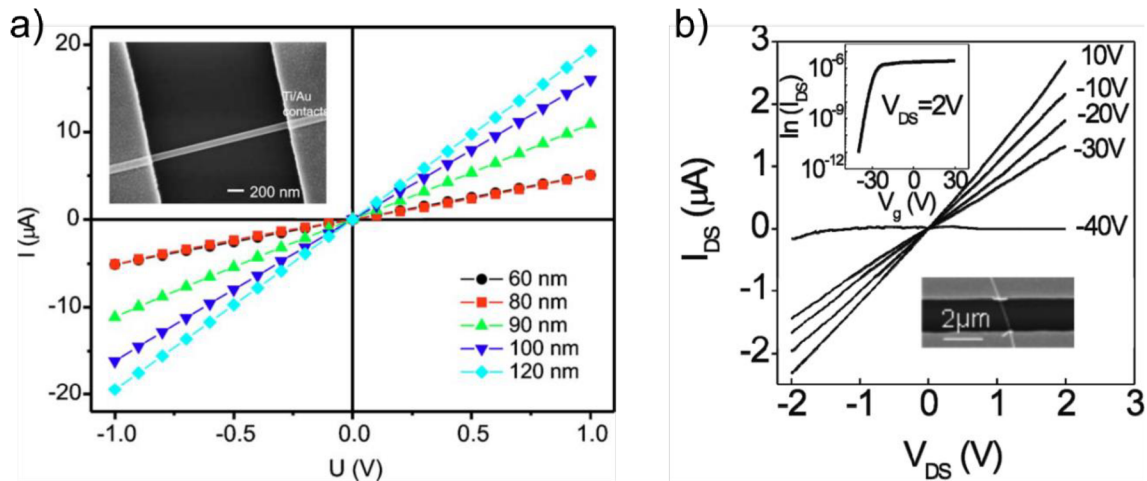
Fig. 24: Electrical transport measurements of ZnO nanowires. a) Indium-doped n-type ZnO nanowires with different diameters, measured at room temperature in high vacuum. The inset shows an SEM image. The distance of the metallic leads is 2.63 µm. Adopted from [117]. b) Undoped (intrinsically n-type) ZnO nanowire. The diameter is 62 nm, the effective gate length is 2.2 µm. Measured at room temperature in the air. The upper inset shows the $\ln(I_{DS})$–V_g plot at V_{DS} = 2 V; the lower inset is an SEM image of the FET. Adopted from [118].

An important topic with respect to electronic-measurement interpretation is the ZnO surface electron accumulation/depletion layer, interconnected with the surface chemistry (presence of surfactants and adsorbates) and also surface ZnO polarity (having a compensation effect); impacting the conductivity measurements. A decrease of conductivity in n-type ZnO was observed for measurement in the oxygen atmosphere, whereas hydrogen caused conductivity increase. The effect is opposite for p-type ZnO. Also, when measured in humid air, the water film causes electrochemical pinning of the Fermi level [101; 111; 113; 118–123]. Note that this performance is highly promising for sensing applications. It is important also for photo-detection applications (UV detection) [122]. The presence of a surface electron accumulation layer is suggested as one of the factors that complicate the measurement of p-type conductivity in ZnO [94].

Raman spectroscopy – pure ZnO

Due to a long-standing interest in zinc oxide material, its properties are well-characterized and described in the literature. The structure of wurtzite ZnO belongs to C_{6v}^4 class (Schönflies notation) and to P6$_3$mc space group (Hermann–Mauguin notation) [124; 125]. Therefore at Γ point of the Brillouin zone, there are six Raman-active optical phonon modes in the first-order spectrum, classified as E$_2$(low), A$_1$(TO), E$_1$(TO), E$_2$(high), A$_1$(LO) and E$_1$(LO) at 99, 377 (or 374), 410, 437, 574 (or 581) and 583 cm^{-1}, respectively (different authors report slightly different values; the A$_1$(LO) and E$_1$(LO) modes are often considered together as LO mode at 579 cm^{-1}). The A$_1$ and E$_1$ modes represent two polar branches, which split into LO and TO components with different frequencies, owing to macroscopic electrostatic forces within the polar crystal [124]. The two E$_2$ branches are non-polar – while the low-frequency mode E$_2$(low) is associated with the Zn sub-lattice, the high-frequency mode E$_2$(high) involves the oxygen sub-lattice. Further, there is a double-phonon mode E$_2$(high)–E$_2$(low) at 333 cm^{-1}. Interestingly, a Raman line attributed to hydrogen interstitials in bond-centre sites acting as donors typically lies around 330 cm^{-1}, thus overlapping with the E$_2$(high)–E$_2$(low) mode [126]. Next, there is a weak second-order 2-E$_2$(low) mode at 204 cm^{-1} and several second-order modes in the range of 1000–1200 cm^{-1}. Besides, A$_1$ and E$_1$ modes are infrared-active. Note that there are also two B$_1$ modes, which are both Raman and infrared silent (i.e. forbidden) [127–130]. Milano et al. [131] reports that B$_1$ modes may be allowed by the breakdown of translational crystal symmetry due to the

30

presence of defects (so-called defect-induced forbidden modes of the original ZnO lattice). Indeed, the B_1(low), 2-B_1(low) and B_1(high) modes have been observed in Ga-doped (and Al-doped) ZnO thin films at 275 (275), 504 (508) and 620 (644) cm^{-1}, respectively [132].

For ZnO nanowires with their c-axis oriented perpendicular to the substrate surface (i.e. parallel to the laser wave propagation direction, as will be the case of our samples), the A_1(TO), E_1(TO), and E_1(LO) Raman modes are forbidden [129]. Still, the A_1(TO) and E_1(TO) peaks will be discussed in the following chapters, as they appear in the spectra of our samples, presumably due to imperfect nanowire alignment and the presence of lattice defects (see the samples' morphology in section 3.2).

The frequency of the E_2(high) mode at 437 cm^{-1} is strain-sensitive, hence informative whether the ZnO nanowires are free of strain or not [129].

Raman spectroscopy – doped ZnO

ZnO thin films and nanowires doped with various elements were the subject of Raman spectroscopy studies as well. Escobedo-Morales and Pal report that incorporation of Ga has no strong effect on the lattice parameters and crystallinity of ZnO nanostructures, whereas In and Sb doping introduce considerable lattice distortion [128]. Micro-Raman measurements of ZnO thin films doped with Fe, Sb, Al and Ga and In showed additional modes at about 277, 511, 583 and 644 cm^{-1}, not specific to any particular element [127; 128; 130]. Instead, host lattice defects induced by doping are suggested as their origin – their positions agree well with the above mentioned defect-induced forbidden B_1 modes. The partial loss of crystallinity of the ZnO nanostructures due to dopant incorporation is verified by XRD measurements (see [128] for indium, specifically). Further additional modes at 531, 631 and 720 cm^{-1} seem specific for Sb, Ga, and Fe dopants, respectively. Li doped ZnO did not reveal additional modes [130]. For Ga-heavily-doped ZnO nanowires, the ZnO Raman peaks are reported to get smaller and broader as Ga content increases, indicating the lattice disorder. Besides, additional peaks emerge (at 691 cm^{-1} and the already-mentioned ones) [133].

An exemplary study of tuneable doping of vertically-standing ZnO nanowires with aluminium is presented in [129], including temperature-dependent Raman spectroscopy. The frequencies of the ZnO Raman modes remain unchanged. Again, additional modes (AM) are observed upon nanowire doping at 276, 509, 623, 643 and 856 cm^{-1}; the 276 cm^{-1} peak (labelled AM1) being the highest – see Fig. 25 for illustration. Bear in mind that (i) these modes are *not* aluminium-specific and that they are reported by other authors as well (read above) and (ii) the positions of these peaks correspond to the defect-induced forbidden B_1 modes of ZnO lattice, as also mentioned earlier [132]. Another additional mode has been reported in the range of 579–584 cm^{-1} [129]. Therefore it overlaps with ZnO A_1(LO) mode, resulting in a single peak at 581 cm^{-1}. The intensity ratio of this A_1(LO)+AM peak over E_2(high) mode is systematically larger for higher Al-doping. In order to visualize the growing intensity of the additional peaks with increased doping concentration, the Raman spectra were normalized in intensity with respect to the E_2(high) Raman line. This means that the intensity ratio of additional mode vs. ZnO E_2(high) mode is increasing for higher dopant concentration (valid for all observed additional modes). Furthermore, the intensity ratio of the E_2(low) over E_2(high) modes remains identical for different doping levels. The intensity ratio of the E_2(high)−E_2(low) over E_2(high) mode is constant regardless the doping concentration. However, it increases with temperature (reversibly). Temperature-dependent measurements (ibid.) indicate that the doping is thermally

activated at a low threshold temperature of 200 °C. The additional modes then remain visible even after cooling down to room temperature.
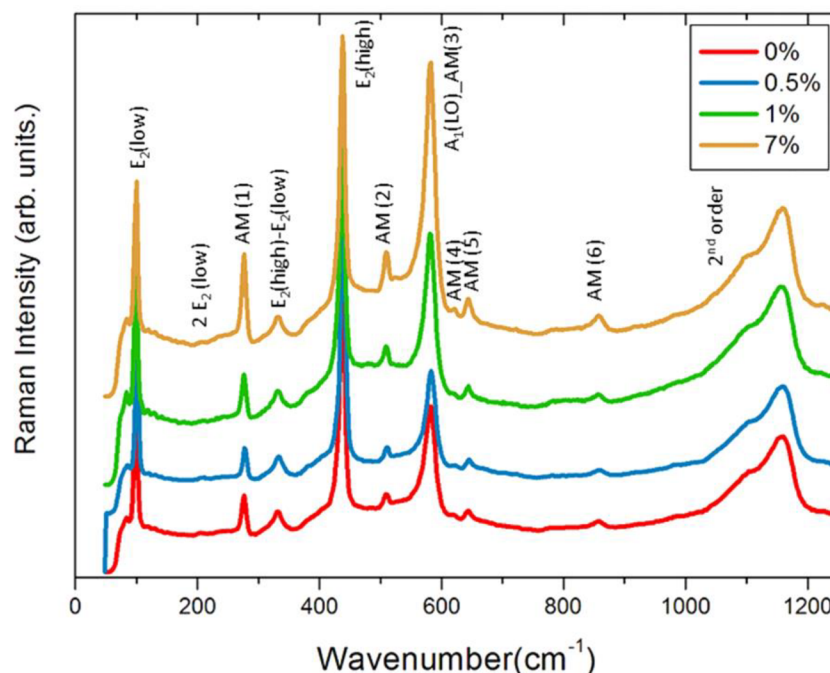

Fig. 25: An illustration of Raman scattering spectra of n-type doped ZnO nanowires. Adopted from [129]. Note that the legend does _not_ present the amount of Al in the nanowires directly; it only shows its trend based on the growth conditions (ratio of Al(NO$_3$)$_3$ over Zn(NO$_3$)$_2$ precursors).

XPS – Oxygen vacancies evaluation (O 1s peak)

Zinc oxide is known for a variety of native point defects (e.g. O and Zn vacancies, interstitials, antisites etc.), the concentration of which is largely dependent on the growth method [122; 125]. (In general, ZnO is differentiated as hydrothermally-grown or melt-grown.) Moreover, the concentration of the point defects may be altered by post-growth treatment. Patently, these crystal defects may alter the dopant incorporation into ZnO lattice [134; 135].

Oxygen vacancies (V_O) are heavily discussed in the literature as a possible origin of the intrinsic n-type doping of ZnO (prevailing reasoning being that they are too deep donors to provide the n-type doping; still acting as effective compensation centres for p-type doping, which proves extremely challenging for ZnO). Leaving aside this dispute, it remains important to be able to characterize the V_O concentration in the samples used, as it may influence the incorporation of group-III dopants; and vice-versa, it may be increased by dopant incorporation [109; 116]. Also, oxygen vacancies are reported to result from ZnO annealing in high vacuum. Reversely, their concentration decreases upon annealing in an oxidative atmosphere [94; 95; 136].

The amount of oxygen vacancies in ZnO can be monitored by X-ray photo-electron spectroscopy (XPS). The O 1s peak is composed of three components ([97; 116; 132; 137; 138]; originally described and discussed for In$_2$O$_3$ material in [98]), attributed to:

- Oxygen ions (O^{2-}) in the WZ structure of bulk ZnO crystal (low-binding-energy peak)
  Peak centre range: 529.7–530.9 eV

- Oxygen ions (O^{2-}) in oxygen-deficient regions of ZnO lattice, i.e. in the vicinity of O vacancies (intermediate-energy peak)
Peak centre range: 531.0–532.0 eV
- Oxygen ions (O^{2-}, O^-, O_2^-) (loosely) bound to ZnO surface – in the form of adsorbates and contamination (–OH, –COOH, –CO_3 bonds, adsorbed H_2O or O_2^-) and/or in the topmost layer of ZnO (high-energy peak)
Peak centre range: 532.2–533.1 eV

Thus, the O 1s peak can be fitted with three Voight profiles. Specific energies of the peak components differ paper-to-paper (probably due to unequal XPS setup and calibration). Generally, the spacing between low-energy and intermediate peak centres is 0.6 to 1.1 eV; for intermediate and high-energy peak it is 0.8 to 1.3 eV. Gabás et al. [132] assign the intermediate peak to oxygen linked to dopant cations (Ga, Al); however, it may also be explained by the oxygen vacancies induced by this doping [116]. Note that this peak is observed in undoped samples as well. Pan et al. [115] report a slight increase of the intermediate peak (assigned to oxygen-deficient regions in the matrix) with higher fluorine concentration in the F-doped ZnO nanowires – the oxygen atoms are substituted by fluorine. For the sake of completeness, the Zn peaks do not show any dependency on V_O concentration.

3.2 ZnO nanowires grown via aerosol-assisted CVD

For the research described hereafter, ZnO nanowires prepared by a collaborating researcher Stella Vallejos (Instituto de Microelectrónica de Barcelona) are used. This section 3.2 represents a short summary of the nanowires' growth method and morphology characterization, as published by Vallejos et al. (see [140; 141] for further details). The nanowires were grown via an aerosol-assisted CVD method at atmospheric pressure (AACVD). This method leads to structured growth of metal oxides without the need for catalyst seeds, i.e. via the vapour–solid (VS) mechanism; and what's more, at relatively low temperature compared to other CVD methods. Here, nanowires grown at 400 °C on a silicon wafer (using $ZnCl_2$ + ethanol solution) are employed.

Quasi-aligned nanowires of two distinct morphologies can be grown – called rods and needles in further text, see Fig. 26. Needle-like structures are grown when a higher aerosol flux is applied. Based on published XRD and TEM examination, both types are single-crystalline with preferential growth in the [001] direction. As a remnant of the growth process, low chlorine contamination is present (determined with EDS; Cl:Zn = 0.05 at.%). The lattice spacing determined by HRTEM is consistent with the literature for ZnO and with the (002) plane identified by XRD. The two morphologies exhibit different aspect ratios and wetting properties (which might be important for sensing applications). XPS measurement of O 1s peak suggests that the surface of needle-like structures is oxygen-deficient. Note that in Fig. 26c,f, the crystallographic notation using the Miller indices is applied. When transformed into Miller–Bravais indices (see section 3.1), the conversion is as follows: {100} -> {10$\bar{1}$0}, {111} -> {11$\bar{2}$1}, (001) -> (0001). Thus the nanowire sidewalls consist of non-polar m-plane ZnO; the top facet is a polar c-plane. The (001) top facet of rod-like nanowires is O-polar, as determined via etching experiments [142].
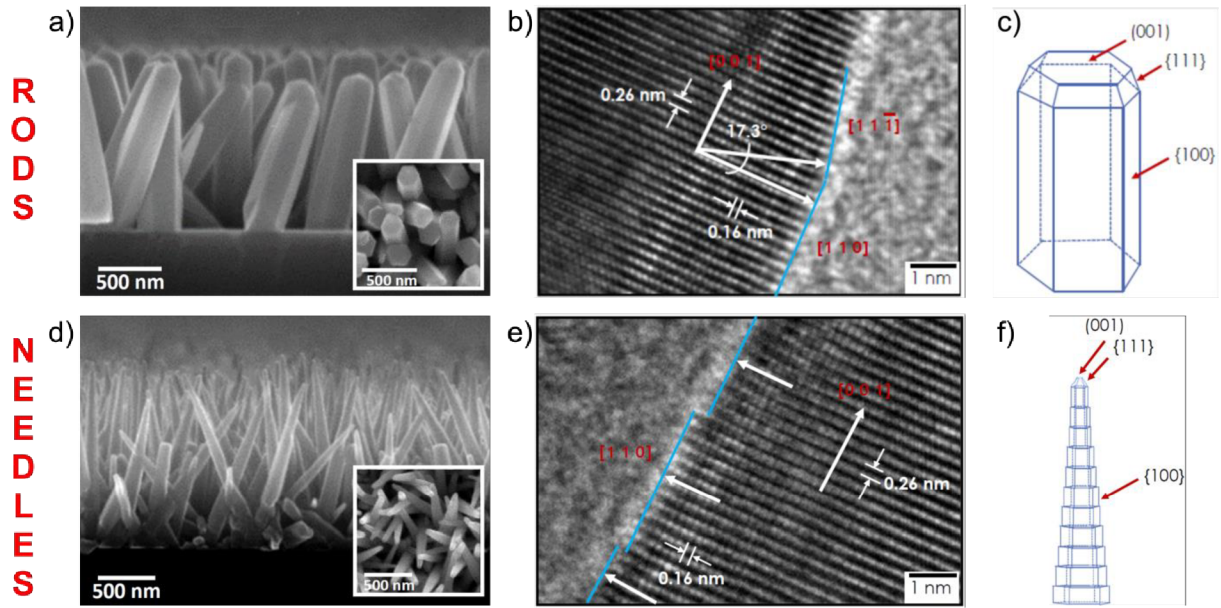
Fig. 26: ZnO whiskers grown by the AACVD method, further used for the doping study: nano-rods (a,b,c) and nano-needles (d,e,f). a,d) SEM image showing side-view of the sample. Inset: top view. b,e) HRTEM image viewed along $[\bar{1}10]$ direction. c,f) Schematics of nanowire facets orientation. Image courtesy: S. Vallejos [140].

3.3 Characterization of as-grown and annealed nanowires

Basic characterization of the as-grown ZnO nanowires, as performed by Vallejos et al., has been presented in section 3.2 above. However, further characterization of the nanowires is needed for the purpose of this thesis. Therefore, additional characterization is presented in the following text. Namely, TEM characterization, Raman spectroscopy and electrical transport measurements of the as-grown nanowires and XPS characterization of nanowires annealed in various environments were performed.

Please note that various samples from several growth batches were inspected within sections 3.3 and 3.4. As the growth conditions may slightly differ for individual batches, the samples' batch number will always be indicated when discussing the results. The batch-number assignment of the studied samples is summarized in Table 1.

Table 1: Assignment of the batch number to individual ZnO samples.

Batch No.	Samples
Batch-1	samples used in section 3.3 for TEM, transport and Raman measurements (except the black spectrum in Fig. 32 and blue in Fig. 33) V_O-rich and V_O-poor samples used in section 3.4.2 for AES, STEM EDS and PL measurements
Batch-2	see Fig. 40b
Batch-3	samples used in: - Fig. 33 (Raman study of different batches) - section 3.4.1 for SEM (except Fig. 40b and Fig. 42c), Raman, XPS and HRTEM analysis
Batch-5	see Fig. 42c
Batch-6	samples used in section 3.3 for XPS analysis upon annealing

TEM characterization

TEM characterization of as-grown ZnO nanowires grown via the AACVD method has been already presented in section 3.2, see Fig. 26 (earlier research of S. Vallejos et al.). In order to have a reference for future measurements of doped nanowires and to confirm the crystal quality of the ZnO nanowires currently used, an as-grown nanowire from a rod-like sample has been characterized anew with TEM, see Fig. 27a,b.

The sample preparation is following: The nanowires grown on Si substrate were sonicated in deionized water for 1.5 hours and then drop-casted (3 droplets per 2 µl) onto a SiN membrane (200 nm holey SiN support membrane). Prior to inserting into TEM, the membrane with nanowires was plasma-cleaned for 5 minutes to avoid contamination during imaging (argon 75 %, oxygen 25 %; Fischione plasma cleaner Model 1020). Then, the samples were characterized using ThermoFisher Titan Themis 60-300 TEM.
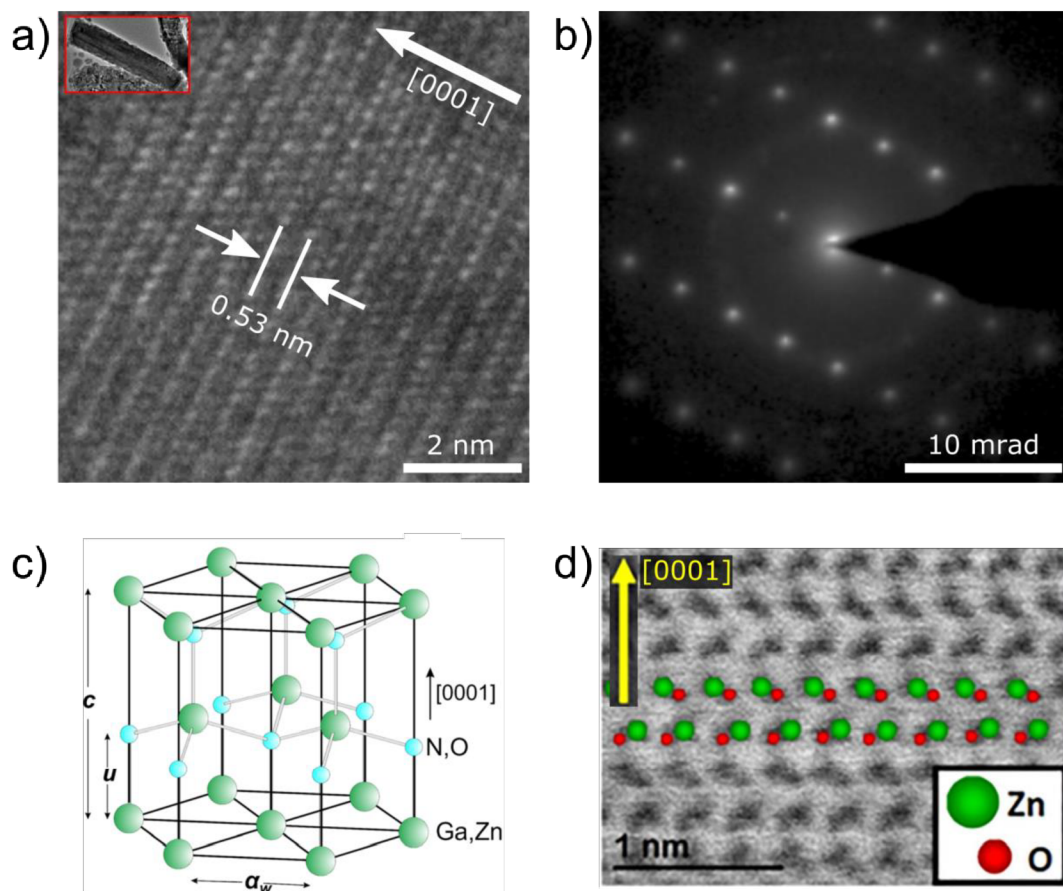
Fig. 27: As-grown ZnO rod-like nanowire. a) HRTEM image of the NW. In the inset, an overview TEM image of the same orientation is shown. Notice the inter-layers in between the 0.53nm period. b) Diffraction pattern taken from the NW shown in a) – the orientation is preserved. Imaging of a),b): K. Bukvišová. c) Ball-and-stick model of the wurtzite ZnO structure. The *c* is the lattice constant along the [0001]-axis. Similar to a), notice the inter-layer of atoms in the middle. Adopted from [101]. d) Atomic resolution Cs-corrected ABF-STEM image of a ZnO nanowire. Adopted from [101].

The TEM inspection of the nanowire confirms its high crystal quality, being a single-crystal throughout the nanowire – see the HRTEM image in Fig. 27a and microdiffraction in Fig. 27b. The measured value of lattice constant *c* along the [0001] growth axis (0.53 nm) is in agreement with published values (0.52 nm in [100; 110]). For a correct interpretation of the (S)TEM measurements, it is important to keep in mind the WZ crystal structure of ZnO, illustrated in Fig. 27c. Within the lattice

constant *c*, there is another double-layer of atoms. However, the Zn and O atoms in this inter-layer are oriented in a different way, which is nicely imaged in Fig. 27d. Therefore, the period is really 0.52 nm and not 0.26 nm (which is also confirmed by diffraction). This is important in order to avoid confusion when interpreting HRTEM and STEM images, where a clear signal from the inter-layers is present, but the orientation of the Zn–O doublet cannot be distinguished. For example, see the inter-layers in Fig. 27a and Fig. 26b,e (HRTEM) or the STEM image in Fig. 27d.

Raman characterization

Keeping in mind the goal of the thesis – to exhibit and characterize Ga doping of the ZnO nanowires – Raman spectroscopy is one of the possible characterization methods to be used (see the literature review in section 3.1). Firstly, it is necessary to characterize the as-grown ZnO rods and needles (see their morphology above in Fig. 26) in order to have a solid reference frame for Raman measurements of doped nanowires. The instrument Witec Alpha 300 R was used for Raman measurements; with a 532 nm excitation laser of 10 mW power. Grating 1800 g/mm was used. The acquisition time was 300 s.

Raman data handling procedure was as follows:

- The characterized samples consisted of nanowire ensemble still attached to the Si growth substrate, i.e. quasi-vertically aligned. (No sonication nor Raman characterization of individual nanowires was performed.)
- Before each data acquisition, a linear scan in z-direction was performed. The focus was adjusted to achieve the highest signal intensity.
- Raman spectrum acquisition.
- Spectrum calibration with respect to the Si peak (i.e. spectrum shift in the frequency-axis).
- For detailed spectra of individual Raman peaks, the background was fitted locally with a linear function and subtracted.
- When helpful, the spectra were normalized (for easier comparison of peak position shift, its full width at half maximum – FWHM – and the ratio of peaks' intensities).

The first aim of the Raman study of the aforementioned nanowires is to establish reference spectra of both rods and needles in the as-grown state (i.e. as-received from S. Vallejos). In this initial stage, two samples of ZnO rods (labelled rods-1 and rods-2) and a sample of ZnO needles were characterized. All of them come from the same growth batch (which will prove to be important as seen in Fig. 33). Note that sometimes both rods and needles coexist on the sample, presumably due to slight variations of the growth conditions.
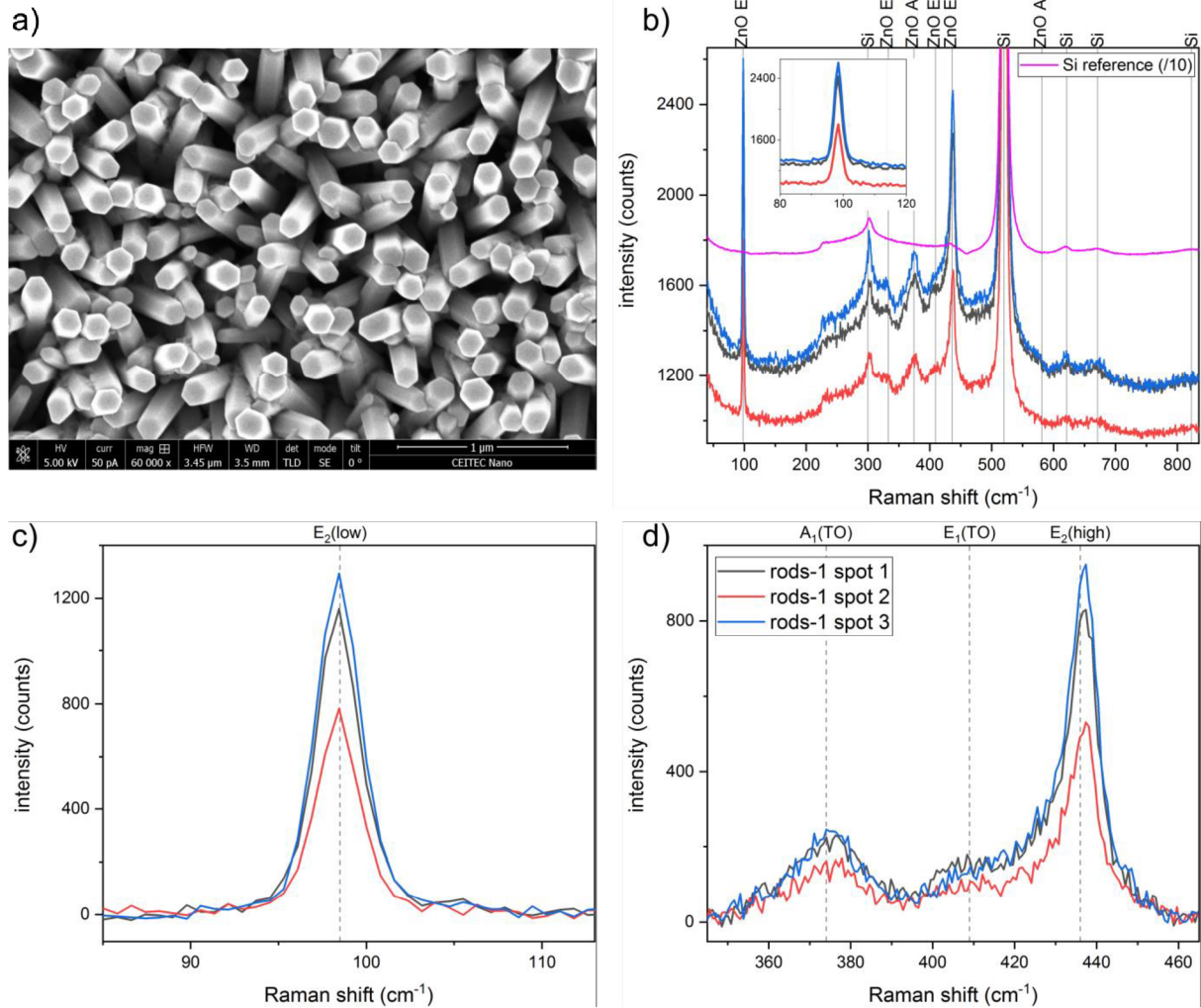
Fig. 28: ZnO rod-like nanowires, sample labelled rods-1. a) SEM top-view image. b) As-measured Raman survey spectra taken at different positions (spot 1 to 3). Si growth substrate measurement is included (purple; signal intensity divided by a factor of 10). c,d) Detailed Raman spectra of ZnO E$_2$(low) and E$_2$(high) peaks, respectively. The legend is common for all graphs.

As an example of the scope of sample characterization, the results from the rods-1 sample are shown in Fig. 28. It presents the top-view SEM image of the sample (Fig. 28a) and the survey Raman spectra taken from various spots on the sample (Fig. 28b). Note that the background signal differs significantly. A reference measurement of a silicon wafer is included. Generally, several peaks are visible, the most prominent corresponding to ZnO nanowires (E$_2$(low) at 98 cm^{-1} and E$_2$(high) at 437 cm^{-1}) and Si growth substrate (300 cm^{-1} and 520 cm^{-1}). The peaks assignment is inscribed in the Figure above the spectra, based on the literature review summarized in section 3.1. Note the shoulder (small peak) at around 585 cm^{-1} corresponding to ZnO A$_1$(LO) mode – it is present for the as-grown samples already. This peak is badly visible due to the overlap with the silicon peak at 520 cm^{-1}. Also, the ZnO E$_2$(high)–E$_2$(low) mode at 333 cm^{-1} is visible, but overlapping with another Si peak. Even after subtracting the background, the height of ZnO E$_2$(low) and E$_2$(high) peaks is different for individual positions on the same sample (see Fig. 28c,d, respectively). This might correspond to a different volume of ZnO nanowires measured at various spots on the sample. The results for the other rod-like sample (rods-2) were analogous (not shown here).
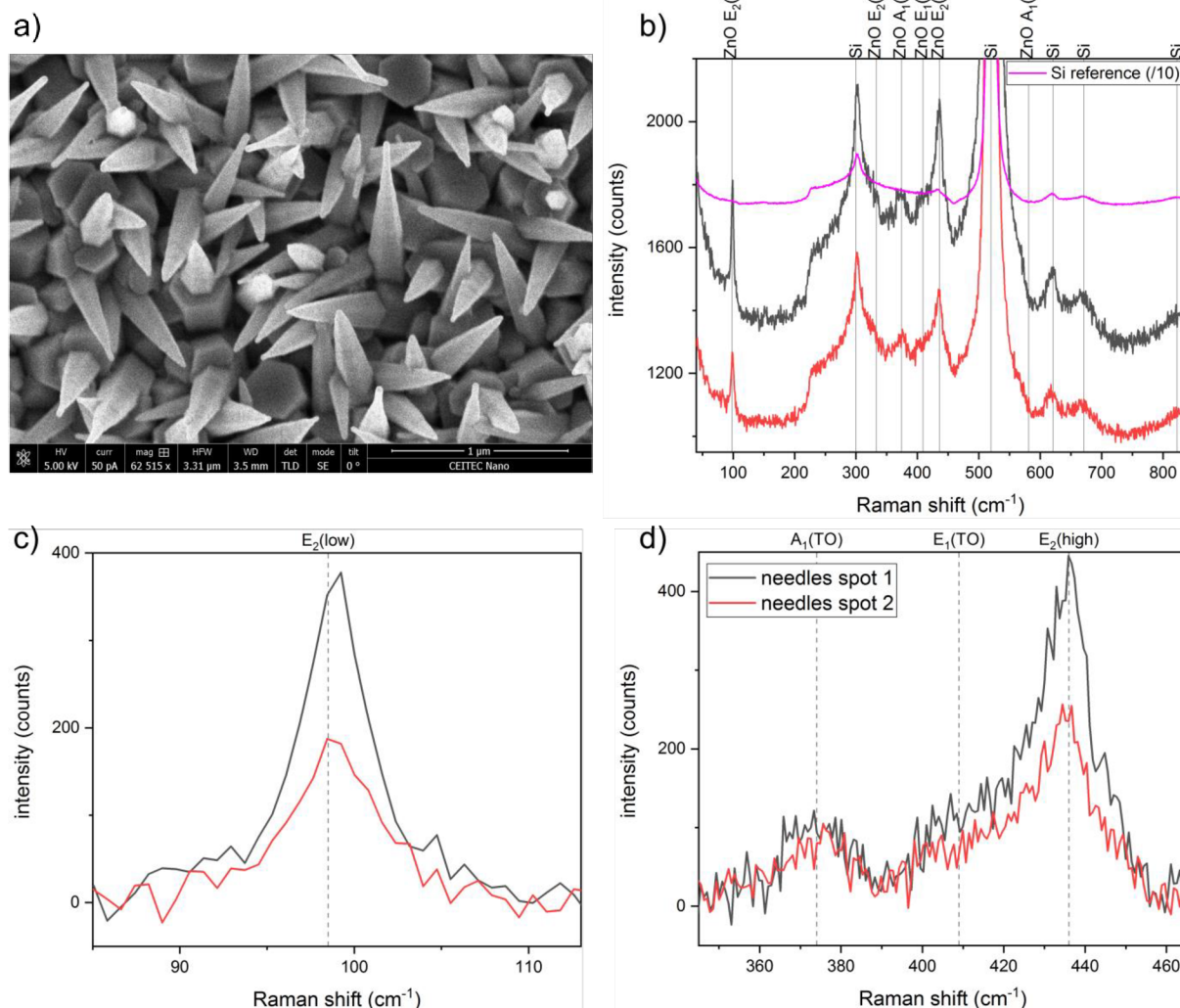
37

Fig. 29: ZnO needle-like nanowires. a) SEM top-view image. b) As-measured Raman survey spectra taken at different positions. Si growth substrate measurement included (purple; signal intensity divided by a factor of 10). c,d) Detailed Raman spectra of ZnO E_2(low) and E_2(high) peaks, respectively. The legend is common for all graphs.

The results obtained from the needle-like sample are shown in Fig. 29. Two different positions on the sample were examined. Similar to rod-like samples, the background signal and the peak heights differ spot-to-spot. Contrary to rod-like samples, a worse signal-to-noise ratio is observed and the Si peak at 300 cm^{-1} is more intense than ZnO E_2(low) and E_2(high) peaks.

Given that the ZnO E_2(low) and E_2(high) peaks height vary not only sample-to-sample but also at different positions on the same sample, one needs to find a quantity or invariant that stays constant i) for different spots of the same sample and ii) for different as-grown samples of the same morphology. Only then it is possible to compare those quantities between rods and needles (both in the as-grown state) and to see the potential changes after the process of gallium doping.

Regarding the as-grown samples, the ZnO E_2(low) peak position and FWHM stay constant for all places on both rod-like samples as is clearly seen in Fig. 30a showing normalized spectra. On the contrary, the needle-like sample exhibits larger E_2(low) FWHM (moreover different for various positions) and its position is slightly shifted. Regarding ZnO E_2(high) peak, the findings are similar: For

needles, the FWHM increases with respect to the rods and the peak position shifts slightly; see Fig. 30b. The FWHM values are presented in Table 2. The ZnO A_1(TO) peak appears to be similar for both rods and needles (see ibid.).
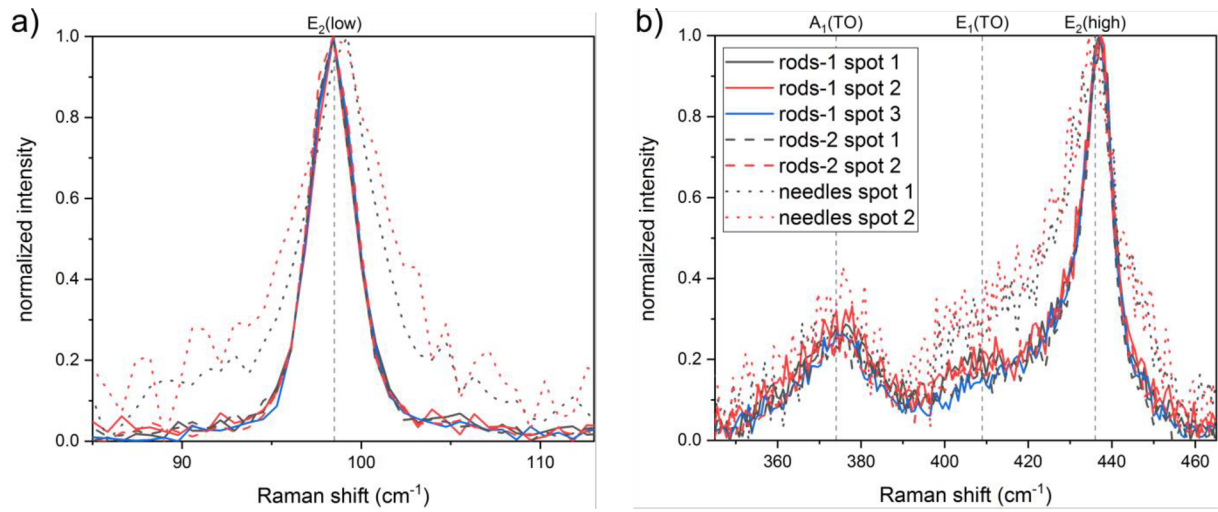

Fig. 30: a,b) Normalized Raman spectra of ZnO E_2(low) and E_2(high) peak, respectively. Each sample was measured at various positions. A direct comparison of peak width and peak height ratios is visible. The legend is common for both graphs.

Further, let's focus on comparing the peak height ratios. Three ratios are studied, namely E_2(low) over E_2(high), A_1(TO) over E_2(high) and E_1(TO) over E_2(high). The results are summarized in Table 2 for both rods and needles. The intervals are inclusive of all the measured values for different spots. Based on the results, the E_2(low):E_2(high) ratio can be used to distinguish the rod-like and needle-like morphology of ZnO nanowires (>1 for rods, <1 for needles). The other peak ratios are compared qualitatively looking at Fig. 30b and commented on within Table 2.

Table 2: Comparison of Raman measurements' outcomes for as-grown ZnO nanowires of rod-like and needle-like morphology.

	Rods	Needles	Comments
AS-GROWN NANOWIRES			
E_2(low) FWHM	3.0 cm^{-1}	4.7 to 6.2 cm^{-1}	see Fig. 30a needles – different for various positions
E_2(high) FWHM	9.6 cm^{-1}	15.8 to 18.6 cm^{-1}	see Fig. 30b needles – different for various positions
A_1(TO) peak	similar FWHM and position		see Fig. 30b
E_2(low):E_2(high) ratio	1.37±0.11	0.79±0.06	>1 for rods, <1 for needles
A_1(TO):E_2(high) ratio	0.26±0.07	0.34±0.07	see Fig. 30b similar; high variance in measured values possible invariant for the as-grown samples
E_1(TO):E_2(high) ratio	lower	higher	see Fig. 30b

To conclude this section: The rod-like and needle-like ZnO nanowire samples exhibit different Raman spectra, regarding ZnO E_2(low) and E_2(high) peak positions and FWHM and also their ratio. This implies the different quality of their crystal structure (I hypothesise on surface defects due to the inclined sidewalls morphology of needles); therefore they shall be regarded individually when utilized for further experiments. On the other hand, the study of different rod-like ZnO samples shows that the results are equivalent and thus pose a good Raman reference for further doping studies. Therefore, only rod-like samples will be examined further.

The experimental procedure for diffusional gallium doping of the nanowires are described in detail below (see section 3.4). The first step of the process is annealing of the as-grown nanowires either in high-vacuum conditions or in H_2O_2 atmosphere. Therefore, it is necessary to investigate whether and how the Raman spectra change after such heat treatment. The annealing conditions were chosen with respect to the results of the XPS study of differently-annealed samples shown below – see Fig. 38 and the related discussion. Annealing in vacuum or H_2O_2 leads to oxygen-vacancy-rich (V_O-rich) or oxygen-vacancy-deficient (V_O-poor) samples, respectively. Further in section 3.4, the impact of O vacancies on gallium incorporation will be studied.

As a reference, previous measurements of rods-1 and rods-2 samples from Fig. 30 are used. Also, to check the repeatability of the measurements, rods-1 sample was measured again at the same time as the annealed samples. The time interval between the measurements was 5 weeks; the new measurement is labelled "rods-1 as-grown later" in Fig. 31. The repeatability is excellent regarding ZnO E_2(low) and E_2(high) peaks. The peak ratios A_1(TO):E_2(high) and E_1(TO):E_2(high) have decreased slightly over that period of time. Further, two other samples were prepared: one annealed in high-vacuum (maximum pressure $1 \cdot 10^{-3}$ Pa) at 400 °C for 30 minutes; the other annealed in H_2O_2 gas (3 kPa) at 535 °C for 30 minutes. Each of those samples was measured at two positions. Fig. 31a shows that the ZnO E_2(low) peak is not affected by either type of annealing; the peak position and FWHM stay the same as for the as-grown samples. The same applies to the ZnO E_2(high) peak, see Fig. 31b. The peak ratio E_2(low):E_2(high) is also similar to as-grown nanowires for both vacuum-annealed and H_2O_2-annealed rods; see the values in Table 3. Also, Fig. 31b shows the other peak ratios: A_1(TO):E_2(high) is the same for as-grown ("rods-1 later") and vacuum-annealed samples, whereas there is a decrease for the H_2O_2-annealed sample. The difference in E_1(TO):E_2(high) ratio is too small to be conclusive. A summary of these results after the nanowires' heat-treatment is shown in Table 3.

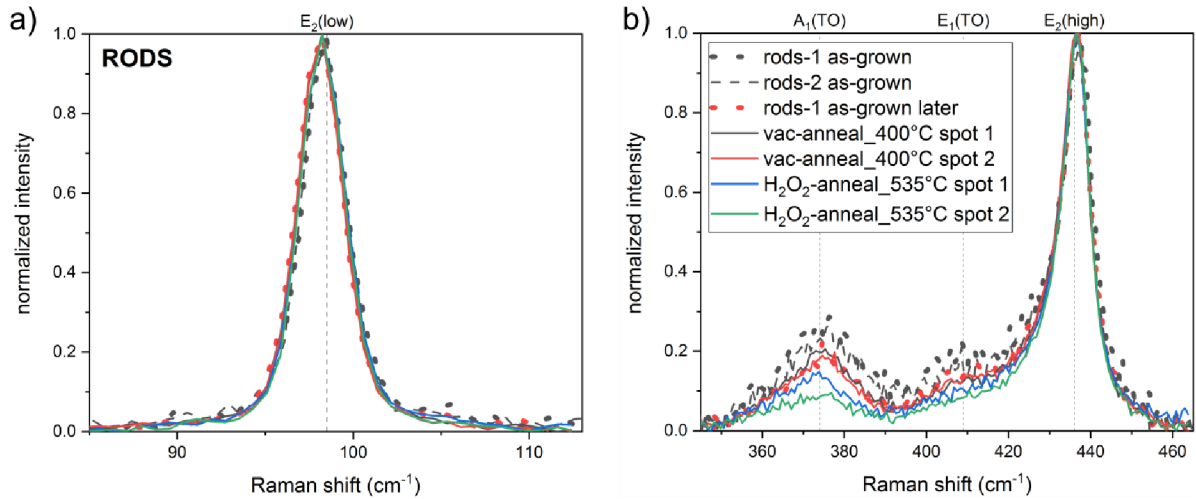**Fig. 31: a,b) Normalized Raman spectra of ZnO E₂(low) and E₂(high) peak, respectively. Repeatability study (rods-1 vs. rods-1 later, time interval 5 weeks) and comparison of the as-grown samples, vacuum-annealed sample (400 °C) and H₂O₂-annealed sample (535 °C). The legend is common for both graphs.**

To investigate the temperature effect, another sample was prepared in the same way as the H₂O₂-annealed one with an additional step of final vacuum-annealing at 535 °C for 30 min without breaking of vacuum. The results are depicted in Fig. 32 and Table 3. The new sample (black spectra in the Figure) shows the same FWHM of the ZnO E₂(low) and E₂(high) peaks as the previous samples, with a slight shift of E₂(low) peak. Also, peak ratio E₂(low):E₂(high) stays similar to previous samples. However, a further decrease of A₁(TO):E₂(high) ratio is observed (0.05±0.02); the A₁(TO) peak vanishes. Taking into account Fig. 32b, one may conclude that the A₁(TO):E₂(high) ratio reduction is a temperature-induced effect combined with an impact of the surrounding atmosphere: Annealing at 400 °C in vacuum gives the same results as the as-grown sample. For nanowires annealed at 535 °C, the ratio decreases. This effect is more pronounced for the sample annealed in H₂O₂ for 30 min and then in vacuum for another 30 min. Still, ZnO E₂(low) and E₂(high) peaks are not affected, hence the ZnO crystal structure does not get degraded by annealing under the aforementioned conditions.

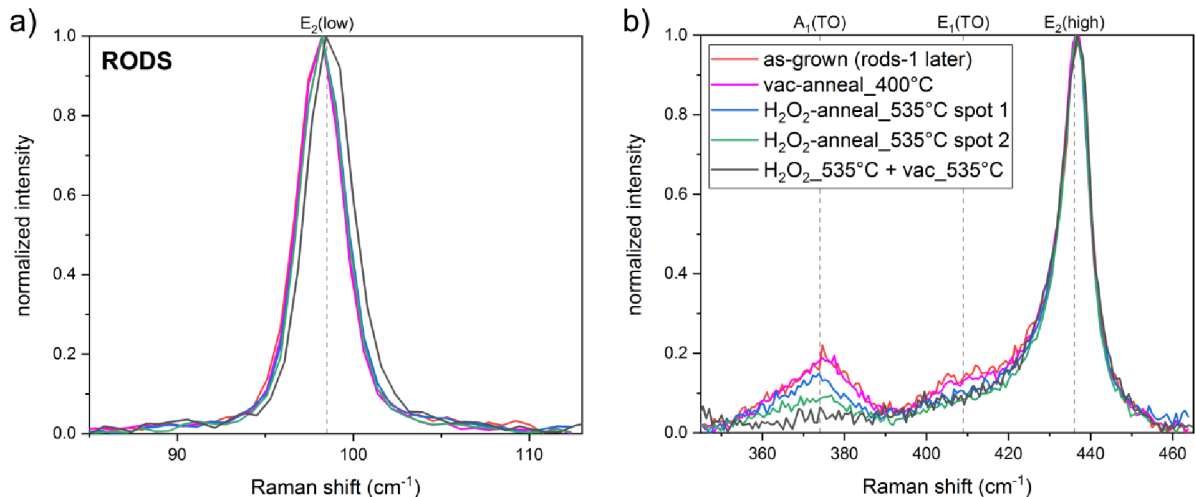**Fig. 32: Combined effect of annealing temperature and environment. Normalized Raman spectra of a) ZnO E₂(low) peak and b) ZnO E₂(high) peak for samples annealed in vacuum (400 °C, 535 °C), H₂O₂ atmosphere (535 °C) and as-grown.**

Table 3: The effect of heat treatment of ZnO rod-like nanowires on Raman measurement outcomes. Annealing was performed at different temperatures and environment. Compare with Table 2 (as-grown nanowires).

	Vacuum-annealed 400 °C	H$_2$O$_2$-annealed 535 °C	H$_2$O$_2$-annealed + vacuum-annealed 535 °C	Comments
AFTER HEAT-TREATMENT (ROD-LIKE NANOWIRES ONLY)				
E$_2$(low) FWHM	not affected by any heat treatment; same as the as-grown			see Fig. 31a, Fig. 32a
E$_2$(high) FWHM	not affected by any heat-treatment; same as the as-grown			see Fig. 31b, Fig. 32b
E$_2$(low):E$_2$(high) ratio	1.45±0.04	1.41±0.03	1.35±0.04	all similar to the as-grown rod-like nanowires (1.37±0.11)
A$_1$(TO):E$_2$(high) ratio	same as for as-grown	decreased	further decreased (no 374 peak visible)	see Fig. 31b, Fig. 32b

Up to now, all of the samples described originate from the same growth-batch (excluding the last sample, annealed both in H$_2$O$_2$ and vacuum). As several growth batches are used in the following study, it is necessary to check and exclude the dependency between the batch number and the results. In order to demonstrate the impact of the growth-batch number on the results of Raman measurements, two as-grown rod-like samples from different batches were characterized, see Fig. 33. The data for the *Batch-1* sample are the same as rods-2 in Fig. 31. The results for the other sample (from *Batch-3*) are strikingly different: The ZnO E$_2$(low) and E$_2$(high) peaks are shifted and show significantly larger FWHM. Regarding the E$_2$(low) peak, the FWHM is 3.0 cm^{-1} for *Batch-1* sample and 7.0 cm^{-1} for *Batch-3* sample. Furthermore, the peak ratio E$_2$(low):E$_2$(high) shows inverse behaviour: It is 1.4 for *Batch-1* and 0.8 for *Batch-3* sample. There are also differences in the A$_1$(TO):E$_2$(high) and E$_1$(TO):E$_2$(high) peak height ratios, see Fig. 33b. To conclude, a great difference in Raman spectra is seen for the as-grown ZnO nanowires of the same morphology, prepared within different growth batches. Therefore, the Raman measurements shall be evaluated separately within each individual growth batch. Moreover, these results indicate quite diverse crystalline quality of ZnO nanowires prepared within different growth batches of the AACVD growth process used (albeit showing the same morphology in SEM micrographs).
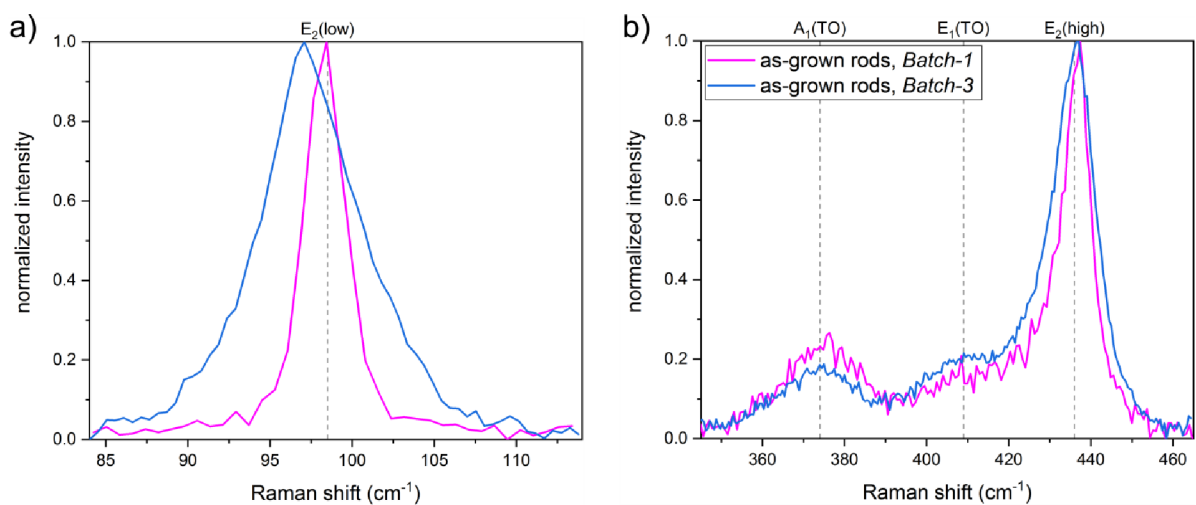

Fig. 33: Impact of growth-batch selection on ZnO Raman spectra. Normalized Raman spectra of two rod-like as-grown samples from different growth batches. a) ZnO E$_2$(low) peak, b) ZnO E$_2$(high) peak.

Transport measurements

Characterizing the transport properties of individual semiconductor nanowires is not a trivial task. One of the techniques utilized for doping characterization is the I–V curves measurement. In line with the research goals of this thesis, representative rod-like ZnO nanowires in the as-grown state were characterized. The nanowires from sample rods-1 (*Batch-1*) were utilized (see their morphology and Raman characterization above). The nanowires were scrubbed off with a sharp blade and then sonicated in a vial filled with deionized water. Next, they were drop-casted onto a suitable substrate: Si wafer with a layer of SiO_2 (258 nm thick) over-deposited with a layer of HfO_2 (ALD technique, 20 nm) for better electrical insulation. The electrical contacts were prepared by electron beam lithography (EBL), using SEM/E-beam writer Tescan Mira 3 and Electron beam evaporator Bestec. The electrical contacts were composed of 6 nm Ti, 240 nm Cu and 20 nm Au (from bottom to top; see the schematics in Fig. 34). Ti-based metallization schemes (often covered by protective Au layer) are reported to form Ohmic contact with n-type ZnO (see the literature review in section 3.1 and Fig. 24). Prior to contacts deposition, the sample was cleaned in oxygen+argon plasma (ratio 80:20) for 15 s to remove the residual resist and ensure a clean interface between the nanowire and metal contacts. The I–V measurements were then performed in dark ambient conditions with a probe-station connected to a parameter analyser, using a two-point method.
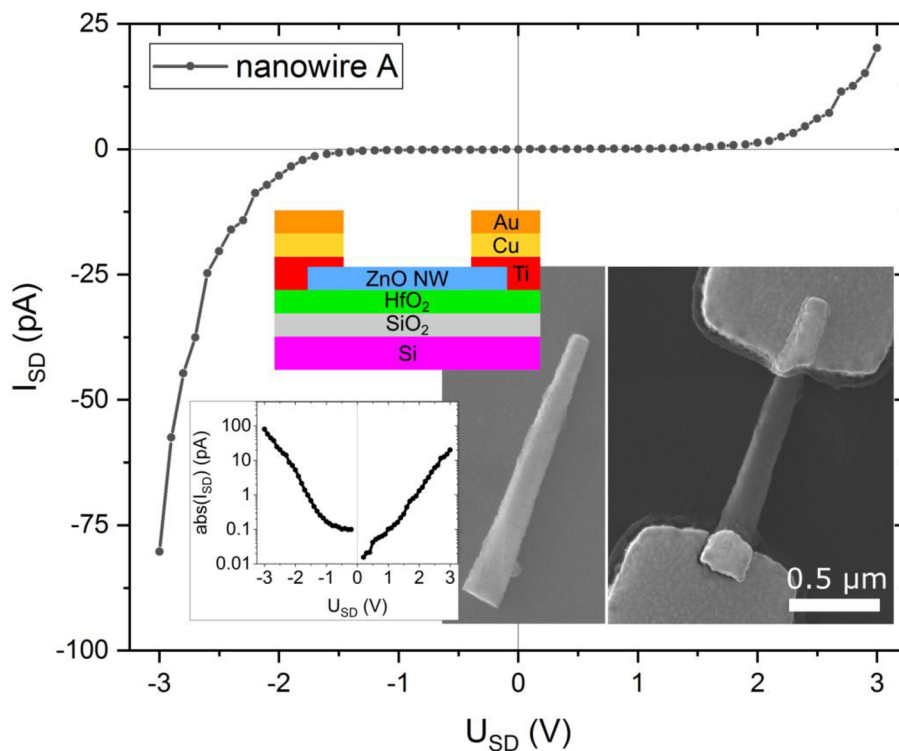
Fig. 34: I–V curve measurement of a rod-like ZnO nanowire in the as-grown state. Colour inset: Layout schematics of materials used (not to scale). White inset: The same measurement in a semi-log scale (absolute value). Dark inset: SEM micrograph of the nanowire before and after metal contacts deposition. EBL and transport measurements: D. Citterberg. Data analysis: author of the thesis.

Two individual ZnO nanowires were characterized (labelled A and B hereafter). The corresponding I–V curve of nanowire A is shown in Fig. 34. In the inset, see the SEM micrographs of the nanowire before and after deposition of electrical contacts. The measurement was done with 1 nA compliance, 1 s hold time, 100 ms delay time and 100 mV step size. A non-linear I–V behaviour is observed in the whole range measured (i.e. −3 V to +3 V). The dependence is exponential, see the inset (straight lines

in the semi-log scale). Moreover, the I–V curve is asymmetric. This implies that the contacts are not Ohmic. Furthermore, the low value of electrical current suggests imperfect contacts with high contact resistance. Indeed, the bottom contact seems broken on the nanowire outline (see the SEM inset).

During subsequent measurements, nanowire A has melted down (probably due to resistive heating owing to bad contacts). Therefore, I–V measurements of another nanowire labelled B will be discussed further in more detail. For the experimental overview, see Fig. 35. The initial I–V measurement is shown as a blue curve in Fig. 35b (see the inset for a better scale). Note the value of maximum current of circa 400 pA. Similarly to nanowire A, non-linear behaviour is observed. Subsequently, repeated I–V measurements were performed (for source–drain voltage going in cycles 0 V – up to max voltage – down to 0 V – down to min voltage – up to 0 V). The maximum current during the measurements was limited to 10 μA by compliance. Gradually, the conductivity increased in such a way that the measured current increased by four orders of magnitude, see the red spectrum in Fig. 35b. This I–V curve is also more linear and more symmetrical, compared to the initial measurement. However, fully linear behaviour was not reached, still indicating non-Ohmic contacts. (Hypothetically, even if the I–V curve was linear, the resistivity calculated based on simplified geometry would be in the order of 10^0 Ω·cm, further suggesting high contact resistance. Such a high value of resistivity is two to three orders of magnitude higher than reported in the literature, see e.g. the measurements shown in Fig. 24b.)

In order to understand this enormous change in conductivity, the sample was imaged by SEM (Fig. 35c) and characterized by AES. The SEM micrograph shows that the nanowire remains intact, whereas partial recrystallization of metal contacts has occurred. Furthermore, AES confirmed that there is no metal (i.e. conductive) layer on either the nanowire or the substrate – no metal out-diffusion from metal contacts was observed. Based on this evidence, we may conclude that due to resistive heating during the I–V measurements, the metal contacts and/or the metal–nanowire interface underwent a transformation, leading to lower contact resistance. (Note the current of 10 μA passing through for several seconds, combined with high initial resistance.) Hence, the initial measurement (blue in Fig. 35b) does not carry any information about the nanowire itself, but rather about the metal contacts and the interface between contacts and the nanowire. This emphasizes the crucial importance of preparing low-resistance Ohmic contacts. Via this "thermal conditioning", the contact resistance was decreased by four orders of magnitude. In principle, the same effect could be achieved by sample annealing prior to I–V characterization.

To assess whether the effect is permanent, another round of I–V measurements was performed (see Fig. 35d) – labelled "II - start" for the first measurement of this cycle and "II - end" for the last. For ease of comparison, the previous measurements (labelled "I - start" and "I - end") are also included. The new measurements are comparable with the "I - end" I–V curve, showing that the change is permanent (hence it is not a temporary temperature effect). Note however that the new curves are smoother and less noisy, and with better repeatability. (This could also be an effect of 200 °C annealing for 24 hours during the AES characterization. However, no change in morphology was observed in SEM after this period.) During this cycle of I–V measurements, the maximum current reached was 16 μA. Still, the measurements "II - start" and "II - end" are comparable, with no significant difference or permanent change. This may indicate that the contact-resistance transformation due to resistive heating had been completed.
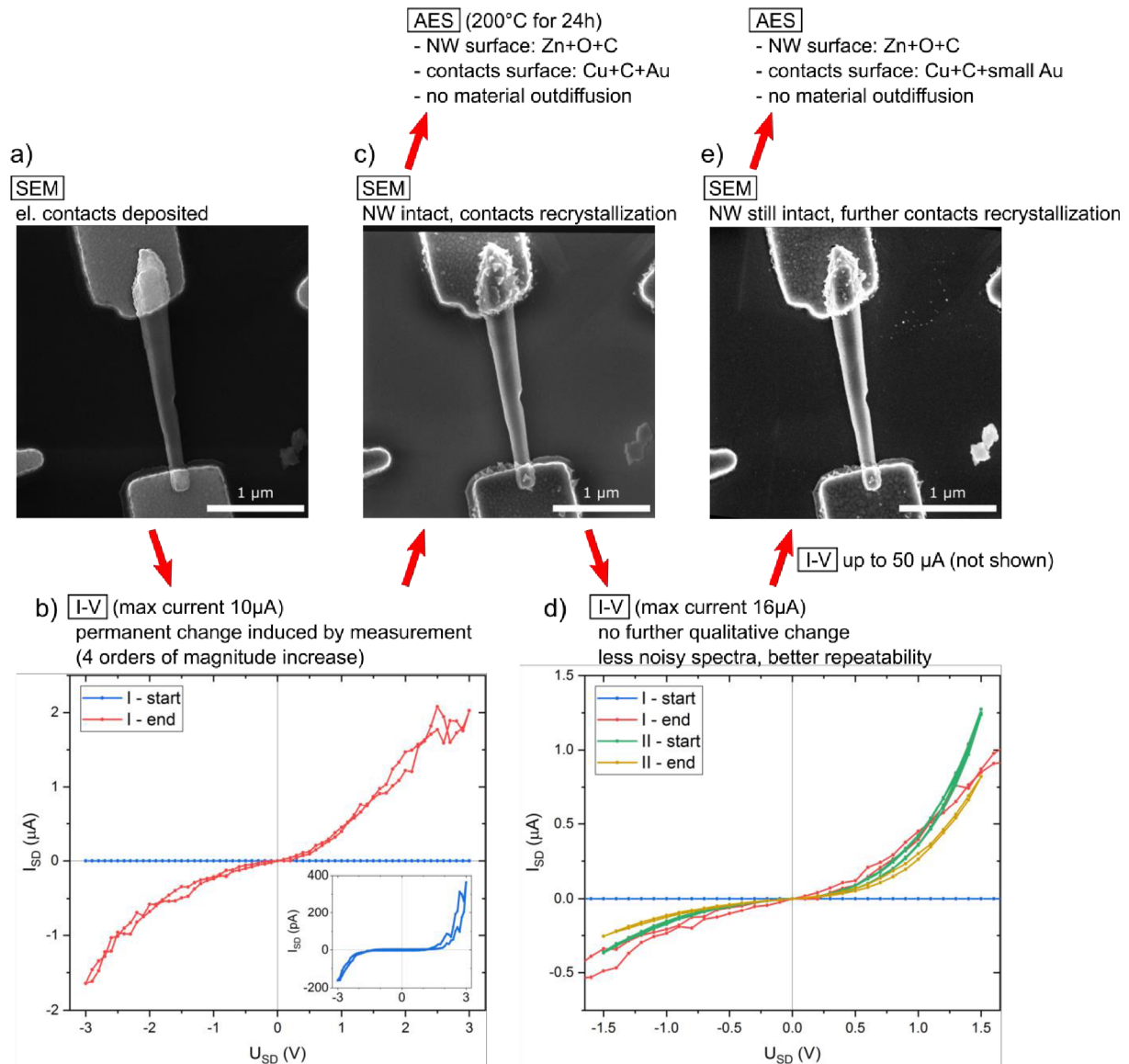
Fig. 35: I–V characterization of an as-grown rod-like ZnO nanowire labelled B – experiment overview. a) SEM micrograph of the nanowire after metal contacts deposition (i.e. prior to any I–V measurements). b) I–V curve measurement of the nanowire shown in (a) – the very first measurement is in blue (see the magnified inset), the last of the series is in red. c) Subsequent SEM micrograph showing metallic contacts recrystallization. A summary of the AES results is included. d) Additional series of I–V measurements of the same nanowire – the first and the last measurement is shown. e) SEM micrograph taken after yet another round of I–V characterization, for source–drain current having reached up to 50 µA. EBL and transport measurements: D. Citterberg. Data analysis: author of the thesis.

Further experiments included I–V measurements with extended limits, reaching up to 50 µA of source–drain current (not shown here). Surprisingly, the nanowire endured intact, see the SEM micrograph in Fig. 35e. Further morphological changes (partial decomposition) of crystallites on metal contacts are clearly seen. Subsequent AES characterization confirmed that there is no metallic layer on either the nanowire or the substrate. More interestingly, the spectra taken from the metal contacts' surface showed very weak Au peaks compared to Cu peaks. Note that the top layer of metal contacts shall be 20 nm of pure Au; the 240 nm Cu layer shall lie beneath. (A similar result – only not so pronounced – has been observed already for the sample shown in Fig. 35c.) Given the high currents during the I–V measurements and contacts recrystallization visible in the SEM micrographs, there must have been a lot of heat produced and dissipated. Taking into consideration the Au–Cu binary phase diagram (see Fig. 36), it is obvious that alloying of gold and copper has

occurred: (i) The phase transformation is possible; different ordering of solid solution occurs below 410 °C, giving rise to Au$_3$Cu, AuCu and AuCu$_3$ phases. (ii) The temperature needed for such transformation has been most likely reached by resistive heating during I–V characterization (note the 4-orders-of-magnitude change in resistivity discussed above). (iii) AES results show that gold leaves the surface of metal contacts in favour of copper. Based on the volume ratio of Au:Cu of 20:240 (=1:12) in the metal contacts, probably a mixture of AuCu$_3$ phase and pure Cu is formed.
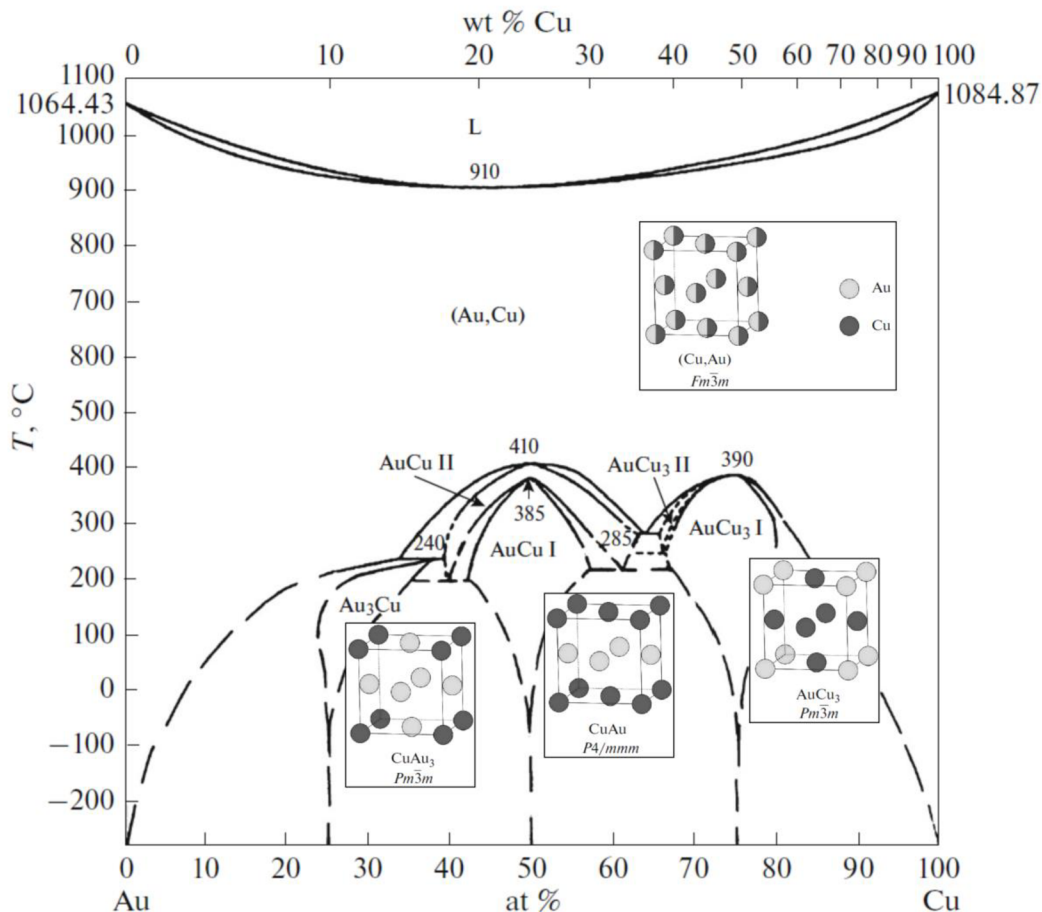
Fig. 36: Au–Cu binary phase diagram. Adapted from [102].

To summarize this section: As these were just the initial measurements of the ZnO nanowires, one may conclude that the I–V characterization of individual ZnO nanowires has been successful with the instrumentation available. However, optimization of metallic contacts is needed. Thicker electrical contacts shall be used to ensure a better nanowire–contact interface. Regarding the electrodes material, the Ti/Au metallization scheme shall be used to ensure the Ohmic behaviour [113; 119]. Further, electrical contacts' tempering (or thermal conditioning) may be needed. As the single-nanowire measurement and data interpretation is a challenging task, a systematic and more complex study shall be performed in the future in order to tailor the process and obtain reasonable results. Regrettably, this has not been possible within the scope of this thesis. That's also the reason why the transport measurements of the diffusionally-doped nanowires (discussed below in section 3.4) were not performed. Instead, the dopant incorporation was assessed directly based on STEM EDS characterization of cross-sectional lamellas cut from the nanowires.

XPS – Annealing in an oxidative environment

As discussed in section 3.1, the presence of oxygen vacancies in ZnO can influence its properties, including dopant incorporation. Furthermore, the concentration of intrinsic defects is growth-method dependent. For both reasons, it is important to characterize the nanowires utilized within this research. The amount of oxygen vacancies can be deduced from XPS measurements. A typical XPS survey spectrum of the sample with the ZnO nanowire ensemble is shown in Fig. 37. Note that the Cl peaks are remnants of the $ZnCl_2$ compound used in the growth process; for growth details see section 3.2. Note also that Cl signal remains present in the STEM EDS spectra of nanowire lamellas even upon the whole Ga-doping procedure described below in section 3.4.2 (including pre-annealing in either vacuum (400 °C, 30 min) or H_2O_2 gas (535 °C, 30 min) and final annealing step at 480 °C for 75 min in vacuum).
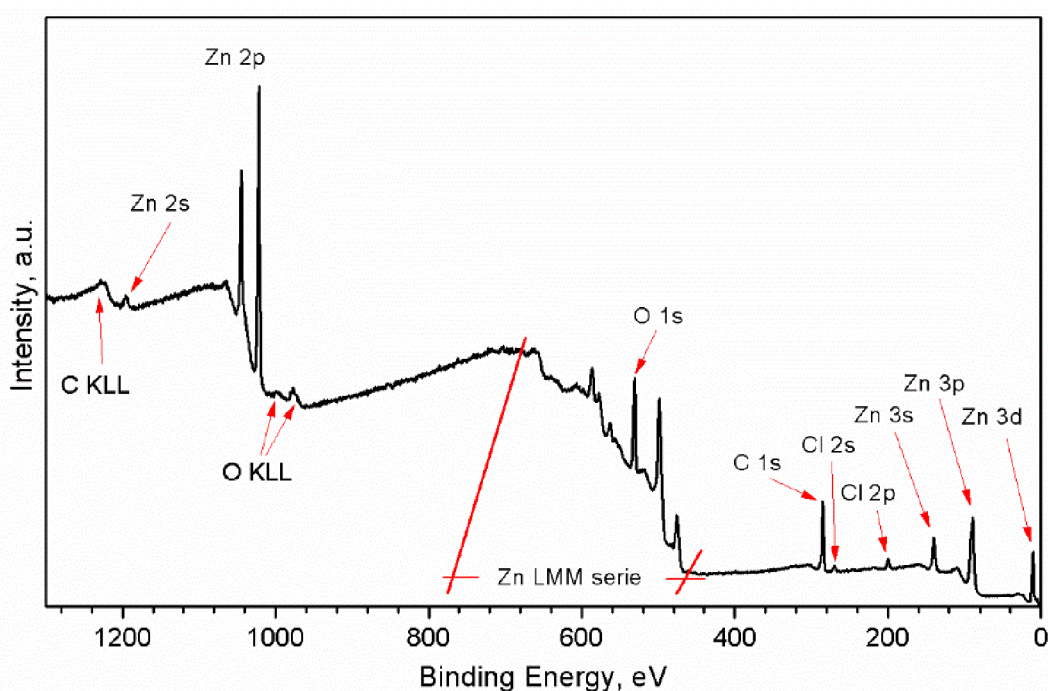
Fig. 37: Survey XPS spectrum of as-grown ZnO nanorods. Image courtesy: S. Vallejos (Figure S3 in the Supporting information of [140]).

In order to assess the relative concentration of oxygen vacancies in the nanowires, the XPS spectra of several samples were acquired for comparison: the as-grown ZnO nanowires and samples annealed in high vacuum and various gases at different temperatures. The upcoming doping-experiment design was taken into account (with respect to annealing temperatures and ambient gas selection). The XPS spectra of O 1s peak of these samples are presented in Fig. 38 (note that the XPS spectra have not been manipulated with respect to energy scale). Clearly, the peak is comprised of several components, being in line with the literature research summarized in section 3.1. Considering the as-grown sample (i.e. *not* annealed, black spectrum), the bulk-ZnO component (centred around 531.0 eV) and the surface-adsorbates peak (532.65 eV) are visible directly. Other samples were annealed in various ambient gases at 400 °C or 535 °C. Upon annealing, the relative intensity of the high-energy component decreased for all samples, showing that this component is indeed related to adsorbates and surface contamination of ZnO. A noteworthy feature (highlighted in the inset with a red arrow) is the "elbow" in the spectra of H_2O_2-annealed samples (red) at around 532.2 eV. Comparing it with the vacuum-annealed sample (green), the two spectra (being otherwise identical)

differ significantly in this particular region (see the inset). This is indeed a sign of the intermediate component of the O 1s peak as reported in the literature – the one related to oxygen vacancies. Thus, Fig. 38 shows that annealing of ZnO nanowires in high vacuum (400 °C) and H_2O_2 gas (400 °C and 535 °C) results in different concentration of oxygen vacancies in the ZnO material. Note that the spectra of the samples annealed in H_2O_2 at 400 °C and 535 °C are identical. Based on Fig. 38, the lowest amount of oxygen vacancies was achieved by annealing in hydrogen peroxide. (Further analysis including O 1s peak deconvolution is discussed below.)

This finding may play a role in the dopant-incorporation experiments presented below in section 3.4. For these experiments, the H_2O_2 oxidative agent has been chosen, given (i) the lowest V_O concentration observed, (ii) its higher reactivity than molecular oxygen and (iii) the fact that it does not require a plasma source or a cracker to produce reactive oxygen species [103].

Regarding the morphology of the nanowires after annealing, no changes were observed in SEM up to the temperature 535 °C for any gas ambient or vacuum. At higher temperatures (600 °C and above), decomposition of the top facet and roughening of the nanowire sidewalls occur, being more pronounced for vacuum-annealed samples (not shown here).
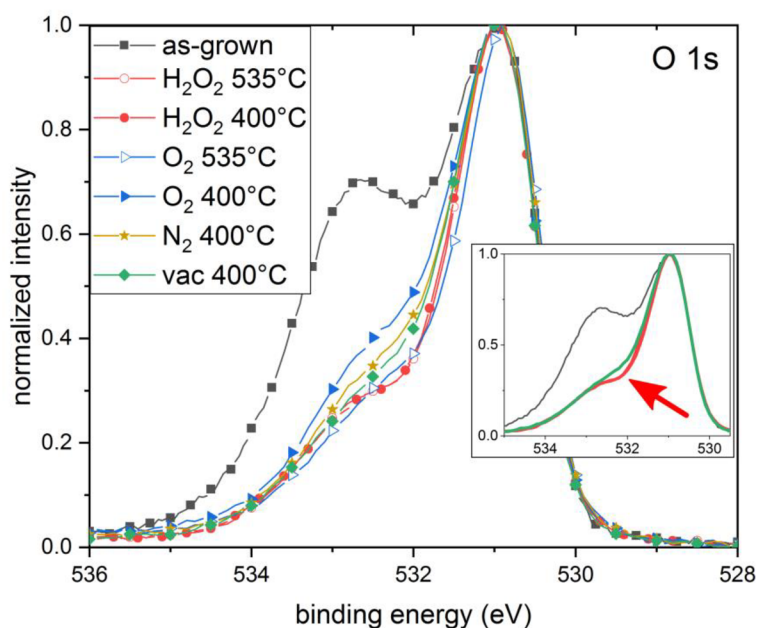
Fig. 38: Detailed XPS spectra of O 1s peak for samples after different post-growth treatment. In the inset, the spectra of the as-grown (black), vacuum-annealed (green) and H_2O_2-annealed (red) samples are highlighted for clarity.

For a more precise assessment of individual components of the O 1s peak, its deconvolution is needed. The spectra presented in the inset of Fig. 38 were deconvoluted into three Voigt profiles using Origin software. The background was fitted with a linear function and subtracted, which may be reasonably applied for spectra exhibiting small intensity differences between low energy and high energy sides of the peaks, which is the case here [104]. The results for H_2O_2-annealed, vacuum-annealed and as-grown samples are presented in Fig. 39a,b,c respectively. Note that the fitting parameters were constrained in the following way: (i) Three Voigt components are taken into consideration. (ii) The FWHM of a specific component has to be the same for all samples. (iii) The relative position of the components is kept constant throughout the sample-set.

Based on the model described above, a plausible fit was found for all three samples, see Fig. 39. The peak centre energies and FWHM of individual components are summarized in Table 4.
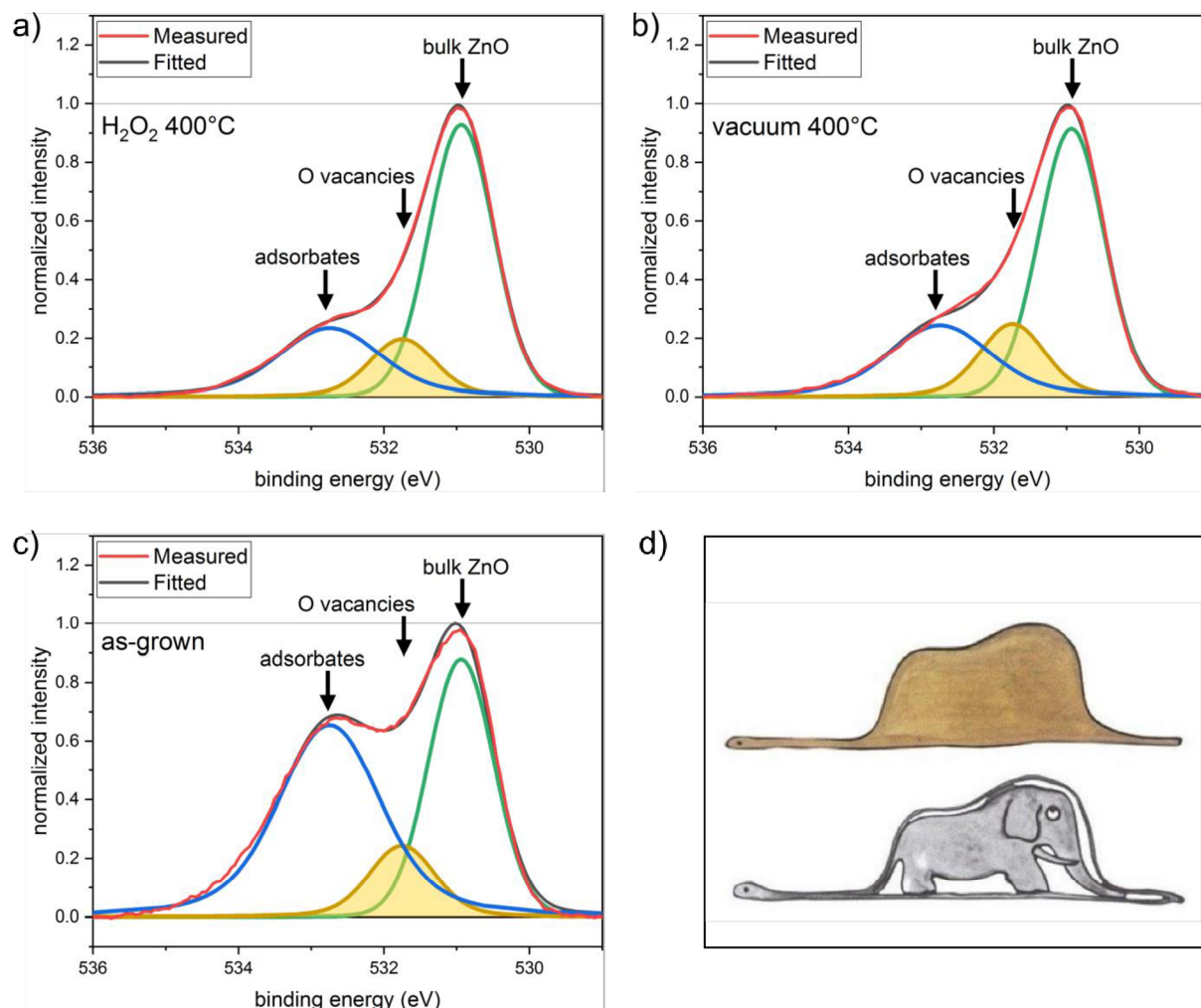
Fig. 39: Normalized XPS O 1s peak spectra of selected samples – deconvolution into individual components: bulk ZnO (green), O vacancies (gold) and surface adsorbates (blue). a) H_2O_2-annealed sample (400 °C). b) Vacuum-annealed sample (400 °C). c) As-grown sample. d) A boa constrictor digesting an elephant. Adopted from [146].

Table 4: Best-fit parameters of XPS O 1s peak components (peak centre, FWHM) as obtained from deconvolution shown in Fig. 39.

sample	adsorbates centre (eV)	adsorbates FWHM (eV)	O-vacancies centre (eV)	O-vacancies FWHM (eV)	ZnO centre (eV)	ZnO FWHM (eV)
H_2O_2-annealed	532.75	1.67	531.75	1.06	530.94	1.06
vacuum-annealed	532.74	1.67	531.74	1.06	530.93	1.06
as-grown	532.75	1.67	531.75	1.06	530.94	1.06

Let's compare the results for the H_2O_2-annealed (Fig. 39a) and vacuum-annealed (Fig. 39b) samples: The adsorbates component (blue curve) is similar for both samples (wrt. the bulk-component). However, the oxygen-vacancy component (gold curve) is indeed undoubtedly higher for the vacuum-annealed sample compared with the H_2O_2-annealed one. See also the summary in Table 5. Both the

peak height and integrated area of O-vacancy component with respect to the bulk component are greater for vacuum annealed sample. This proves that annealing of ZnO nanowires in H_2O_2 atmosphere yields a lower concentration of O vacancies within the material compared to annealing in high-vacuum.

Table 5: Best-fit parameters of O-vacancies component of XPS O 1s peak for selected samples analysed in Fig. 39.

V_O–component	H_2O_2 400 °C	vacuum 400 °C	as-grown
peak height in normalized spectrum	0.20	0.25	0.24
peak height wrt. the bulk-component	21 %	27 %	28 %
integrated area wrt. the bulk-component	23 %	29 %	30 %

Regarding the as-grown sample, the assessment is somewhat more difficult. (May the reader recall a similarly difficult question of what is inside the boa constrictor, to which only the Little Prince knew the right answer – see Fig. 39d. Actually, the Little Prince was doing a deconvolution.) The component related to adsorbates is higher with no doubt. However, the scale of the O-vacancy-component is hard to evaluate, as the deconvolution is *not* unambiguous. The result in Fig. 39c was obtained using the same fitting parameters as for the previous graphs (Fig. 39a,b). Interestingly, the scale of oxygen-vacancy-component in the as-grown sample is similar to the vacuum-annealed one (see Table 5). This may imply that the amount of O vacancies (intrinsically present in as-grown samples) does not change upon annealing in high-vacuum up to 400 °C.

Also, other defects or impurities (such as H or Cl) may be present in small concentrations, having an effect on the XPS spectra of as-grown nanowires. However, note that in the study of gallium incorporation into the nanowires (presented below in section 3.4), the nanowires are always annealed during the doping procedure – either in vacuum or in H_2O_2 gas. Therefore, the XPS spectra of the annealed nanowires presented above are considered a solid reference regarding the relative amount of oxygen vacancies present in the nanowires.

3.4   Diffusional doping – gallium

Gallium doping of ZnO material allows to reach very high doping levels up to several at.%, thus being very promising materials for near-IR to mid-IR plasmonics – see the review in section 3.1. The preparation of such highly-doped ZnO nanowires is one of the thesis' objectives. Thus, the following chapter describes the study of diffusional doping of ZnO nanowires with gallium. The samples – an ensemble of vertical ZnO nanowires grown on Si substrate – were covered with gallium overlayer and annealed in high vacuum or oxidizing environment with the aim of promoting gallium diffusion into ZnO nanowires.

In section 3.4.1, sample treatment and the doping procedure are described. The results of SEM imaging and Raman characterization of samples after different steps of the doping procedure are presented. Then, the results of XPS spectroscopy of Ga-doped nanowire ensemble and HRTEM characterization of individual Ga-treated nanowire are shown. Following the results obtained, an optimized doping procedure is defined and implemented within section 3.4.2. The doping experiment is recorded step-by-step and the real-time in-situ SEM/AES results are presented. Further, the STEM EDS characterization of cross-sectional lamellas cut from the doped nanowires is addressed. Based on a diffusion model described, the diffusion coefficient of gallium in ZnO is derived and compared for two distinct samples of different oxygen-vacancy concentration (pre-

annealed either in vacuum or in H_2O_2 environment). Then, room-temperature PL spectra of these samples are presented.

3.4.1 Procedure details & Basic results

For primary experiments, a dedicated vacuum chamber is used. The samples are annealed by a resistive heater, calibrated with a thermocouple. A commercial Ga effusion cell is used, calibrated with a QCM thin film monitor. The supply of hydrogen peroxide gas is realized by connecting a vessel filled with liquid H_2O_2 to the vacuum chamber with a needle valve. In order to sustain the pressure (3 kPa or 6 kPa) of H_2O_2 in the chamber during selected experiments, the roughing pump was equipped with a butterfly valve; the turbo-molecular pump was switched off.

The experimental procedure consists of several steps:

- pre-annealing:

  Either *none*, or in *high vacuum*, or in *H_2O_2* gas.

  Pre-annealing experiments are more described in section 3.3. Annealing of ZnO nanowires in different environments leads to changes in intrinsic defects concentration, which may have an impact on the (subsequent) dopant incorporation. Namely, the relation between the presence of oxygen vacancies (different concentration of which is created by pre-annealing in vacuum or H_2O_2 gas) and gallium incorporation into ZnO nanowires is studied further.

- gallium deposition:

  Gallium atoms are deposited by evaporation in high vacuum conditions onto the sample kept at room temperature.

- annealing:

  Parameters controlled: *pressure* (high vacuum), sample *temperature*, annealing *time*.

  Given that Ga diffusion is a thermally driven process, the samples are annealed at high temperature to promote Ga diffusion and incorporation into nanowire lattice. However, the thermal decomposition of ZnO nanowires takes place above 600 °C under vacuum conditions. Therefore, the annealing temperature of 535 °C is chosen to be used in this section.

- ex-situ characterization:

  all samples: SEM

  selected samples: Raman spectroscopy, XPS, TEM, AES, STEM EDS, PL

Morphology evaluation

Sample morphology at different stages of the experimental procedure is shown in Fig. 40 in order to illustrate selected steps of the procedure (imaged with ex-situ SEM). All the micrographs were taken from the top-view direction. Further information is inscribed in the micrographs if considered helpful for the reader.

For the experiments, samples with rod-like ZnO morphology are used; see the as-grown nanowires in Fig. 40a. For some of the samples received, the top facets are not entirely smooth, but a faint pattern can be seen in the secondary-electron contrast in the centre of the facet (see Fig. 40a). For other

samples received, the top facets seem to be intact. The sample shown in Fig. 40b underwent the pre-annealing step in H_2O_2 gas (30 min, 535 °C, 3 kPa), followed by vacuum-annealing (30 min, 535 °C, $8 \cdot 10^{-4}$ Pa). Note that after such heat treatment, nanowire morphology does not change and the facets remain smooth.
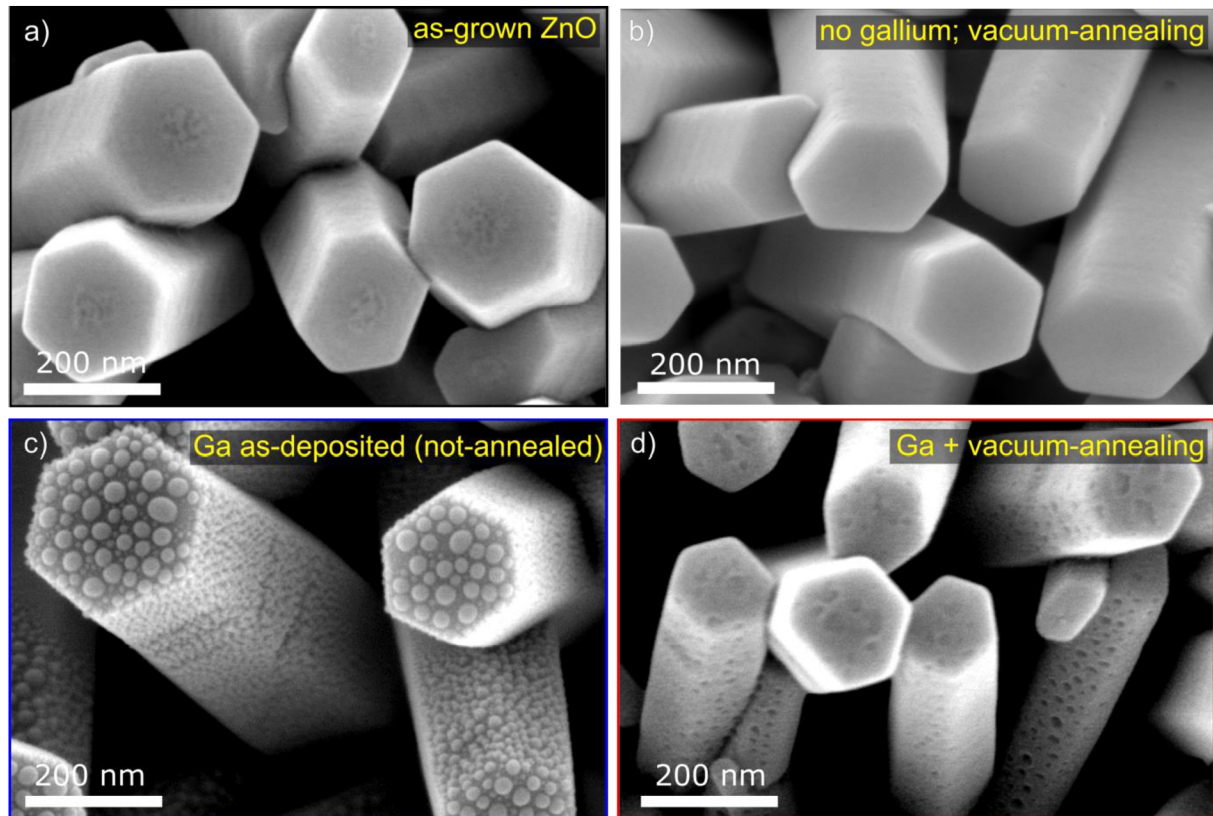

Fig. 40: Impact of annealing conditions on the ZnO nanowire morphology. a) As-grown nanowires. b) Nanowires after pre-annealing in H_2O_2 gas and subsequent annealing step in vacuum (i.e. without Ga deposition). c) Nanowires after evaporation of 12 nm of gallium at room temperature. No post-annealing applied. d) The nanowires after 12 nm Ga deposition and subsequent annealing in high vacuum. Samples a,c,d are taken from *Batch-3*, sample b is from *Batch-2*.

The samples shown in Fig. 40c,d underwent the pre-annealing step in H_2O_2 as well (30 min, 535 °C, 3 kPa). After cooling the samples down to room temperature and reaching high vacuum in the chamber (10^{-4} Pa), 12 nm of Ga was deposited onto both samples. For illustrative purposes, the sample from Fig. 40c was taken out of the apparatus right after Ga deposition. Although the deposition was performed at room temperature, gallium does not form a continuous layer. Instead, individual Ga droplets are formed on the nanowire, leaving part of the ZnO facets exposed. As soon as the sample is taken out of the apparatus for SEM imaging, gallium droplets oxidize. The size of the droplets differs for individual facets, depending on their angle with respect to the Ga beam, which was normal to the sample.

The sample representative of a complete diffusional-doping procedure is shown in Fig. 40d. After pre-annealing in H_2O_2 and Ga over-deposition, it was annealed in vacuum (30 min, 535 °C, $7 \cdot 10^{-4}$ Pa). Gallium droplets are no longer present and the surface of the nanowires is damaged. This indicates that deposited gallium remained in a non-oxidized state and either desorbed or incorporated into the nanowire (or a combination of both). The sidewalls decomposition is induced by the presence of gallium; the nanowires without gallium remained intact after the pre-annealing step in H_2O_2 gas and subsequent vacuum-annealing (535 °C, 30 min) — see Fig. 40b. The nanowires in Fig. 40d are

damaged in a specific way, which is different for the top facet and the sidewalls. On the sidewalls, deeper and more pronounced pits are present, whereas a shallower structure is visible on the top facet. The reason for this difference may be a different structure of the top facet c-plane compared to other crystal planes.

Raman spectroscopy

The samples presented in Fig. 40a,c,d were examined with Raman spectroscopy. The survey spectra are shown in Fig. 41a; a zoomed-in view is presented in Fig. 41b. A reference measurement of a silicon wafer is included. The peaks assignment is inscribed. Let's summarize the main results:

- In Fig. 41c, a variation of E_2(low) peak FWHM is visible. It can be understood as follows: The as-grown sample is in a state with a certain crystal quality and hence FWHM (black spectrum). After pre-annealing in H_2O_2 gas, the crystal structure is improved by decreasing the concentration of oxygen vacancies. Therefore the FWHM gets smaller and subsequent Ga over-deposition does not play a role (blue spectrum). Then, the final annealing step takes place under vacuum conditions, promoting the oxygen-vacancy generation. This leads to FWHM increase again (red spectrum). The same applies to ZnO E_2(high) peak, see Fig. 41d. Note that these results are in line with the PL measurements presented further below (Fig. 59 and Table 9).

- The additional Raman modes (AM) induced by doping as reported in the literature (see section 3.1) are *not* observed after gallium deposition and annealing – see their expected positions highlighted with dash-and-dot vertical lines in Fig. 41b. The AM nomenclature is adopted according to [129]. The additional modes overlapping with Si peaks (at 509 and 623 cm^{-1}) are not shown, as they cannot be utilized for doping evaluation. Still, the most prominent additional mode shall be AM1 at 276 cm^{-1}, which is not observed either. Also, the peak ratio A_1(LO)&AM3 over E_2(high) (being indicative of successful doping [129]) does not follow the desired trend.

- Note that the small peak at about 585 cm^{-1} – assigned to A_1(LO) ZnO mode – has already been visible for the as-grown samples (see Raman characterization in section 3.3). Therefore it is not Ga-related, although it appears more pronounced at the samples with gallium oxide droplets. Likewise, the peak is not related to gallium oxide either: The Ga_2O_3 peaks expected at 200 cm^{-1} (being the highest), 650 and 765 cm^{-1} [133; 147–149] are not visible here, presumably due to the low volume of gallium oxide on the nanowires.

- Small peaks of A_1(TO) and E_1(TO) modes (at 374 and 409 cm^{-1}), which shall be silent for vertically aligned ZnO nanowires, are visible – more for the as-grown samples, see Fig. 41d. Their decrease for processed samples is a temperature-induced effect, as already discussed for the as-grown nanowires – see Fig. 32 in section 3.3.

In general, the strong Raman peaks of Si substrate (300, 520, 623 and 671 cm^{-1}) overlap with ZnO peaks and potential dopant-induced additional modes. This makes the precise interpretation of Raman spectra an intricate task. Therefore, for further potential Raman studies, it would be beneficial to grow ZnO nanowires on a sapphire substrate instead of silicon.
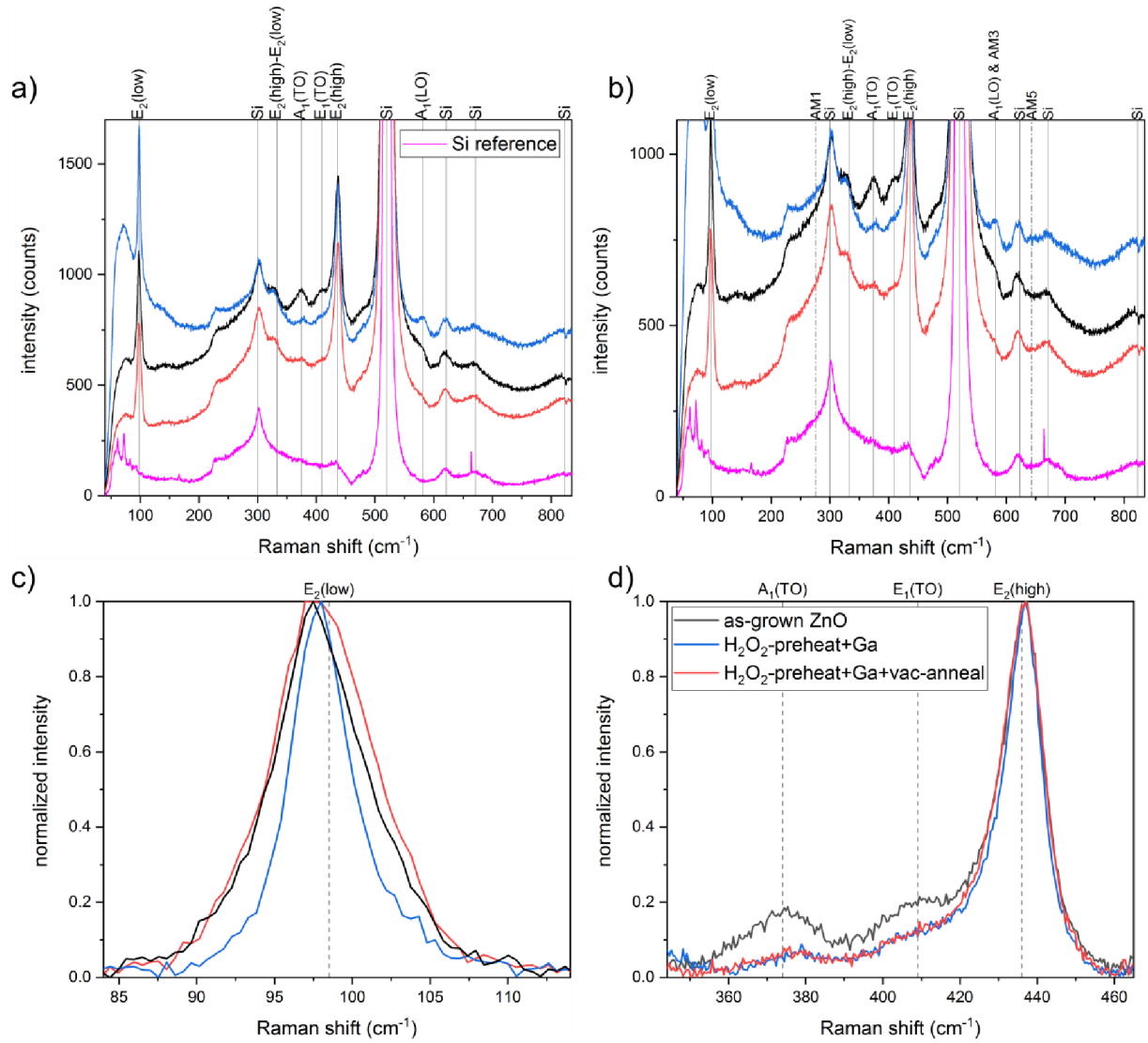
Fig. 41: Raman spectroscopy measurement of the samples shown in Fig. 40a,c,d. The colour-coding corresponds to the frames in Fig. 40. a) Raman survey spectra with peaks assignment. b) Zoomed-in view of the same spectra. The positions of potential additional Raman modes (AM) are depicted with dash-and-dot lines. c,d) Detailed spectra of ZnO E_2(low) and E_2(high) peaks, respectively.

Impact of residual chamber pressure and pre-annealing environment

As an important variable in the experiments, the impact of residual chamber pressure on the final nanowire morphology is addressed hereafter. The residual gas could cause oxidation of deposited gallium before it desorbs or incorporates into ZnO material, thus spoiling the process of diffusional doping. The value of the highest residual pressure during the experiment (from Ga deposition on) is written in the SEM micrographs, see Fig. 42. The samples are taken from *Batch-3*, pre-annealed in H_2O_2 gas (30 min, 535 °C, H_2O_2 at 3 kPa) and over-deposited at room temperature with 12 nm of Ga. Then, they are annealed at 535 °C in vacuum. At the end of the experiment, the nanowires are often covered with oxidized circular remnants of Ga droplets. Notably, the amount of gallium oxide remnants roughly correlates with the residual pressure. Fig. 42 shows the comparison of samples annealed at the same temperature (535 °C) at various residual pressure levels. While at the pressure of $7 \cdot 10^{-4}$ Pa the nanowire facets are partially decomposed and no Ga remnants are visible (Fig. 42a), at the pressure as high as $4 \cdot 10^{-2}$ Pa the nanowire is covered with large oxidized Ga remnants (Fig. 42b). The intermediate state (for both the pressure and the morphology) is depicted in Fig. 42c, using

54

a sample from *Batch-5*. Based on the results discussed so far, it seems that the turning-point for the residual pressure is about $9 \cdot 10^{-4}$ Pa, depending also on the annealing temperature and batch number. Generally, the pressure has to be low enough not to allow gallium oxidation during the experiment timeframe.
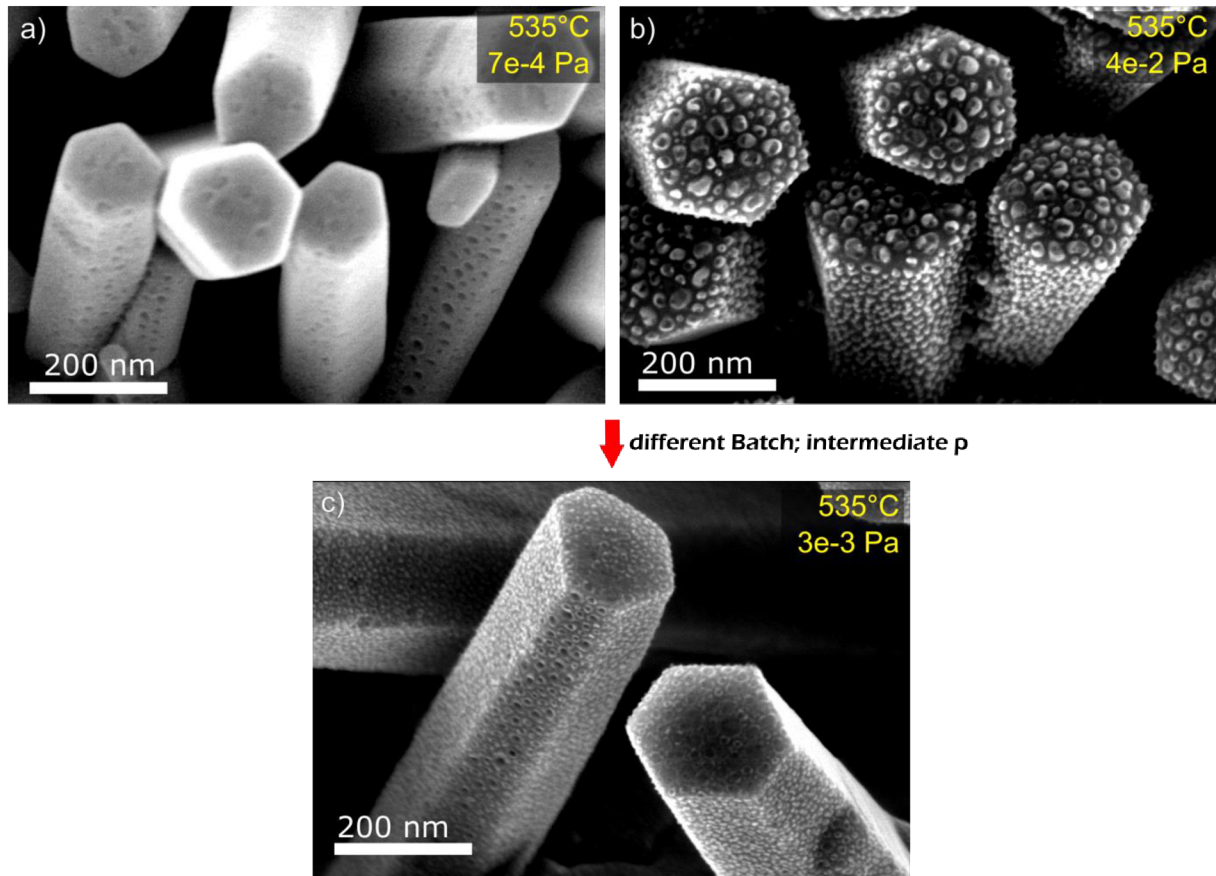
Fig. 42: Impact of residual gas pressure on the final nanowire morphology, given the annealing temperature is the same. Samples a) and b) are from *Batch-3*, sample c) is from *Batch-5*.

The impact of the pre-annealing environment was looked into as well. No influence on final nanowire morphology after Ga diffusion step was found whatsoever. See Fig. 43 comparing the samples pre-annealed for 30 min in high vacuum (400 °C, $2 \cdot 10^{-3}$ Pa) and H_2O_2 gas (535 °C, 3 kPa). After deposition of gallium (12 nm), both samples were annealed in high vacuum at 535 °C for 30 minutes. Morphology of both samples shows similarly damaged nanowires with characteristic pits on the sidewalls.
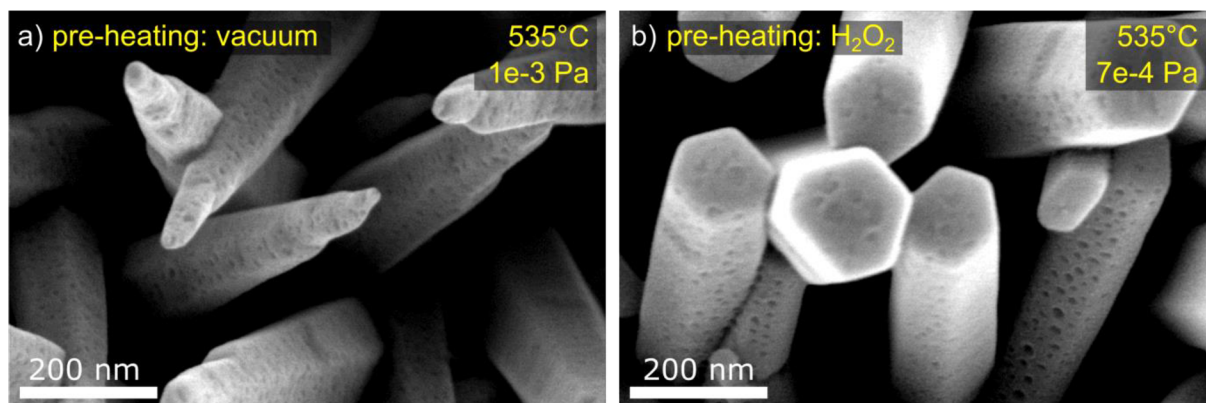
Fig. 43: Samples pre-annealed at high vacuum (a) and H$_2$O$_2$ atmosphere (b). No morphology difference is observed wrt. nanowire damage or Ga remnants.

To summarize the results presented so far: The key parameter that influences the process is residual chamber pressure. If higher than $9 \cdot 10^{-4}$ Pa, it causes the oxidation of gallium on the nanowire surface, preventing Ga incorporation. In the optimized experimental procedure (see section 3.4.2), the base pressure of the vacuum chamber will be improved. Also, Raman spectroscopy proved not to be a suitable technique for doping-level assessment of our samples, as the nanowire ensembles are grown on a silicon substrate. The Raman peaks of silicon overlay the peaks assigned to doped ZnO. Therefore, other techniques will be utilized in further text for assessment of Ga incorporation into the ZnO nanowires – namely in-situ SEM and above all STEM EDS.

XPS measurements – Gallium treated samples

As introduced in sections 3.1 and 3.3, the XPS measurements are able to provide information about the crystalline structure and composition of ZnO nanowires. It is interconnected with the intrinsic point defects concentration and possibly with the incorporation of the extrinsic dopants, having an impact on the O 1s peak components proportion. Namgung et al. [116] studied the drive-in diffusion of aluminium dopant into ZnO nanowires. Indeed, they observed higher O 1s component connected with oxygen vacancies after the doping process; the explanation being that O vacancies were generated by Al doping. Our experiments (designed in a similar way) with gallium deposited onto ZnO nanowires do not show any change in O 1s peak whatsoever for samples measured without annealing (no doping expected) and after annealing in vacuum (doping expected via a drive-in diffusion), see Fig. 44b; despite a major change in morphology (see SEM micrographs in Fig. 44a). Thus, with the mutual ratios of individual components of O 1s peak staying the same for both samples, we do *not* observe similar results to Namgung et al. Therefore, the experimental procedure implemented does not increase the concentration of oxygen vacancies in ZnO nanowires, contrary to Al diffusional doping.
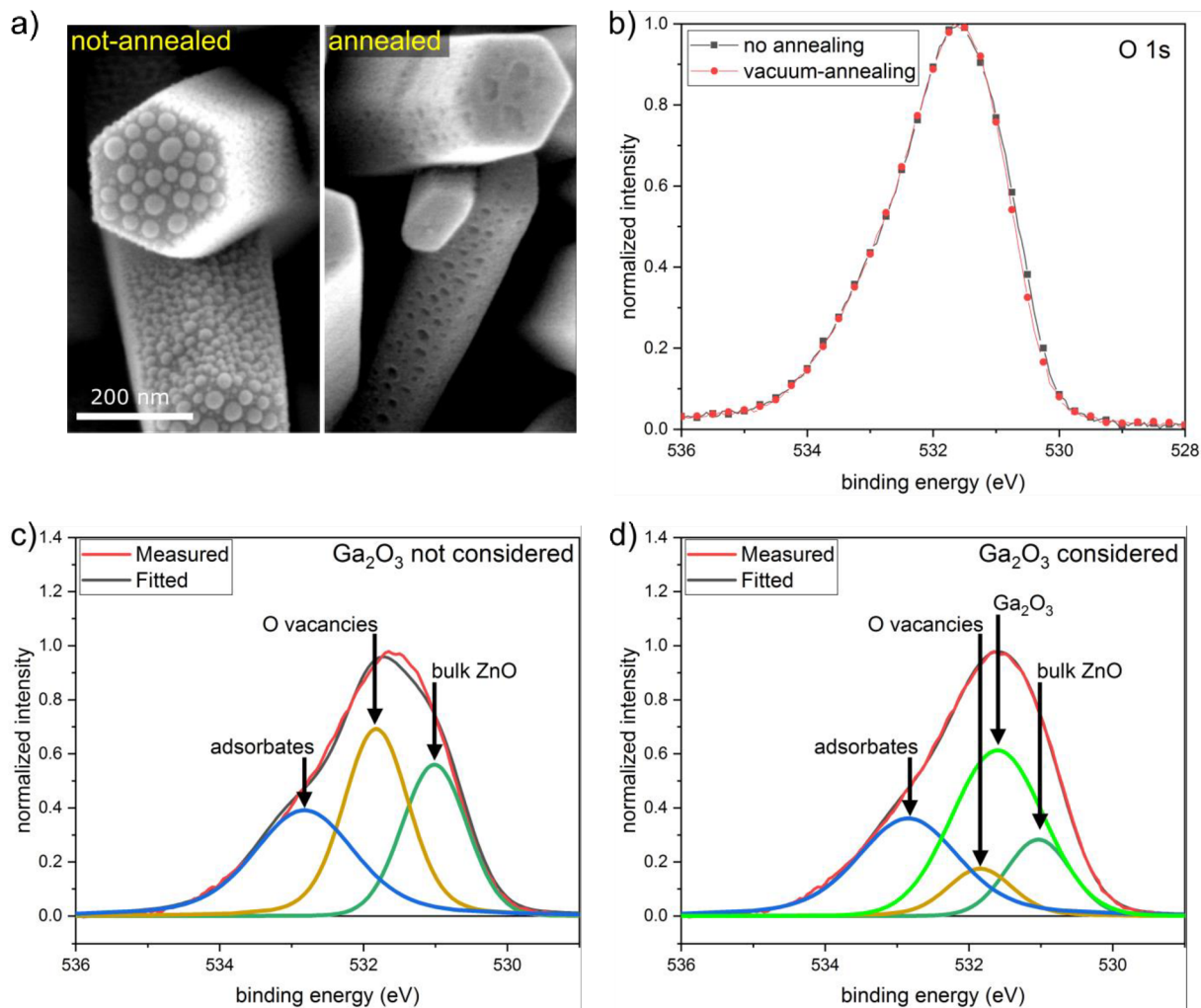
Fig. 44: a) SEM micrographs of ZnO nanowires over-deposited with Ga (at room temperature) and either taken out of the vacuum chamber directly (left, no annealing step) or annealed in vacuum at 535 °C upon Ga deposition and only then taken out (right). **b)** Detailed XPS spectra of O 1s peak of these samples. Interestingly, no difference is observed. **c)** Deconvolution of the O 1s peak based on the same fit-parameters as in section 3.3. The Ga_2O_3-component is *not* considered here, i.e. only the components assigned to surface adsorbates on ZnO (blue), oxygen vacancies (gold) and standard ZnO lattice (dark green) are considered. Note that the cumulative fit deviates from the measured curve, indicating the presence of another component. **d)** Deconvolution of the O 1s peak, taking into account also the Ga_2O_3-component (light green) of O 1s peak.

Let us present the XPS measurements in more detail. The samples (SEM micrographs of which are shown in Fig. 44a) are the same as presented earlier in Fig. 40c (no annealing upon Ga deposition) and Fig. 40d (vacuum-annealed upon Ga deposition). A quick reminder on samples' preparation: Both underwent the pre-annealing step (30 min, 535 °C, H_2O_2 at 3 kPa). After cooling the samples down to room temperature and pumping down to high vacuum (10^{-4} Pa), 12 nm of Ga was deposited onto the samples. The "not-annealed" sample was taken out of the apparatus right after Ga deposition. The "annealed" sample was annealed right after Ga deposition without breaking vacuum conditions (annealing: 30 min, 535 °C, $7 \cdot 10^{-4}$ Pa). The latter sample represents an ideal candidate for doped nanowires – it has undergone the whole procedure and there are no Ga_2O_3 remnants visible in SEM on the surface. The other sample represents a good reference, as the only difference is the absence of the final annealing step.

Surprisingly, the XPS spectra of O 1s peak of those two samples (Fig. 44b) evince no difference whatsoever, even despite a profound change in morphology. The peak in Fig. 44b is markedly

asymmetric; its deconvolution into individual components is to be performed and discussed hereafter. Note that this deconvolution applies for both spectra from Fig. 44b as they are practically identical. First, in Fig. 44c, a deconvolution based on the same fit-parameters as for the as-grown ZnO nanowires (see Table 4 in section 3.3) is presented. Three components are considered – ZnO lattice (dark green), oxygen vacancies in ZnO (gold) and surface adsorbates (blue). As clearly seen, the fitted curve (black) deviates from the measured one (red) significantly. Moreover, the O-vacancy component is unrealistically high compared to the bulk-ZnO component. It is clear that yet another component has to be added – the one corresponding to Ga_2O_3 (or gallium oxides in general). Such four-component deconvolution is presented in Fig. 44d; the best-fit parameters are presented in Table 6. This fit corresponds much better to the measurement and what's more, the ratio of individual components seems physically plausible. Note that the relative positions of the individual components of the O 1s peak of ZnO (adsorbates, O-vacancies, bulk-ZnO) were kept the same as in section 3.3 as well as their FWHM. The XPS measurements were not calibrated for C 1s peak energy (here centred at 285.6 eV), therefore the spectrum is slightly shifted with respect to the measurements presented there (by 0.1 eV) – based on comparison of Table 4 with Table 6. Taking into account the energy of the C 1s peak, the position of Ga_2O_3-component (here at 531.6 eV) corresponds to the available literature on Ga_2O_3 (531.3 eV in [150; 151]; 531.8 in [152]; 531.1 in [153]).

Table 6: The parameters of the XPS O 1s peak components (bulk ZnO, Ga_2O_3, O vacancies, adsorbates) as obtained from the deconvolution shown in Fig. 44d.

component	centre (eV)	FWHM (eV)
ZnO	531.03	1.06
Ga_2O_3	531.60	1.50
O-vacancies	531.84	1.06
adsorbates	532.84	1.67

Interestingly, given that both morphologies presented in Fig. 44a yield the same XPS spectra, the Ga_2O_3-component stays constant for both samples. Therefore, gallium is still present in the annealed sample in the form of its oxide. However, no Ga_2O_3 droplets are visible in the SEM micrograph after annealing. The XPS spectra of Ga $2p_{3/2}$ and Ga 3d peaks are shown in Fig. 45a,b, respectively. They confirm the presence of gallium oxide on both samples. The only difference in the spectra is the presence of a small peak of elemental Ga in the not-annealed sample – presumably in the core of gallium oxide droplets (where gallium did not get oxidized due to the droplets' size). No elemental-Ga signal is observed for the annealed sample, indicating that all the gallium is in the oxidized state. Probably, gallium forms a thin layer of gallium oxide on the surface. At the same time, however, assuming that gallium *did* diffuse into ZnO lattice and substituted Zn atoms, the Ga–O bonds would form as well, possibly yielding similar XPS results as for gallium oxide(s) on the surface. As will be shown later, STEM EDS confirms both the Ga-rich oxidized surface layer and gallium diffused into the nanowires (see section 3.4.2).
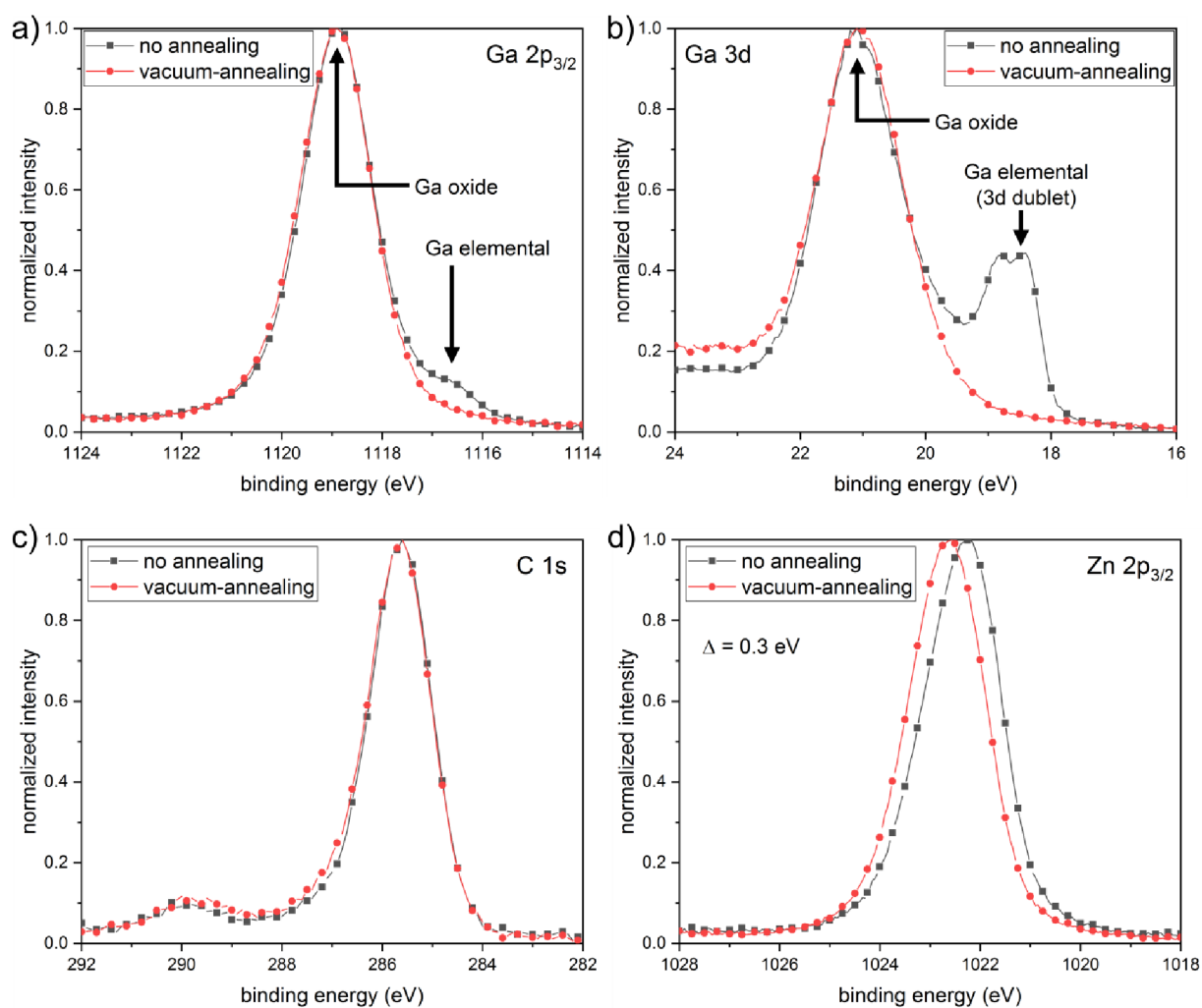
Fig. 45: Detailed XPS spectra of a) Ga 2p$_{3/2}$, b) Ga 3d, c) C 1s and d) Zn 2p$_{3/2}$ peaks of the ZnO nanowires over-deposited with gallium without further annealing (black spectra) and with final annealing step upon Ga deposition (high vacuum, 535 °C, 30 min; red spectra).

For the sake of completeness, the C 1s and Zn 2p$_{3/2}$ peaks are presented in Fig. 45c,d, respectively. The carbon spectra are identical (with C 1s peak centre at 285.6 eV; no shift observed). Interestingly, the Zn 2p$_{3/2}$ peak centre is shifted by 0.3 eV towards higher binding energy for the annealed sample. The FWHM of the peak remains identical for both samples (1.8 eV). Note that the same shift was observed for the Zn 3p peak (not shown here). Surprisingly, no shift and no change in the shape of Ga 2p$_{3/2}$ peak is observed (as should have been the case for Ga3+ ions substituting Zn2+ ions in ZnO lattice, as reported in [138; 154; 155]).

A follow-up discussion is presented below, where TEM characterization of this particular annealed sample is shown and discussed.

HRTEM characterization – Gallium-treated nanowire

The aim of this part is to compare the results of the TEM characterization of an as-grown nanowire (see section 3.3) and a gallium-treated nanowire. The latter nanowire is taken from the sample shown in Fig. 40d, which underwent the following Ga-treatment procedure (selected as a result of optimization discussed in previous sections): H$_2$O$_2$ pre-annealing step (30 min, 535 °C, H$_2$O$_2$ at 3 kPa), Ga deposition (12 nm, 10^{-4} Pa), annealing step (30 min, 535 °C, 7·10^{-4} Pa). It is also the same sample

as shown in Fig. 44a on the right (the "annealed" sample, SEM micrograph) and characterized by XPS, see Fig. 44 and Fig. 45. XPS measurements confirmed the presence of gallium bound to oxygen. The SEM micrographs show pits in the nanowire sidewalls and no visible Ga droplets (see Fig. 46a). The TEM characterization may provide a decisive insight to answer the question, whether gallium forms an oxidized layer on the nanowire surface, or diffuses into the nanowire, substituting zinc atoms in ZnO lattice.

The goals of the TEM characterization are following:

- To assess whether the crystal structure of the nanowires changes after gallium treatment
- Decide whether gallium is localized on the nanowire surface or diffuses into the ZnO lattice
- As the nanowire top facet is of different crystallographic orientation and polarity than the sidewalls (see section 3.2), the process of Ga diffusion may differ for these two surfaces. Therefore, they shall be analysed separately with respect to Ga diffusion into the nanowire.

For TEM characterization, the sample was prepared in the same way as the as-grown nanowire discussed in section 3.3. Two conclusions are drawn based on the EDS inspection of the wire (images not shown here): (i) The presence of Cl was detected. This is not surprising, considering the $ZnCl_2$ agent used for nanowire growth (see section 3.2 for growth method description). (ii) Gallium peaks are visible in the spectra taken from different parts of the nanowire. The ratio of Ga:Zn signal increases towards the edges of the nanowire. This indicates the presence of gallium on/near the nanowire surface. This is in line with the XPS measurements of this particular sample (showing Ga–O bonds, Fig. 44 and Fig. 45). Apart from these findings, no other local differences are apparent in the EDS data for this configuration (i.e. nanowire lying flat on the membrane). For more precise analysis, a cross-sectional EDS study is recommended for future samples. (See conclusive results in section 3.4.2, showing such analysis of different Ga-treated ZnO nanowires.)

The HRTEM analysis of the sample is shown in Fig. 46. Firstly, *no* gallium oxide layer was observed on the nanowire surface at all. This indicates that gallium incorporates into ZnO material rather than forming a thin layer of gallium oxide on the surface. Furthermore, the values of the lattice constant *c* are identical near the surface and in the volume of the nanowire (see Fig. 46c). Also, the crystal planes reach up to the nanowire surface. Thus, the crystalline quality of ZnO is preserved after Ga incorporation. Secondly, a clear zig-zag change in contrast near the wire surface is observed (see Fig. 46b in between the black arrows as a guide to the eye). This can be explained by the different thickness of the sample in this area due to the sharp edges of the etched-away pits on the nanowire sidewalls (compare with the SEM micrograph in Fig. 46a). So, this change in TEM contrast follows the surface morphology of the nanowire. Thirdly, no difference between the nanowire sidewalls (non-polar $\{10\bar{1}0\}$ facets) and the top facet (polar (0001) orientation) was observed.
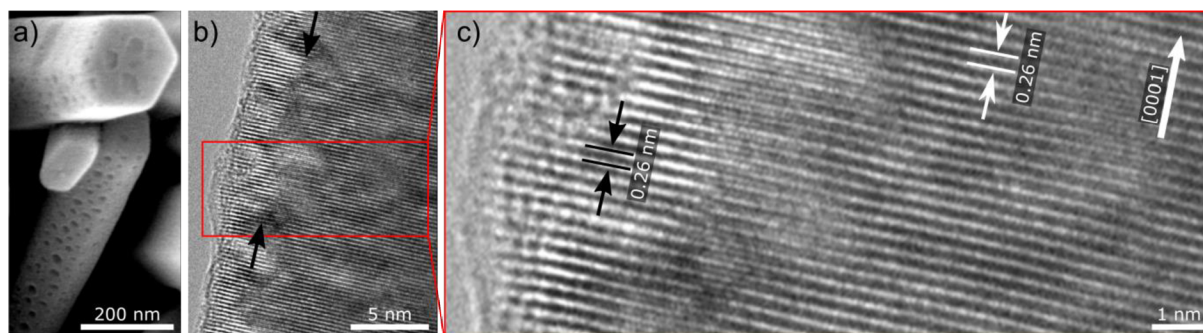
Fig. 46: a) Top-view SEM micrograph of the gallium-treated ZnO nanowire. Another NW from the same sample was further analysed by TEM. **b)** TEM image of the sidewall of the nanowire. The crystal planes are visible all the way up to the NW surface. Note the sharp change in contrast – the black arrows serve as a guide to the eye. **c)** HRTEM image of the same nanowire. Imaging: K. Bukvišová. Image analysis: author of the thesis.

3.4.2 Optimized procedure

Let's summarize the key conclusions from previous chapters. Firstly, ZnO nanowires of needle-like and rod-like morphology shall be assessed separately, as they show differences in Raman spectra for the as-grown samples already. For the same reason, the samples from a single growth-batch shall be used for any comparative study. Secondly, the concentration of oxygen vacancies within ZnO nanowires can be altered by annealing in vacuum or H_2O_2 gas and measured with XPS. Thirdly, the residual pressure in the vacuum chamber is one of the limiting factors for the gallium-doping experiment. The pressure in the order of 10^{-3} Pa is not sufficiently low; it causes the oxidation of gallium, which inhibits gallium incorporation into the nanowires. Finally, gallium-induced decomposition of ZnO wires is observed at elevated annealing temperatures (desired for promoting Ga diffusion into ZnO). This leads to the formation of etched-away pits on nanowires' facets. The presence of gallium in such structures is confirmed by XPS and STEM EDS.

Based on the findings summarized above, the experiment was transferred into another apparatus, which provides lower residual pressure (UHV conditions, base pressure down to 10^{-9} Pa) and the possibility of in-situ SEM/AES characterization during sample annealing. The aim is to prevent the oxidation of gallium deposited onto ZnO nanowires during the experiment and to inspect the process of diffusional doping in-situ in real time, using combined SEM and AES techniques. Further, prospective gallium incorporation into ZnO nanowires will be characterized directly with STEM EDS, using cross-sectional lamellas cut from the nanowires. The points to be targeted are namely:

- Suppression of gallium oxidation due to better residual pressure – in order to neglect the effect of this variable on diffusional doping process evaluation.
- A better understanding of ZnO nanowires degradation during the process (formation of pits on nanowire sidewalls). Distinguishing between thermal decomposition and Ga-induced process.
- Determining the spatial distribution of gallium on/within the nanowire after the annealing step.

In further chapters, two distinct samples from the same *Growth-batch-1* will be inspected and compared. (For the summary of sample batches, see Table 1 in section 3.3.) The two samples will differ in the pre-annealing environment (vacuum or H_2O_2 gas) so that the relation between oxygen-vacancy concentration and Ga incorporation can be assessed. The samples are labelled "V_O-rich" for the sample with a large concentration of O vacancies (caused by pre-annealing in vacuum; see the

reasoning and XPS results in chapter 3.3) and "V_O-poor" for the sample with a low concentration of O vacancies (caused by pre-annealing in H_2O_2 gas).

Real-time in-situ SEM/AES

For the in-situ SEM/AES experiment, the V_O-rich sample is used. Its preparation was following: It was pre-annealed in vacuum (300 °C, $4 \cdot 10^{-6}$ Pa) for 30 minutes. After cooling down to room temperature, 9 nm of Ga was deposited onto the sample (Ga flux direction was 30° to the sample surface; chamber pressure $4 \cdot 10^{-6}$ Pa). Then the sample was transferred in-situ to the AES chamber with a base pressure of $7 \cdot 10^{-9}$ Pa. Due to the ZnO NWs growth process (see section 3.2), there is a high density of thin nanowires in the centre of the sample, whereas a low density of thicker wires is found on the sample edges. For better illustration and visibility, such isolated thick wires were chosen for the in-situ study. These wires are fully representative (and in line with the previously studied ones) as they are bounded by the same crystallographic facets. Furthermore, as gallium flux is oriented 30° to the sample surface, only one side of the nanowire is decorated with gallium. This gives us the possibility to study both Ga-decorated and bare-ZnO facets at the same time under the same conditions.

The gallium–doping experiment flowchart is presented in Fig. 47. Two adjacent nanowires decorated with gallium were selected to undergo the in-situ annealing with real-time SEM imaging. Note that due to shadowing of the incident Ga flux, there are both Ga-decorated and non-deposited areas on the top facet of the right-hand-side wire (well seen in Fig. 47a). The sample was annealed gradually so that the dynamics of morphological changes could be observed in real time; the sample temperature and time-stamp since the beginning of annealing is inscribed in the SEM micrographs. The maximum chamber pressure during annealing was $2 \cdot 10^{-7}$ Pa. After annealing the sample up to 480 °C (which is the maximum allowed temperature in the apparatus), the wires were inspected with the AES technique (still at 480 °C; results discussed below) and cooled down to RT (Fig. 47e).

Let's have a look at the interaction of Ga with the ZnO wires step by step. In Fig. 47a, two ZnO wires upon Ga deposition are imaged at room temperature (prior to the beginning of annealing, t = 0 min). Ga droplets have covered the sidewalls of the left wire and part of the top facet of the right wire – the shadowed area without gallium deposit is clearly seen. Note the sharp borders indicating low Ga surface diffusion at room temperature (indicated by dashed lines in the other micrographs). Next, the sample was heated up to 440 °C (Fig. 47b, t + 77 min). Gallium droplets get gradually smaller, i.e. no Ostwald ripening is seen. Therefore, either Ga desorption or its diffusion into ZnO volume takes place. Also, no damage to the ZnO wire is observed. (Note that the decrease in Ga droplets volume was evident already at 350 °C, t + 48 min; not shown here.) Having increased the temperature to 450 °C (Fig. 47c, t + 95 min), Ga droplets have completely disappeared and smooth ZnO facets are seen. Interestingly, as will be shown later by AES (Fig. 49), gallium undoubtedly remains present on such facets. Therefore, Ga does *not* desorb from ZnO, but rather incorporates into the nanowire. After further temperature increase and time delay (Fig. 47d, 480 °C, t + 180 min), the surface of the wire starts to be decomposed (see the etched-away pits). Notably, this decomposition occurs only on areas of previous Ga deposition – mind the shadowed top-facet area, which remains smooth and intact (marked by the dashed purple lines). Therefore, the observed ZnO decomposition is *not* a temperature effect itself; the ZnO etching is gallium–induced. (This is in agreement with the results presented earlier, where vacuum–annealing of as-grown ZnO nanowires up to 535 °C did *not* induce their thermal decomposition; see Fig. 40b in section 3.4.1.) Figure Fig. 47d shows the sample conditions when the AES measurements presented in Fig. 49 were performed. After that, the sample
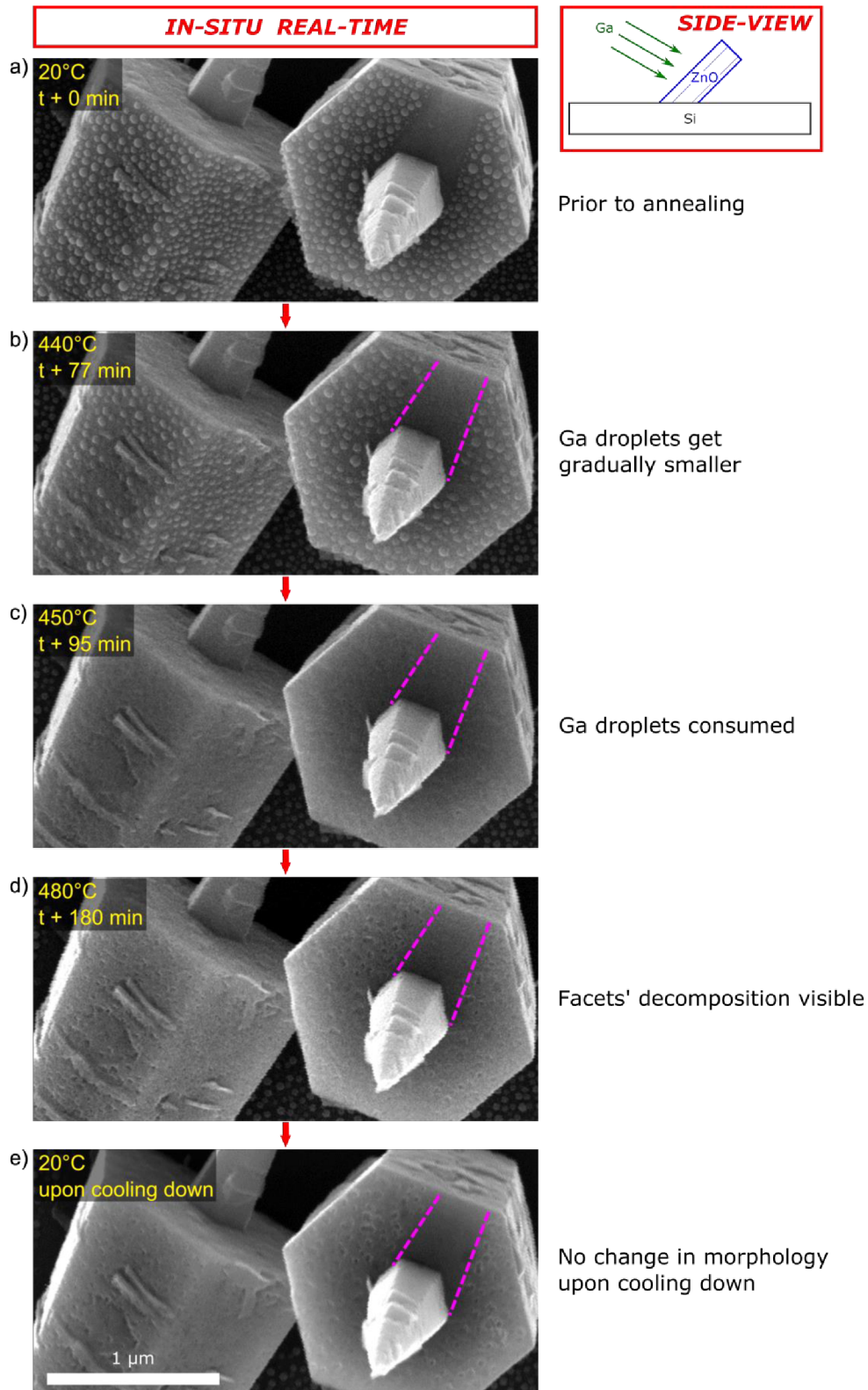
Fig. 47: Flowchart of gallium–incorporation experiment: Real-time in-situ SEM study of Ga incorporation into ZnO wires at elevated temperatures and Ga-induced ZnO decomposition. The timestamp (since the start of annealing) and sample temperature are indicated in each micrograph. After Ga deposition at room temperature (a), the sample is heated up step by step. Ga droplets get gradually smaller (b) until they get completely consumed (c). After that, the wire facets start to decompose (d) – both the sidewalls and the top facet of the wire (despite being crystallographically different). Note that the decomposition takes place only on areas originally decorated with gallium – see the difference for the shadowed area on the top facet, marked by the purple dashed lines. e) Final sample morphology after the annealing sequence and cooling down to room temperature. No gallium precipitation is observed. Note that gallium has not desorbed, but rather incorporated into ZnO (as proved by AES and EDS, see further text).

was cooled down to room temperature (Fig. 47e). The sample preserved the same morphology as at the end of the annealing series (480 °C), including the distinction between the etched and the intact area. Note that *no* gallium droplets have formed on the wire after cooling down – indicating permanent change and real incorporation (as opposed to forming a thin surface layer). Also, *no* gallium–oxide remnants have formed under these conditions, which is in contrast with measurements presented above in section 3.4.1 (performed in the chamber with much worse base pressure; see Fig. 42b,c). The oxidized remnants of deposited gallium were indeed a parasitic effect of the residual chamber pressure, oxidizing the surface gallium before the annealing process could be finished.

A reasonable question is whether the behaviour presented in Fig. 47 is influenced (or even caused) by the electron beam itself, utilized for imaging the process. All SEM micrographs presented in this section 3.4.2 were acquired using a 10 keV beam with a probe current 100 pA. No effects of electron beam irradiation were observed. Nevertheless, another ZnO wire from the same sample was briefly imaged during the annealing experiment (only three times in order to minimize the e-beam irradiation) – see Fig. 48. The results are the same as in Fig. 47. Therefore, we may conclude that the electron beam does not affect the observed results under the experimental conditions used.
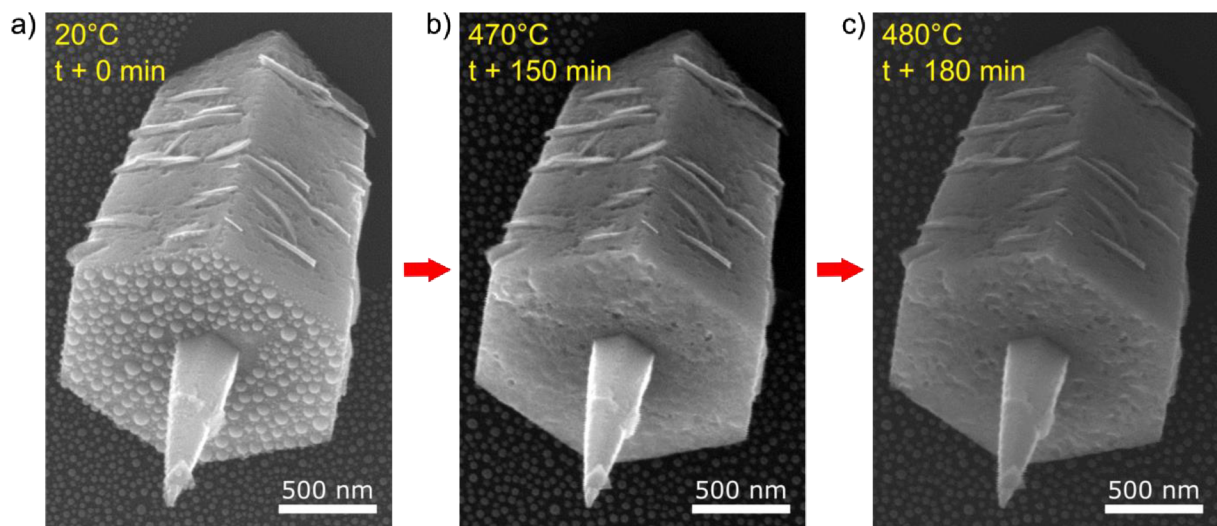

Fig. 48: A check-experiment investigating the influence of e-beam SEM irradiation on the Ga-incorporation into ZnO wires. Compare with Fig. 47. Here, the e-beam irradiation used for imaging the wire was reduced to a necessary minimum (i.e. a single scan for each micrograph shown; 3 scans in total). The wire is part of the same sample as the wires discussed in Fig. 47 and hence it has undergone the same experimental procedure, except the e-beam irradiation for SEM imaging. The resulting morphological features are identical. Therefore, the process of Ga-incorporation into ZnO wires discussed in this chapter is not affected by the e-beam used for SEM imaging (10 keV beam, probe current 100 pA).

The already mentioned AES spectra taken at elevated temperature from both the partially-decomposed (etched) and the intact (shadowed) area of the top facet of the ZnO wire shown in Fig. 47d are presented in Fig. 49a (C and O peaks) and Fig. 49b (Ga and Zn peaks).

Two points are worth noting here:

- In the AES spectral region between 800 eV and 1200 eV, there shall be three zinc peaks and three gallium peaks. The upper indices in Fig. 49b indicate how intense the peaks shall be (e.g. Ga^1 being the highest and Ga^3 the least pronounced). Note that this labelling is applied for the purpose of this thesis only to ease the evaluation and description.

- Given the rougher (i.e. "more 3D") morphology of the etched area, spectra normalization was applied. Here, normalization means the multiplication of measured spectra so that they reach the same background intensity at the upper end of the energy range.

Carbon peak is visible in both spectra due to contamination. More interestingly, gallium is also visible in both spectra. This is not surprising in the area of previous Ga deposition (and incorporation), yet gallium present in the "shadowed" area indicates higher Ga surface diffusion at elevated annealing temperatures than expected from the sharp boundary between the etched and intact parts of the top facet. Still, the Zn^1 peak is more visible in the shadowed area, see Fig. 49b. (Gallium presence after annealing on the facets not originally decorated with gallium is further confirmed by STEM EDS measurements, see further text and figures in this chapter. Lower Zn^1 peak on the etched area – where Ga was deposited – corresponds with EDS results as well; smaller Zn concentration was observed where Ga had been deposited, see e.g. Fig. 52.)
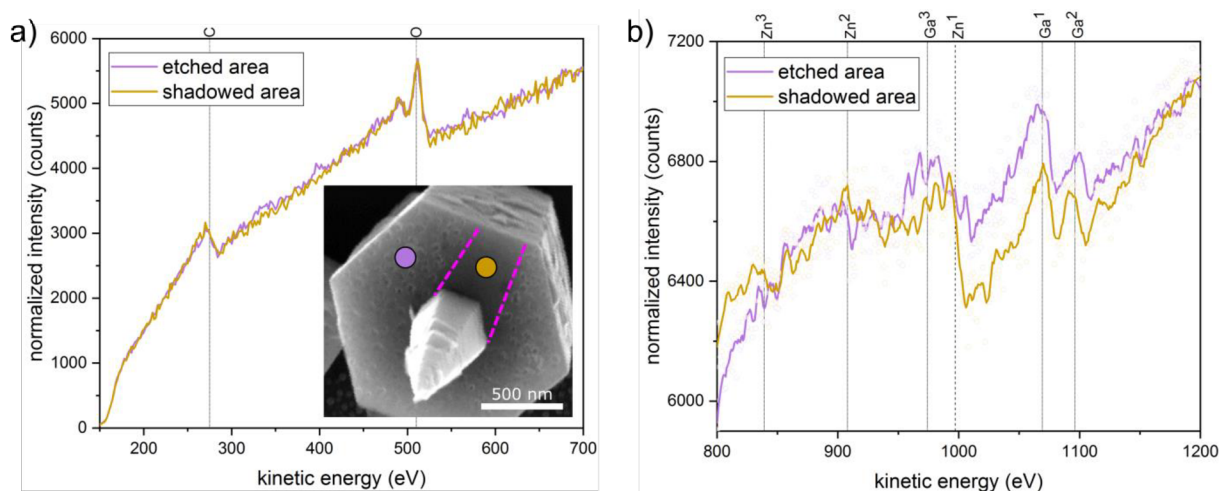

Fig. 49: Normalized AES spectra taken on different areas of the top facet of ZnO wire shown in Fig. 47d. Here, see the inset, where the location of spectra acquisition is illustrated (purple spot for the etched area, golden for the shadowed area). The spectra were acquired at 480 °C, i.e. at the end of the annealing procedure. a) Carbon and oxygen peaks are identical for both areas inspected. b) Gallium peaks were identified on both spots, including the area originally shadowed from gallium deposition. This indicates Ga surface diffusion into such areas during annealing. The zinc signal is high in the shadowed area and weak in the etched area (over-deposited with Ga in the beginning).

Cross-sectional STEM EDS & Diffusion model

The key question is whether gallium diffuses into the ZnO nanowires and if so, what is the diffusion kinetics like. This chapter presents STEM EDS characterization of the two distinct samples introduced above (i.e. V_O-rich and V_O-poor, differing in the pre-annealing environment) that underwent the gallium-treatment procedure. Cross-sectional lamellas cut from the nanowires are inspected. Out of the V_O-rich sample, two nanowires are characterized – the one utilized for the real-time SEM/AES characterization presented above and another one, not influenced by such examination. Subsequently, a nanowire from the V_O-poor sample is characterized. Further, a simple diffusion model is introduced, out of which the diffusion coefficients and diffusion lengths of gallium in such ZnO nanowires are extracted. At the end of the chapter, these quantities are compared for both samples.

In order to characterize the spatial distribution of gallium within the V_O-rich ZnO nanowires after the annealing process described above, a cross-sectional STEM EDS analysis was performed – see the

SEM micrographs of two selected nanowires in Fig. 50. The wire indicated in Fig. 50a is the same as observed during the annealing process in SEM/AES (i.e. the left wire in Fig. 47). This wire will be referred to as Wire-2 in further text. The other wire to undergo the EDS analysis (shown in Fig. 50b, referred to as Wire-1) has not been imaged or characterized before. This ensures that the wire has not been influenced by SEM or AES measurements. This might prove important, as the AES technique could lead to local heating of the sample – note the high current and electron energy used (1 nA, 10 keV). The location of the TEM lamellas cut from the wires is indicated by dashed red lines in Fig. 50. The aim is to inspect the cross-section of the wires and measure the EDS profiles of gallium. The samples were cut with a xenon-plasma focused ion beam (ThermoFisher Helios 5 PFIB DualBeam). (Note that a standard Ga FIB cannot be used as it would compromise the EDS measurement by possible gallium implantation.) The lamellas were cut perpendicularly to the substrate surface; therefore, they are *not* perpendicular to nanowire axes. This will be taken into account for the correct interpretation of gallium depth-profiles measured by EDS (see further text).
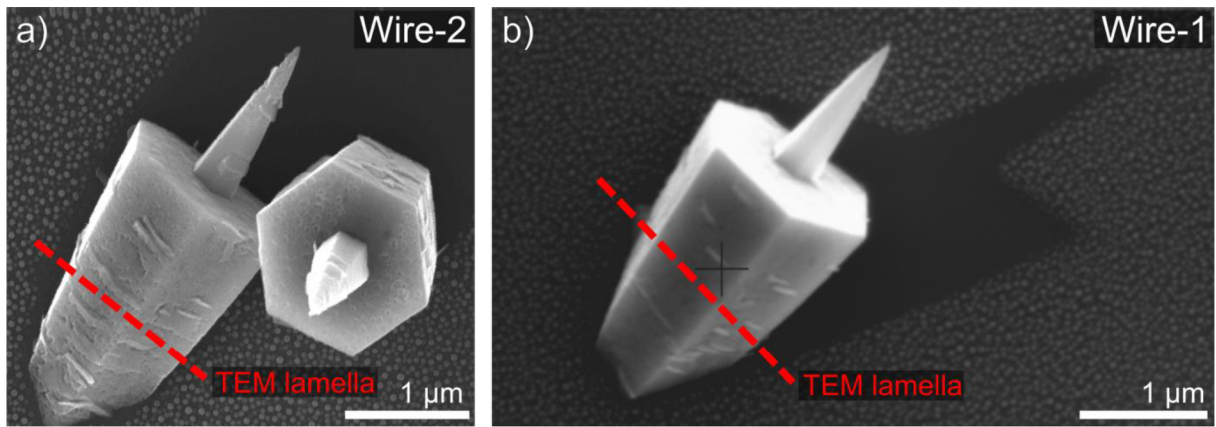

Fig. 50: ZnO wires from V$_O$-rich sample after Ga-incorporation procedure – location of the TEM lamellas for EDS characterization (indicated by red dashed lines).

Also, a clear shadowing effect is seen in Fig. 50. The wires are blocking part of the incoming gallium flux, hence creating a sharp silhouette on the sample surface. This is highlighted in Fig. 51, which shows the same image as in Fig. 50b with higher contrast and brightness. Gallium was deposited at room temperature at an angle of 30° with respect to the sample surface.

The SEM micrograph in Fig. 51 shows a top view of the sample. The x and y coordinates are defined in the substrate plane and marked in the Figure; the x, y and z axes make a right-handed coordinate system. Next, the following vectors are defined: $\overrightarrow{Ga}$ is the vector of incident gallium flux. $\vec{w}$ is a vector the direction of which is identical to nanowire growth axis and its length is equal to the length of the sidewall edge which casts a shadow onto the substrate due to gallium flux. $\vec{k}$ is a vector perpendicular to a selected sidewall (thus lying within the top facet); its length is defined by two non-adjacent vertices of the top facet of the wire. For better understanding, see the illustration in Fig. 51. In the Figure, it is possible to measure the projection of these vectors into the xy plane, marked Ga_{xy}, w_{xy} and k_{xy}, respectively. Further, the angles ρ, ε, μ are the angles between the x axis and the oriented projection of vectors $\overrightarrow{Ga}, \vec{w}, \vec{k}$, respectively. Given that the angle between the incident Ga flux and the substrate surface is 30°, the unit vectors are defined and calculated as follows:

$$\overrightarrow{Ga_J} = \frac{\overrightarrow{Ga}}{|\overrightarrow{Ga}|} = \cos(-30°) \cdot (\cos\rho, \sin\rho, \tan(-30°)), \tag{3.1}$$

$$\overrightarrow{w_j} = \frac{\vec{w}}{|\vec{w}|} = \frac{1}{\sqrt{1+\left(\frac{Ga_{xy}}{w_{xy}} \cdot \tan(+30°)\right)^2}} \cdot \left(\cos\varepsilon, \sin\varepsilon, \frac{Ga_{xy}}{w_{xy}} \cdot \tan(+30°)\right), \qquad (3.2)$$

$$\overrightarrow{k_j} = \frac{\vec{k}}{|\vec{k}|} = \frac{1}{\sqrt{1+\left[-\frac{w_{xy}}{Ga_{xy} \cdot \tan(+30°)} \cdot \cos(\mu-\varepsilon)\right]^2}} \cdot \left(\cos\mu, \sin\mu, \cos(\mu-\varepsilon)\right). \qquad (3.3)$$

The amount of deposited gallium is different for each facet on the wire due to its unique geometric orientation relative to the incoming Ga flux. Therefore, there are basically three-in-one independent experiments on the wire – one for every facet exposed. Having calculated the unit vectors of Ga flux (3.1) and sidewalls' normal (3.3), gallium dose for a particular facet (relative to a maximum Ga dose for a facet perpendicular to Ga flux) can be estimated based on the experiment geometry as a dot product of $\overrightarrow{Ga_j}$ and $\overrightarrow{k_j}$. This quantity calculated for each facet is presented as "Ga dose (SEM)" in Table 7. Based on (i) this geometric information, (ii) angles and distances measured in Fig. 51 and (iii) the fact that the main body of the nanowire is a right hexagonal prism (see section 3.2), the 3D geometric information about the wire can be calculated based on this 2D SEM micrograph. This is indeed necessary for the correction of EDS profiles, as the TEM lamellas are not cut perpendicularly to the wire axis.
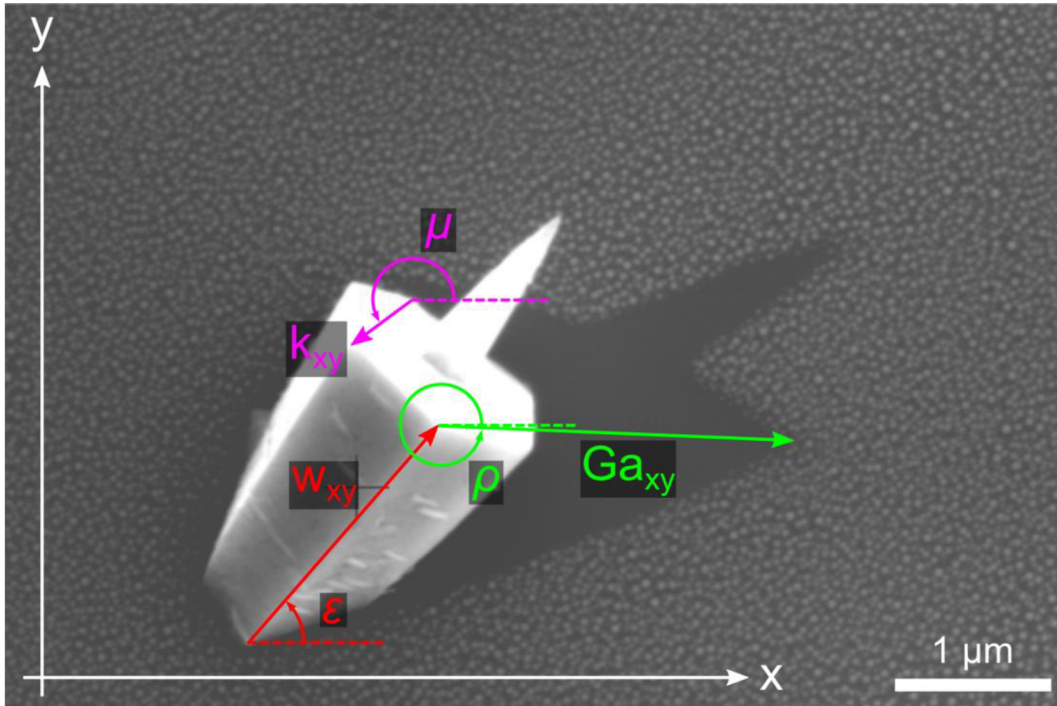
Fig. 51: Schematics of the distances and angles measured in the SEM top-view micrograph of ZnO wire over-deposited with gallium. The values are utilized in the diffusion model for EDS profiles correction.

The EDS elemental maps acquired from Wire-2 lamella (see its location in Fig. 50a) together with the HAADF image are presented in Fig. 52. (The EDS characterization was performed on ThermoFisher Talos F200i S/TEM microscope with Dual-X detectors.) The information of utmost importance is that gallium *does* penetrate into the ZnO wire, see Fig. 52a. This proves that the process used is applicable for the incorporation of gallium into ZnO, potentially leading to high doping levels. (Let's leave the question of dopant activation aside.) However, gallium is distributed inhomogeneously in two distinct ways:

- (i) Its concentration is higher near the wire surface (i.e. close to the original facets where Ga was deposited) and decreases towards the nanowire central axis. This is not surprising; it indicates a diffusive process that was stopped before the homogeneous concentration could be reached. This means that a longer annealing time shall be applied for a more homogeneous distribution of gallium. Another possibility – increasing the annealing temperature – is not recommended as it would promote the decomposition of ZnO (as discussed above).
- (ii) As can be seen in the Ga EDS map, there are brighter and darker spots and lines even for the same distance from the wire surface. This adds another level of inhomogeneity. (This will be further discussed for gallium depth-profiles extracted from this map, see Fig. 53c. The profiles are not monotonous near the surface in particular.) This points to strong surface effects having an impact; in particular, the ZnO decomposition (formation of etched-away pits on the surface, discussed earlier in this section) may play a role. Another fact that supports the presence of surface effects is the deficiency of Zn in the vicinity of wire facets – compare the EDS maps of zinc and oxygen and see the combined image in Fig. 52. These surface-related inhomogeneity effects are more pronounced on sidewall facets where more gallium was deposited (i.e. the top-left and the top-right facet in the view of Fig. 52, as opposed to the left facet – inferred from the inset SEM micrograph). This is in line with the previous conclusion that the decomposition of the ZnO surface is gallium-induced (see the AES results discussion above).

Based on these findings, more optimal experimental conditions will require lower annealing temperature (to prevent ZnO decomposition) and longer annealing time to counterbalance the decreased temperature and to promote more homogeneous gallium distribution within the wire.
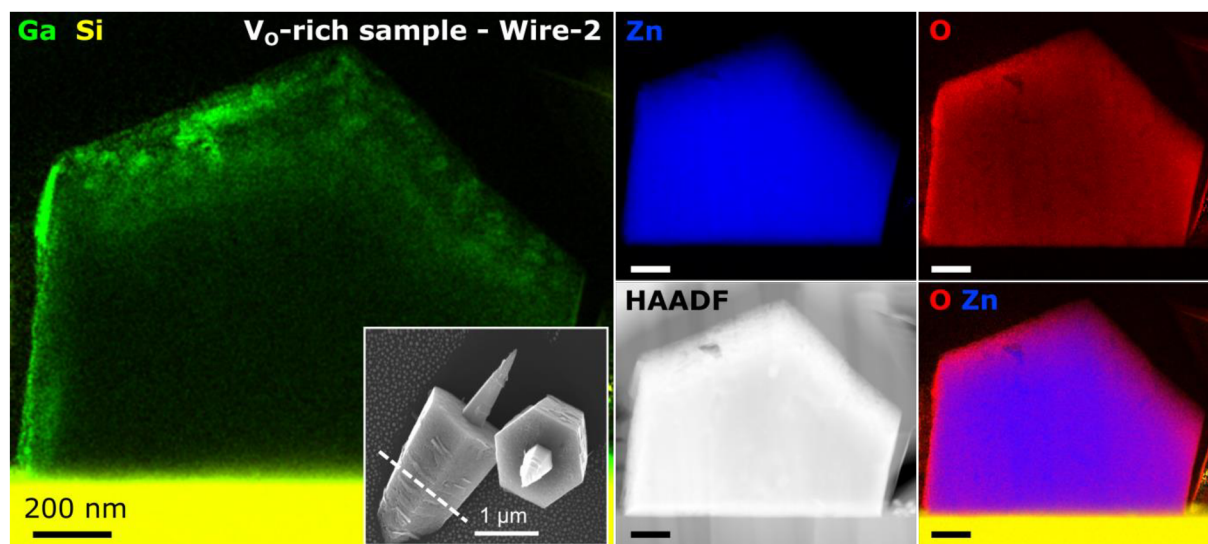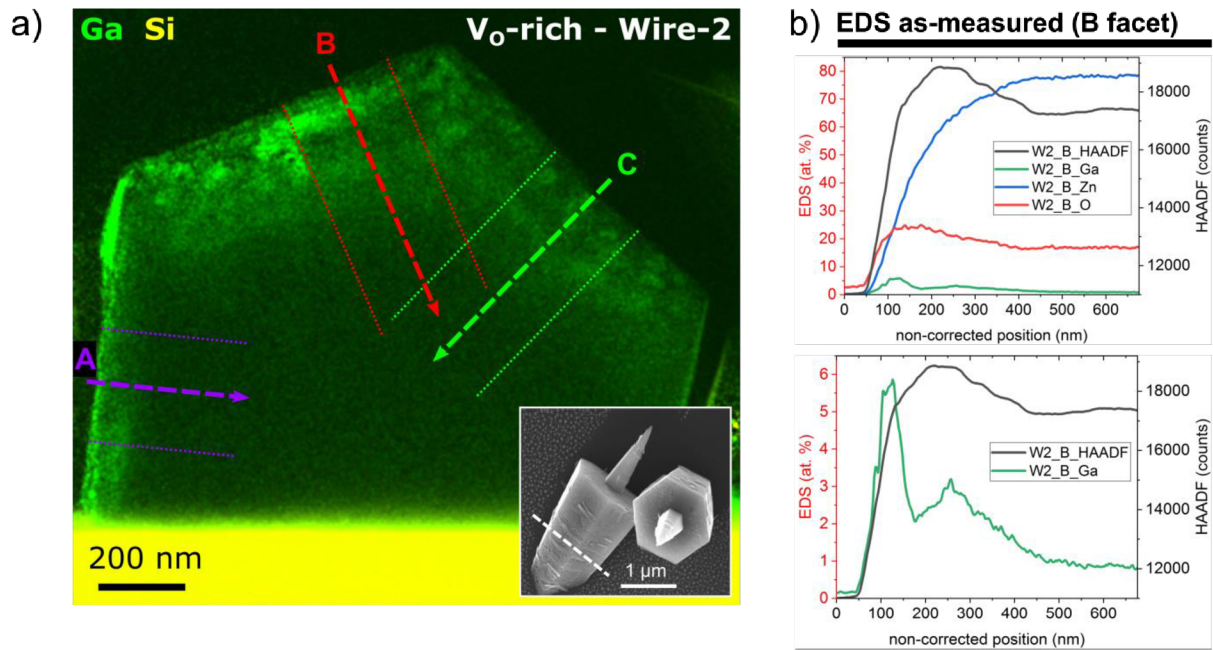

Fig. 52: STEM EDS maps of Wire-2 lamella from the V_O-rich sample. The location of the lamella (cut perpendicularly to the growth substrate) is shown in the inset (SEM top view, white dashed line) and also in Fig. 50a. Results for Ga, Si, Zn and O elements are presented, together with HAADF image and combined O+Zn map. Imaging: K. Bukvišová. Data analysis: author of the thesis.
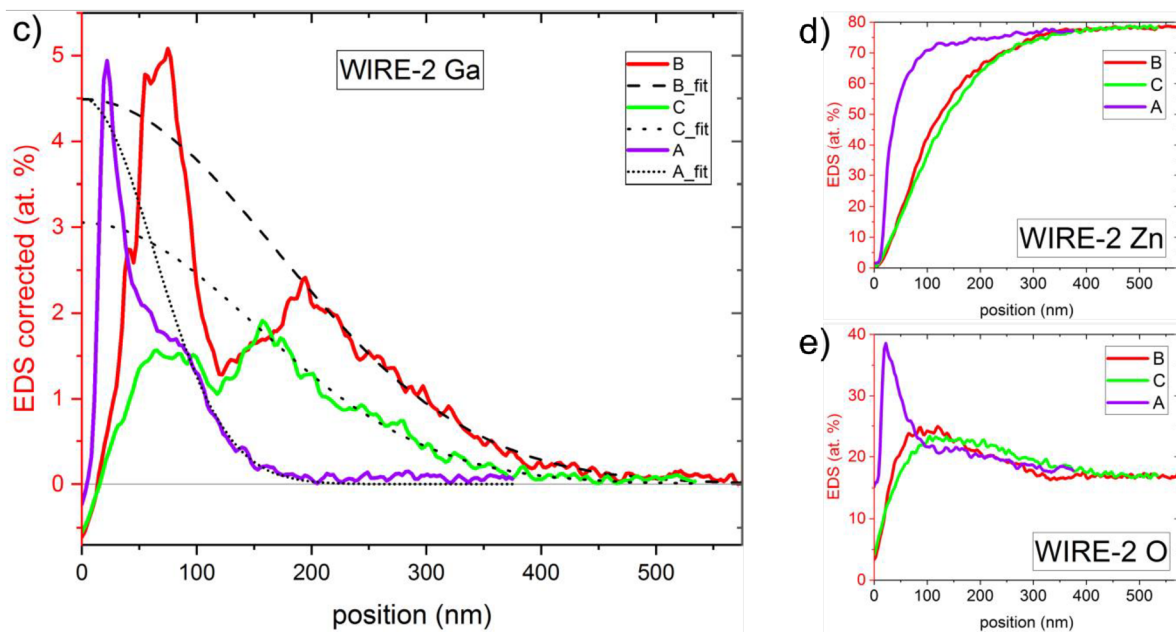
Fig. 53: ZnO Wire-2 (V$_O$-rich sample) EDS profiles. a) EDS map of Ga (green) acquired from the inclined cross-sectional TEM lamella. The location of the lamella within the wire is shown in the inset (take notice of the wire facets). The position of the elemental line profiles (perpendicular to lamella's edges) is indicated by coloured dashed lines (purple, red and green for the A, B and C edge, respectively). The line spectra are integrated over a 100px-wide area, indicated by the dotted lines of the same colour. b) To illustrate the data handling, the as-measured line spectra of the B profile are shown for Ga, Zn, O and HAADF signal. No correction is applied yet (see explanation in the text). The lower graph in b) shows a zoomed-in Ga spectrum from the upper graph. c,d,e) Corrected EDS depth-profiles of gallium, zinc and oxygen, respectively. After necessary corrections described in the text, the spectra represent real depth-profiles, perpendicular to nanowire sidewall facets A, B and C. The black dashed/dotted lines in c) show the Ga concentration profiles extracted from the diffusion model for A, B and C facets. (Note a good fit for the inner part of the profiles.) Also, pay attention to different colour-coding of the b) figure, which corresponds to the EDS maps shown in Fig. 52. In contrast, the colour-coding of c-e) reflects the schematics in figure a).

The depth-profiles extracted from the EDS maps will be presented and discussed hereafter. In Fig. 53a, the positions of line spectra of Wire-2 are indicated for sidewall facets labelled A, B and C. The EDS map was pre-filtered by applying 3px-averaging. The line spectra are integrated over a 100px-wide area (indicated by the dotted lines of the same colour; see the schematics ibid.). The as-measured EDS spectra and HAADF signal for the B facet (i.e. measured along the red dashed line indicated in Fig. 53a) are shown in Fig. 53b for illustration. The bottom graph ibid. (showing gallium profile) is a zoomed-in detail of the upper graph.

Several remarks are worth mentioning here:

- (i) The onset of both HAADF and EDS signals is clearly seen in Fig. 53b – it indicates the position where the wire begins. In further analysis, this position will be shifted to the origin of the x-axis (see Fig. 53c,d,e).
- (ii) The spectra of all the elements approach a certain constant value towards the centre of the wire – which is presumably pure ZnO. Interestingly, the values for zinc and oxygen are not near the expected 1:1 ratio, presumably due to the setup of EDS quantification calibration. Still, we are more interested in qualitative analysis – of gallium incorporation in particular. For the inner part of the wire, gallium approaches the value of approx. 0.8 at.%, which will be considered a zero baseline for gallium in Fig. 53c (taking into account the EDS detection limits and pure ZnO expected in the centre of the wire).
- (iii) Last but not least, correction of the x-axis of as-measured EDS spectra is needed. The x-axis in Fig. 53b indicates the position on the lamella shown in Fig. 53a. However, as the wire was originally inclined with respect to the substrate, the lamella was not cut perpendicularly to the wire axis. Therefore the measured position needs to be scaled (corrected) by a geometric factor individual for each facet. Only then the x-axis of EDS spectra will reflect the real depth-profile (in a direction perpendicular to the wire sidewall) and only then the measurements from the three facets can be correctly compared. This correction is already applied in Fig. 53c,d,e. The correction factor depends on the angle κ between the facet normal $\vec{k_j}$ and the unit vector $\vec{l_j}$ normal to the plane of the TEM lamella. Based on the quantities introduced in Fig. 51, the unit vector $\vec{l_j}$ is calculated as

$$\vec{l_j} = (\cos\varepsilon, \sin\varepsilon, 0) . \tag{3.4}$$

Then, the angle κ between the vectors $\vec{k_j}$ and $\vec{l_j}$ is

$$\kappa = \arccos\left(\vec{l_j} \cdot \vec{k_j}\right) = \arccos\left\{ \frac{1}{\sqrt{1+\left[-\frac{w_{xy}}{Ga_{xy} \cdot \tan(+30°)} \cdot \cos(\mu-\varepsilon)\right]^2}} \cdot \cos(\mu-\varepsilon) \right\} \tag{3.5}$$

and the corrected x-axis position is calculated

$$x = x_{EDS} \cdot \sin\kappa , \tag{3.6}$$

where x_{EDS} is the as-measured non-corrected position (shown e.g. in Fig. 53b) and x is the corrected position (reflecting the true depth-profile; applied e.g. in Fig. 53c,d,e).

Having applied the three types of corrections discussed above, graphs in Fig. 53c,d,e show the EDS depth-profiles of gallium, zinc and oxygen in the ZnO wire, going from its surface inwards. The measurements were done on three independent facets with different Ga dose deposited. The highest Ga dose was deposited onto the B facet, less onto the C facet and the least onto the A facet (see Table 7 for the exact values). The depth-profiles are compared directly for all facets, see the Figure.

For gallium profiles presented in Fig. 53c, it is clear that a substantial amount of gallium incorporates up to several hundreds of nm inside the wire. The penetration depth increases with the original Ga dose. Also, double-peak behaviour is observed for all the facets. The first maximum belongs to gallium trapped on or near the surface. The other maximum is due to Ga diffusing into the volume of the wire – therefore it is much more informative and valid for the assessment of diffusional incorporation of Ga into ZnO wires. This inner part of the depth-profiles (i.e. neglecting the part close to the wire surface) will be further incorporated into a simple diffusion model, see below. Regarding Zn profiles in Fig. 53d, a clear Zn deficiency near the surface area is seen for B and C facets, which are the ones with higher Ga dose deposited. This result corresponds to the EDS maps presented in Fig. 52. However, note that the behaviour of Ga and Zn profiles is not completely inverse – there is almost no difference between B and C profiles for zinc, whereas the difference in gallium profiles is substantial.

Generally, the gallium diffusion process follows Fick's second law, for 1D case being

$$\frac{\partial \varphi(x,t)}{\partial t} = D \cdot \frac{\partial^2 \varphi(x,t)}{\partial x^2} \, , \tag{3.7}$$

where $\varphi(x,t)$ is Ga concentration and $D = const.$ is the diffusion coefficient of Ga in ZnO for a given temperature T. (Keep in mind the dependence $D = D_0 \cdot e^{-\frac{E_a}{kT}}$. In case of another experiment performed at a different temperature, the activation energy of diffusion E_a and coefficient D_0 could be determined from the Arrhenius plot.) Solution of Fick's second law for limited-source diffusion – which is our case with a finite Ga dose deposited onto the ZnO wire – can be written in the following form [156]:

$$\varphi(x,t) = \frac{Q}{\sqrt{2Dt} \cdot \sqrt{2\pi}} \cdot e^{-\frac{x^2}{2(\sqrt{2Dt})^2}} \, , \tag{3.8}$$

which happens to be a Gaussian function of a normal distribution centred at zero (i.e. at the wire surface). Its standard deviation equals $\sqrt{2Dt}$. Let's define the diffusion length as $\lambda = \sqrt{Dt}$. The quantity Q represents the amount of gallium deposited on the facet; it will be called *effective Ga dose* in further text. It can be understood as the area below the concentration profile.

For each Ga profile in Fig. 53c, the inner part (neglecting the part near the wire surface due to reasons presented above) was fitted with equation (3.8) of the diffusion model and plotted into the graph as dashed and dotted black lines – see ibid. The annealing time t of 4500 s (i.e. the duration of annealing at the highest temperature, 480 °C) is considered for all facets. (The time needed to reach the final temperature is not considered for simplicity.) Based on the fitted curves, the following quantities are calculated individually for each facet: (i) effective Ga dose Q, (ii) diffusion length λ and (iii) diffusion coefficient D. The results are summarized in Table 7 (together with the results for Wire-1 from the same sample, discussed further below). Comparing the effective Ga dose with the dose

calculated geometrically, there are some variations; however, the trend is similar. Also, the diffusion length differs for the three facets – ranging from 44 nm to 120 nm. The diffusion coefficient varies accordingly. However, the exact numbers are not that important here. What matters is the overall magnitude of the diffusion coefficient D – lying within one order of magnitude.

Table 7: Summary of the data for the V_O-rich sample, extracted from EDS characterization and gallium diffusion model, both presented above. In total, six (independent) facets from two ZnO wires were characterized. *Ga dose* represents the amount of deposited gallium relative to deposition onto a facet perpendicular to Ga flux. It is calculated based on the geometrical setup of the apparatus and the sample. *Effective Ga dose Q* was extracted from the diffusion model based on fitted Ga profiles and calibrated with the Ga dose value 0.77 for B facet of Wire-2. This is used as a common reference for both wires. *Diffusion length λ* and *diffusion coefficient D* are extracted from the diffusion model. All of the values are based on the corrected EDS data.

Wire	Facet	Ga dose (SEM)	Effective Ga dose Q (EDS fit)	Diffusion length λ (nm)	Diffusion coefficient D ($m^2 \cdot s^{-1}$)	Comment
2	A	0.08	0.26	44	$4.4 \cdot 10^{-19}$	low direct Ga deposition
2	B	0.77 (ref.)	0.77	120	$32.1 \cdot 10^{-19}$	affected by AES measurement
2	C	0.55	0.45	107	$25.6 \cdot 10^{-19}$	affected by AES measurement
1	D	0.87	0.55	75	$12.5 \cdot 10^{-19}$	
1	E	0.88	0.23	50	$5.7 \cdot 10^{-19}$	
1	F	0.00	0.08	39	$3.4 \cdot 10^{-19}$	no direct Ga deposition

Nearly identical conclusions to those just discussed for Wire-2 can be drawn for the other wire (i.e. Wire-1) as well. Its EDS maps are presented in Fig. 54. Keep in mind that the two wires are from the same V_O-rich sample and have therefore undergone the same experimental procedure. There is one exception though – Wire-1 was *not* characterized by SEM/AES techniques at elevated temperature before the EDS measurements. Another difference between the wires is the amount of deposited gallium on individual facets – it is different for each facet of each wire due to their unique geometric orientation relative to the incoming Ga flux.

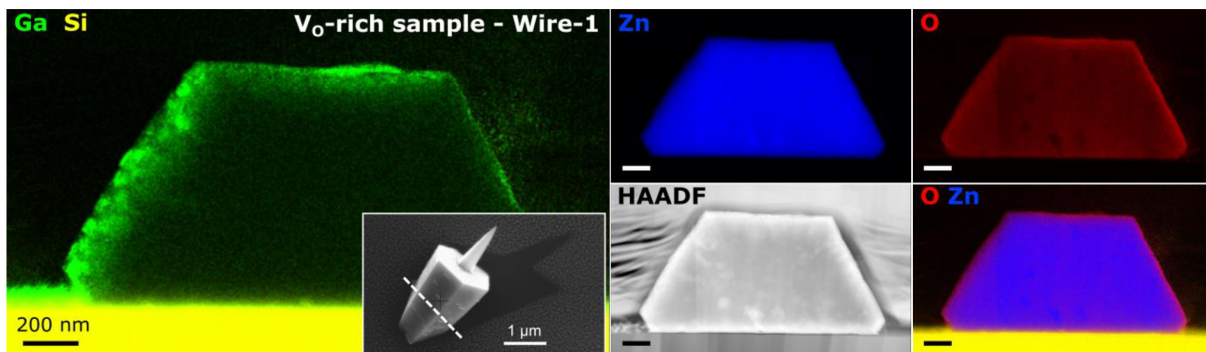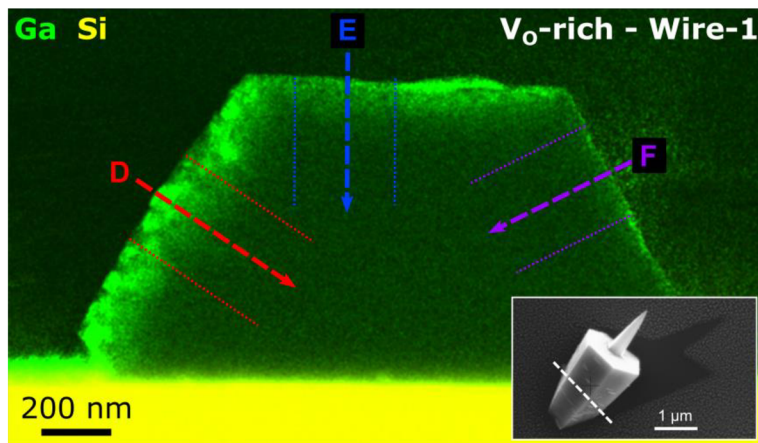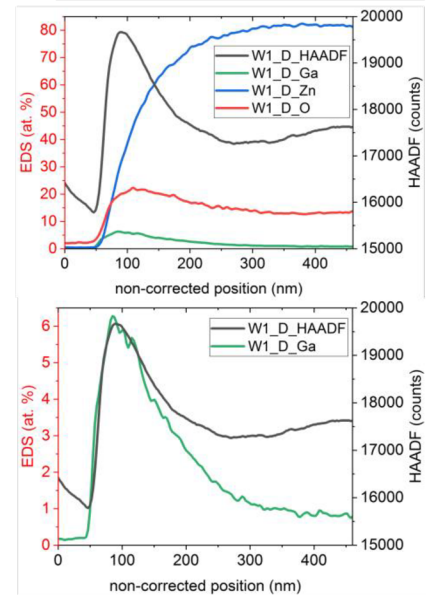**Fig. 54: STEM EDS maps of Wire-1 lamella (taken from the V_O-rich sample). The location of the lamella (cut perpendicularly to the growth substrate) is shown in the inset (SEM top view, white dashed line) and also in Fig. 50b. Results for Ga, Si, Zn and O elements are presented, together with the HAADF image and combined O+Zn map. Imaging: K. Bukvišová. Data analysis: author of the thesis.**
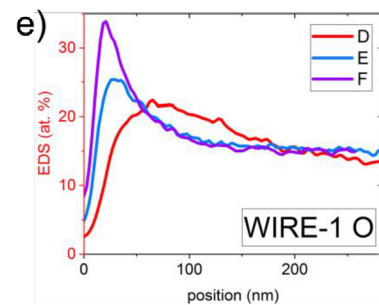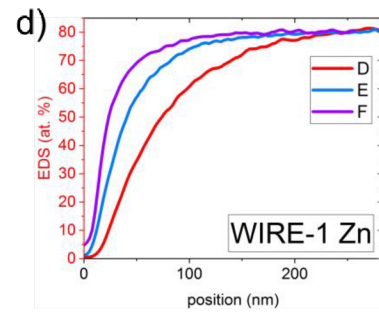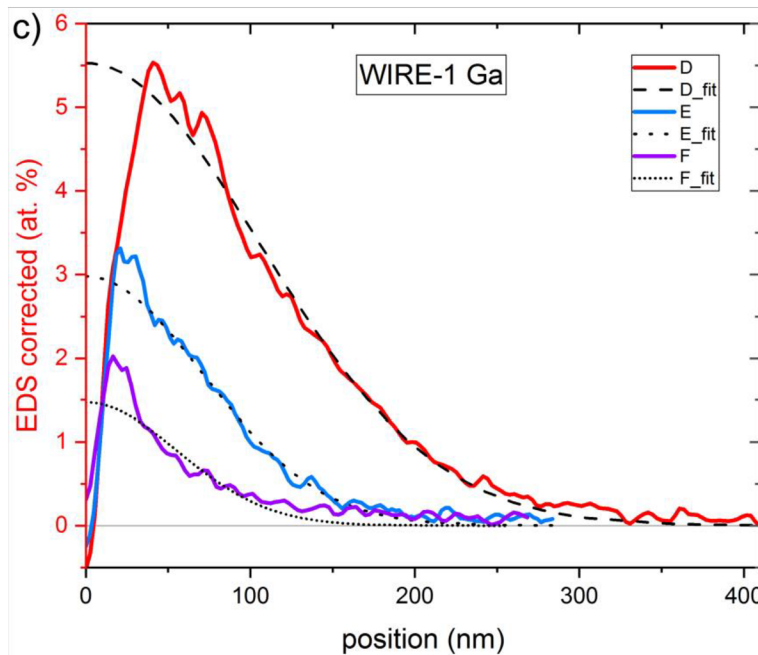
Fig. 55: ZnO Wire-1 (V$_O$-rich sample) EDS profiles. (The data layout is the same as in Fig. 53 for Wire-2). a) EDS map of Ga (green) acquired from the inclined cross-sectional TEM lamella. The location of the lamella within the wire is shown in the inset (take notice of the wire facets). The position of the elemental line profiles (perpendicular to lamella's edges) is indicated by coloured dashed lines (red, blue and purple for the D, E and F edge). The line spectra are integrated over a 100px-wide area, indicated by the dotted lines of the same colour. b) To illustrate the data handling, the as-measured line spectra of the D profile are shown for Ga, Zn, O and HAADF signal. No correction is applied yet (see explanation in the text). The lower graph in b) shows a zoomed-in Ga spectrum from the upper graph. c,d,e) Corrected EDS depth-profiles of gallium, zinc and oxygen, respectively. After necessary corrections described in the text, the spectra represent real depth-profiles, perpendicular to nanowire sidewall facets D, E, F. The black dashed/dotted lines in c) show the Ga concentration profiles extracted from the diffusion model for the D, E and F facets. Pay attention to different colour-coding of b) figure, which corresponds to the EDS maps shown in Fig. 54. In contrast, the colour-coding of c-e) reflects the schematics in fig a).

The same data processing as described above was applied to the EDS maps of Wire-1 lamella presented in Fig. 54. Location of the EDS depth-profiles on three distinct Wire-1 facets (labelled D, E, F) is presented in Fig. 55a. The unprocessed (non-corrected) EDS and HAADF spectra of the D facet are shown in Fig. 55b for illustrative purposes. More importantly, the corrected depth-profiles of Ga, Zn and O are depicted in Fig. 55c,d,e, respectively. The surface effects affecting the gallium profiles are much weaker, which is in line with the profiles' much more predictable behaviour. Apart from that, the qualitative conclusions are the same as for Wire-2 discussed above. Regarding the numerical values, see the summary for both wires in Table 7.

Two comments are worth pointing out:

- There was no direct deposition of Ga onto the F facet of Wire-1 (due to geometric setup). Still, the depth-profile in Fig. 55c shows a certain amount of gallium penetrating from this facet into the wire (see the purple profile). This can be explained by the surface diffusion of gallium from the E facet onto the F facet at first (when the temperature has been raised), followed by gallium incorporation. Indeed, both the effective Ga dose (thus being positive) and the diffusion length for the F facet are the smallest among all facets inspected – see the exact figures in Table 7.
- (ii) The range of Ga diffusion length for the Wire-1 facets (39 nm – 75 nm) is much narrower than for Wire-2 (44 nm – 120 nm) and the diffusion length is generally smaller. Together with the fact that the Ga depth-profiles of Wire-1 show smaller surface effects (including one maximum only), this indicates that the AES characterization of Wire-2 could have indeed influenced Ga incorporation by local heating of the B and C facets most exposed to the electron beam. Note that these facets show the highest diffusion length (120 nm and 107 nm) – a factor of 2 to 3 higher than the rest of the facets. Therefore, it is Wire-1 that is considered a more valid and credible reference for other measurements (e.g. the H_2O_2-preannealed wire presented below) or further research.

The EDS results for the V_O-rich nanowires presented above are to be compared with a V_O-poor ZnO nanowire. Its preparation was the same as for the V_O-rich sample except for the pre-annealing step, which was performed in H_2O_2 gas (30 min, 300 °C, 6 kPa) instead of vacuum. After cooling down in H_2O_2 gas, the sample was taken into another vacuum chamber, where Ga was deposited at room temperature (9 nm of Ga, flux direction 30° to the sample surface, chamber pressure $2 \cdot 10^{-6}$ Pa). Then the sample was transferred in-situ to the SEM/AES chamber with a base pressure $7 \cdot 10^{-9}$ Pa and annealed in vacuum (480 °C, 75 min) in order to perform gallium incorporation. SEM images of selected nanowires before and after the final annealing step are shown in Fig. 56. SEM results regarding morphological changes are the same as for the V_O-rich (i.e. vacuum-preannealed) nanowire: Gallium droplets on the decorated facets got consumed and the facets show rough morphology. The facets without gallium remained smooth and intact. Hence the gallium-induced decomposition of ZnO has been shown for this sample as well.
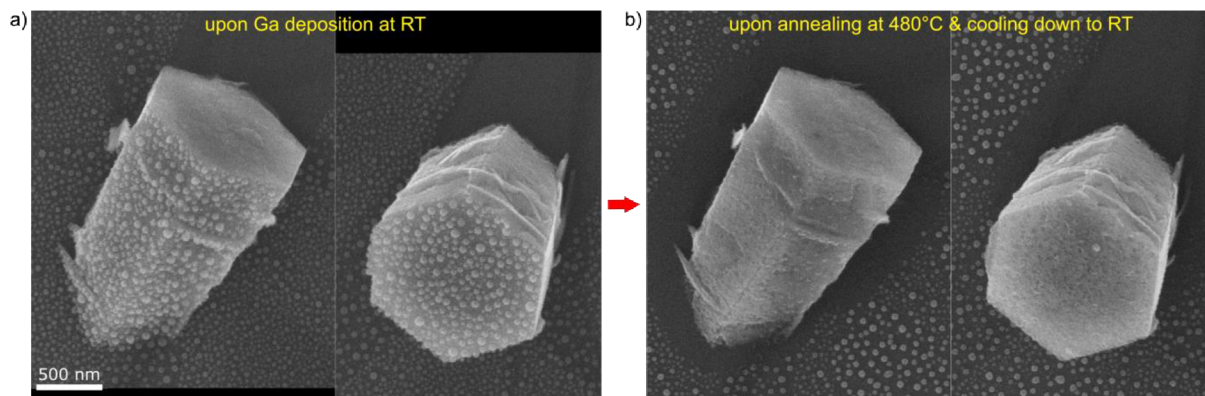
Fig. 56: SEM micrographs of the V_O-poor (i.e. H_2O_2-preannealed) ZnO wires taken a) upon Ga deposition at room temperature, b) upon subsequent in-situ annealing (480 °C, 75 min) and cooling down to room temperature for SEM imaging. Similarly to V_O-rich (i.e. vacuum-preannealed) ZnO wires (see Fig. 47 and Fig. 48), the annealing step induced Ga incorporation into ZnO wires and Ga-induced ZnO decomposition. The decomposition takes place only on areas originally decorated with gallium.

Further, a TEM lamella was cut from another nanowire for EDS inspection. The same instrumentation and procedures were used as for the V_O-rich sample presented earlier in this chapter. SEM image of the nanowire and location of the lamella are shown in the inset of Fig. 57. The EDS elemental maps and HAADF image are presented in the same Figure. The top-left and top-right sidewall facets were originally decorated with gallium. Clearly, Ga gets incorporated in a considerably inhomogeneous way – being located mostly at/near the wire surface and within the subsurface clusters. These clusters are probably correlated with the pores and hollows in nanowire sidewalls – see the rough surface morphology in Fig. 56b. This effect could be inhibited by applying lower annealing temperature (450 °C or less, as proved sufficient for Ga incorporation based on real-time SEM analysis shown in Fig. 47). However, for the sake of direct comparison, both V_O-rich and V_O-poor samples were annealed at the same temperature 480 °C for the same time of 4500 s. Similarly to the V_O-rich wires, weaker Zn signal is observed near the wire surface (see combined O+Zn image in Fig. 57) and it also correlates with stronger Ga signal (better seen in the EDS line spectra shown below, see e.g. the Ga protrusion on the G profile – compare blue spectra of Ga and Zn in Fig. 58c,d).

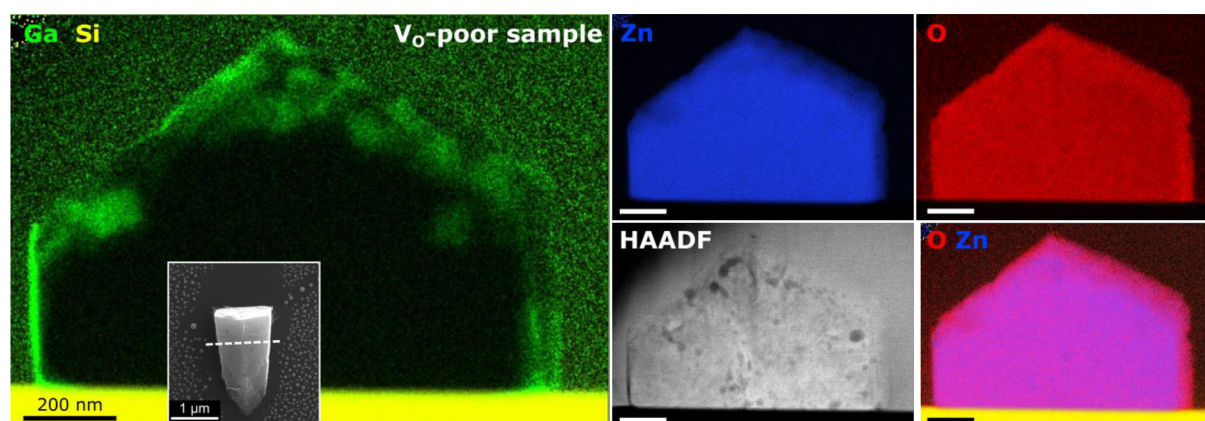**Fig. 57: STEM EDS maps of nanowire lamella taken from the V_O-poor sample. The location of the lamella (cut perpendicularly to the growth substrate) is shown in the inset (SEM top view, white dashed line). Results for Ga, Si, Zn and O elements are presented, together with the HAADF image and combined O+Zn map. Imaging: K. Bukvišová. Data analysis: author of the thesis.**

The depth-profiles extracted from the EDS maps are presented in Fig. 58. Positions of the line spectra are indicated in Fig. 58a – labelled G, H and J. The EDS maps were pre-filtered by applying 3px-averaging. The line spectra are integrated over a 60px-wide area (indicated by dotted lines of the same colour; see ibid.). The as-measured (i.e. non-corrected) EDS spectra and HAADF signal for the H line are shown in Fig. 58b for illustration. The bottom graph ibid. (showing gallium profile) is a zoomed-in detail of the upper graph. The corrected depth-profiles of Ga, Zn and O are depicted in Fig. 58c,d,e, respectively. The same correction procedure as for the V_O-rich sample was used (described above).

The positions of line spectra G and J were chosen on purpose, in order to show Ga-rich protrusions within the nanowire. However, homogeneous gallium incorporation is of more interest. Therefore, the H profile is studied further, as it covers the most homogeneous region of the lamella. Ga signal of H profile was fitted with the diffusion model presented earlier – see the black dashed line in Fig. 58c. The surface-affected area (marked with dotted line ibid., corresponding well to the projection of wire surface into the lamella plane due to the finite width of TEM lamella) was not considered in the fitting procedure. Annealing time t of 4500 s (duration of annealing at the highest temperature, 480 °C) was used as an input. Based on the fitted curve, diffusion length λ and diffusion coefficient D are calculated and summarized in Table 8 – for the purpose of comparing the V_O-rich nanowire (Fig. 55) with the V_O-poor one (Fig. 58). From the V_O-rich sample, Wire-1 was selected as more representative due to the reasons discussed above. Further, facet F was discarded, as there had been no direct Ga deposition on that facet, thus being unrepresentative for Ga incorporation evaluation.

Table 8: Comparison of the data extracted from EDS characterization and gallium diffusion model for V_O-rich and V_O-poor ZnO nanowire. *Ga dose* represents the amount of gallium deposited onto the sidewall relative to deposition onto an imaginary facet perpendicular to Ga flux. It is calculated based on the geometrical setup of the apparatus and the sample. *Diffusion length λ* and *diffusion coefficient D* are extracted from the diffusion model. All of the values are based on the corrected EDS data.

Wire	Facet	Ga dose (SEM)	Diffusion length λ (nm)	Diffusion coefficient D ($m^2 \cdot s^{-1}$)
V_O-rich sample (Wire-1)	D	0.87	75	$12.5 \cdot 10^{-19}$
V_O-rich sample (Wire-1)	E	0.88	50	$5.7 \cdot 10^{-19}$
V_O-poor sample	H	0.60	34	$2.6 \cdot 10^{-19}$

Comparing the EDS results of V_O-rich and V_O-poor ZnO nanowires leads to the following conclusions:

- Weaker Zn signal correlates with stronger Ga signal for both samples, being an indication of substitutional doping.
- Gallium incorporation is stronger and way more homogeneous for the V_O-rich ZnO nanowire (compare Fig. 55 and Fig. 58). Also, note the sharp boundary between Ga protrusions and ZnO material in the V_O-poor sample (well seen in G profile), further indicating that low concentration of oxygen vacancies inhibits Ga diffusion into ZnO.
- Gallium diffusion length in ZnO, as well as the diffusion coefficient, is larger for the V_O-rich nanowire (by a factor of 1.5 to 2.2 for λ; by a factor of 2.2 to 4.8 for D, see Table 8). Note however that this quantification serves as a rough estimate for drawing qualitative conclusions. In order to perform a quantitative study, more samples shall be inspected and surface effects would need to be considered in more detail.
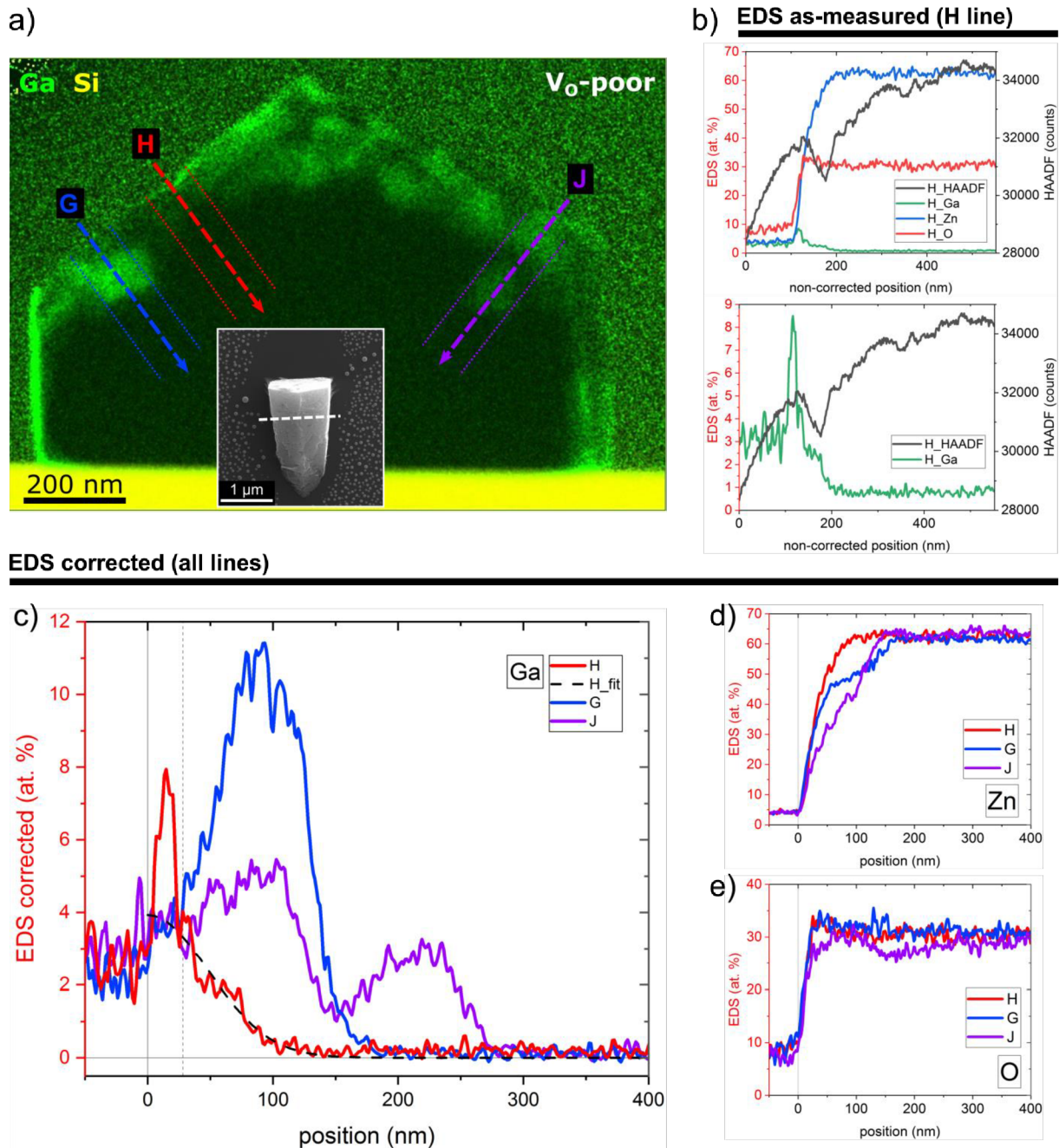
Fig. 58: EDS profiles of the V_O-poor nanowire. a) EDS map of Ga (green) acquired from the inclined cross-sectional TEM lamella (see its location in the SEM top-view inset). The position of the elemental line profiles (perpendicular to lamella's edges) is indicated by the coloured dashed lines. The line spectra are integrated over a 60px-wide area, indicated by the dotted lines of the same colour. **b)** For illustration, the as-measured line spectra of the H profile are shown for Ga, Zn, O and HAADF signal. No correction is applied yet. The lower graph in b) shows a zoomed-in Ga spectrum from the upper graph. **c,d,e)** Corrected EDS depth-profiles of gallium, zinc and oxygen, respectively. After the corrections described in the text, the spectra represent real depth-profiles, perpendicular to nanowire sidewall facets. In fig. c), the grey dotted vertical line (serving as a guide to the eye) separates the surface-influenced region of the H profile, which is not considered in the diffusion model. The black dashed line in c) shows the Ga concentration profile extracted from the diffusion model for H measurement. Beware of the different colour-coding of b) figure, which corresponds to the EDS maps shown in Fig. 57. In contrast, the colour-coding of c-e) reflects the schematics in fig a).

To summarize, Ga diffusional doping of ZnO nanowires has been proved. The pre-annealing environment (vacuum or H_2O_2 gas) indeed influences Ga incorporation into ZnO. Most probably, oxygen vacancies (prepared by vacuum-preannealing) promote higher gallium diffusion into the ZnO material. On the contrary, pre-annealing in H_2O_2 gas decreases the concentration of oxygen vacancies, thus suppressing Ga diffusion, which is then limited to ZnO crystal imperfections.

One of the thesis goals was to assess the Ga diffusional-doping procedure for ZnO nanowires, with respect to achieving high doping levels needed for novel applications. The suitability of this method was proved by the EDS measurements, showing successful gallium incorporation – with concentration up to several at.% in the subsurface regions (5 at.% for V_O-rich sample, 3 at.% for V_O-poor sample). Such measurements correspond to Ga concentration in the range of $2 \cdot 10^{21}$ cm^{-3} – $4 \cdot 10^{21}$ cm^{-3}, well suitable for plasmonics and bio-sensing applications. For practical use, way more homogeneous gallium distribution would be needed, yet this is feasible by prolonged annealing time. As a proof-of-concept, the diffusional-doping method used was shown to be a viable option for achieving high doping levels of gallium in ZnO nanowires.

Room-temperature photoluminescence

Room-temperature photoluminescence (PL) of the samples presented within section 3.4.2 above (V_O-rich and V_O-poor samples doped with gallium, differing in the pre-annealing environment only) was measured and compared with the as-grown nanowires. Samples with nanowire ensembles grown on Si substrate were used. All samples come from the same growth-batch. For characterization, a UV laser (355 nm) of 0.5 mW power and a UV-transparent 40× objective lens were utilised. Due to the detection range of the spectrometers, two of them were used – drawn with solid and dotted lines for UV and VIS range respectively, see Fig. 59. Each sample (as-grown, V_O-poor and V_O-rich) was characterized at several different positions (circa 0.5 mm apart; labelled P1 to P3), see the results in Fig. 59a. For ease of comparison, Fig. 59b shows the spectra normalized to the UV peak and sample-coloured only (disregarding measurement position on the sample). The detailed as-measured spectra of UV and VIS region are presented in Fig. 59c,d respectively. The UV peak at around 380 nm corresponds to ZnO near-band-edge region, while the broad green PL peak around 510 nm (consisting of multiple overlapping peaks as seen e.g. in Fig. 59d) is assigned to different ZnO crystal defects. In the literature, unambiguous assignment of specific defects to a particular PL wavelength is still under debate [110]. Nevertheless, the crystal quality is usually assessed by the intensity ratio of UV-to-VIS emission. Also, the VIS peak position is reported to be growth-method dependent [125]; vapour-deposited ZnO having a maximum around 550 nm (green PL, usually assigned to O vacancies), while solution-based ZnO showing a yellow-orange PL (580–600 nm) or even red-orange PL (620–730 nm, recently assigned to V_{Zn}–H complexes [113]). The nanowires used here – grown with the AACVD method (more in section 3.2) – show the maximum VIS intensity around 500–520 nm, being close to the vapour-deposition methods.

Although the spectra measured at different position of the same sample slightly differ (indicating sample inhomogeneity on a millimetre-scale probably due to growth- and annealing-temperature differences), several general conclusion may be drawn.

First, the UV-to-VIS ratio – corresponding to ZnO crystal quality – is the highest for the V_O-poor (i.e. the H_2O_2-preannealed) sample, followed by the as-grown ZnO-nanowire sample, and the lowest for the V_O-rich (i.e. the vacuum-annealed) sample (even being less than 1), see Fig. 59b and a summary

in Table 9. (Similarly, annealing in another oxidative environment – O_2 atmosphere – is also reported to increase the UV-to-VIS photoluminescence ratio [136]. In contrast, inverse results are described in [157], explained by the effect of surface band bending.) Given that our as-grown sample is in a certain state (regarding the crystal quality and concentration of different defects), its quality is improved by pre-annealing in H_2O_2 and worsened by pre-annealing in vacuum. Note that this had already been demonstrated on samples without Ga deposited [142]. This result is well in line with the fact that the concentration of O vacancies is altered by such annealing (as proved in section 3.3). Subsequently, Ga can incorporate differently into such-prepared samples. Interestingly enough, Ga indeed incorporates faster and deeper into the vacuum-preannealed nanowires, as presented above based on STEM EDS results. This leads to the conclusion that the presence of oxygen vacancies in ZnO facilitates gallium incorporation (or Ga diffusional doping).
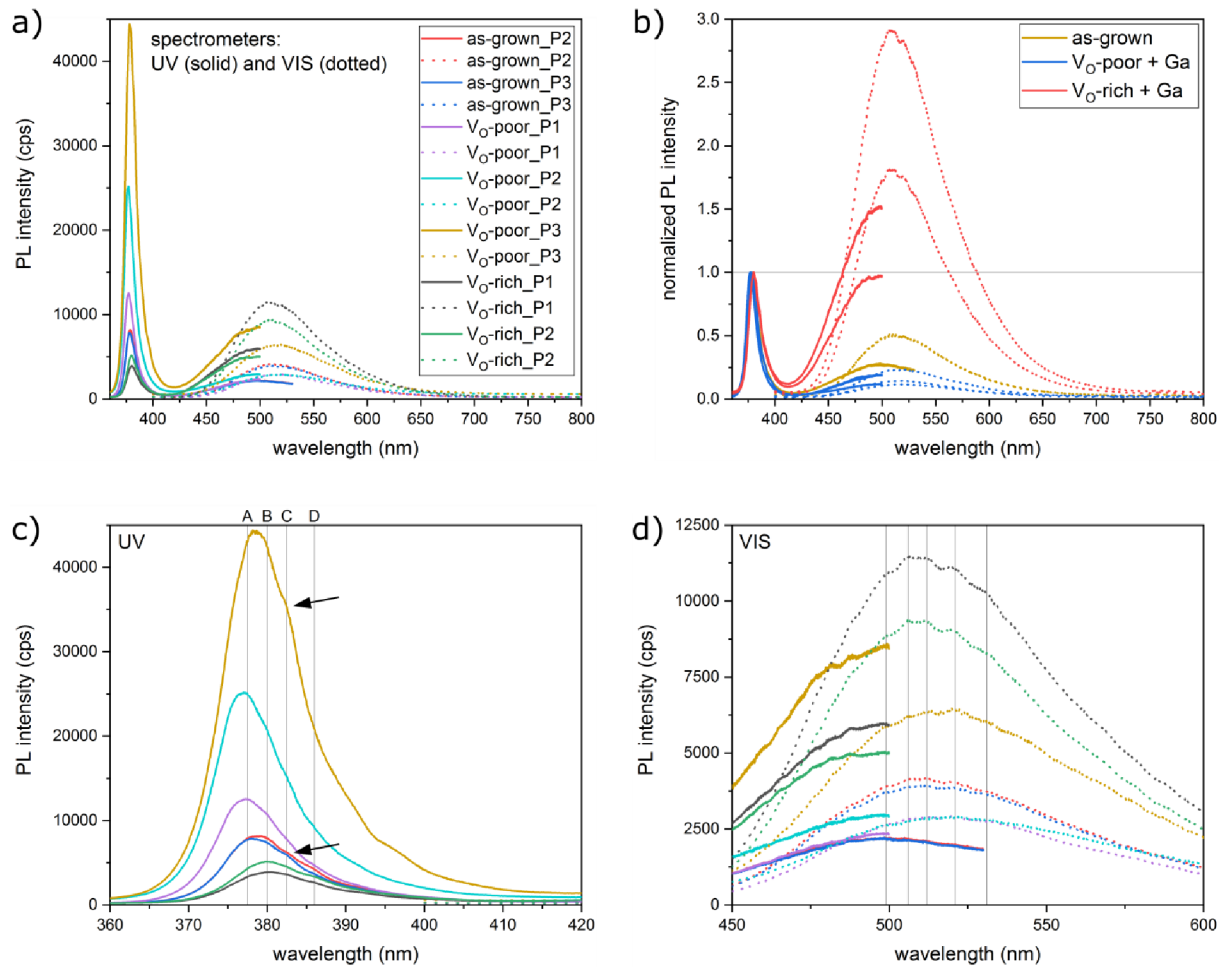
Fig. 59: Room-temperature PL characterization of the ensemble of as-grown ZnO nanowires, V_O-rich ZnO nanowires with subsequent Ga incorporation and V_O-poor ZnO nanowires with subsequent Ga incorporation. Solid and dotted lines represent the measurements recorded with a UV and VIS spectrometer, respectively. a) Summary of measurements at different positions of the samples. b) The same spectra as in a) normalized to the height of the UV peak of ZnO. All measurements taken from one sample are shown in the same colour (see the colour-coding in Table 9). c,d) Detailed view of the UV and VIS photoluminescence region, respectively. The legend is the same as in a). PL measurement: D. Citterberg. Data analysis: author of the thesis.

Second, the as-measured UV signal intensity corresponds to the UV-to-VIS ratio as well (V_O-poor sample being the highest, V_O-rich sample the lowest). Accordingly, the VIS signal intensity is reversed (with the exception of V_O-poor_P3 measurement).

Third, both the UV peak and the broad VIS peak are comprised of several sub-peaks (indicated in Fig. 59c,d with grey vertical lines as a guide to the eye). The UV peak may be composed of two main sub-peaks – labelled A (377.5 nm) and B (380 nm) in Fig. 59c. These two manifest themselves differently for the samples used; peak A being higher for the V_O-poor sample and peak B being higher for the V_O-rich sample. The as-grown sample lies in between. Probably, this is not a sign of Ga doping (albeit differently high), as the peak maximum shifts to opposite directions with respect to the as-grown sample. Further, two more contributions are spotted – position C at 382.5 nm (visible for all samples) and D at 386 nm (visible for V_O-rich and as-grown samples; less for the V_O-poor). For a more precise distinction of sub-peaks in both UV and VIS region, a low-temperature PL shall be applied.

Table 9: Summary of the UV-to-VIS PL intensity ratio measured at different positions of the as-grown ZnO nanowires, V_O-poor ZnO nanowires (H_2O_2-preannealed) with subsequent Ga incorporation and V_O-rich ZnO nanowires (vacuum-preannealed) with subsequent Ga incorporation.

Sample	Location	UV-to-VIS ratio	Colour-code in Fig. 59b
as-grown	P2	1.95	
as-grown	P3	2.00	
V_O-poor (H2O2+Ga)	P1	4.28	
V_O-poor (H2O2+Ga)	P2	8.60	
V_O-poor (H2O2+Ga)	P3	6.84	
V_O-rich (vac+Ga)	P1	0.34	
V_O-rich (vac+Ga)	P2	0.55	

4   Conclusion

The research presented within the thesis was focused on the growth and in-depth characterization of germanium and zinc oxide semiconducting nanowires, with the intention of acquiring high doping levels. Three main thesis objectives were defined in the introduction (chapter 1) and elaborated in subsequent chapters.

Ge nanowires

The literature review on the VLS growth of semiconductor nanowires using gold and non-traditional catalysts was summarized in section 2.1. Also, the incorporation of catalyst atoms into nanowires and the impact of surface adsorbates on nanowire growth were introduced.

Firstly, two elements of Ge nanowires' growth mechanism were studied in section 2.2 – the material transfer from the Au catalyst onto the nanowire and the impact of adsorbates passivating the sidewalls (atomic hydrogen in particular) onto nanowire growth and morphology. The experiments were performed either in vacuum conditions or with the assistance of atomic hydrogen, leading to dissimilar nanowire morphologies. The combined effect of atomic hydrogen adsorption and Au catalyst spreading on the growth direction and morphology was revealed and explained: It was shown that gold (diffusing out of the catalyst particle) promotes the formation of {111}-oriented sidewall facets, thus confining the nanowire growth into <110> direction. However, atomic hydrogen (if adsorbed on nanowire sidewalls) prevents gold from diffusing out of the catalyst. The nanowires then exhibit nearly cylindrical or hexagonal cross sections, as the growth is not constrained by any preferential sidewall orientation. Moreover, these results bridge the gap between the MBE and CVD growth methods, explaining their contradictory results – regarding nanowire growth direction in particular. The findings presented in the thesis bring additional insight into the explanation of Ge nanowire growth mechanism in general, highlighting the importance of surface adsorbates – being present on purpose (MBE setup) or unintentionally (most of the CVD methods, where hydrogen-containing adsorbates are generated as a by-product).

Secondly, Ge nanowire growth using dopant-containing catalysts was investigated in section 2.3 – with the intention of catalyst incorporation leading to nanowire doping. The alloyed Au–Ga catalyst was prepared and imaged in-situ during formation, followed by the successful growth of Ge nanowires – although the catalyst stability is lower than for pure Au. The presence of gallium in the catalyst atop the nanowire was confirmed by Auger electron spectroscopy and STEM EDS analysis. However, gallium incorporation from the catalyst into the nanowire was not observed. Next, nanowire growth from pure-Ga and pure-Al catalyst was not achieved due to inhibited Ge diffusion on the growth wafer and catalyst instability on Ge structures. Growth from alloyed Au–In catalyst was successful, leading to in-plane Ge nanowires on (110)-oriented Ge wafer. To summarize, only the alloyed Au–Ga catalyst was found to be applicable for germanium out-of-plane nanowire growth – out of several material combinations studied. Despite high dopant concentration in the catalyst, no gallium incorporation into the nanowire was reached. Hence, this method of nanowire doping was proved unsuitable for the material system selected.

ZnO nanowires

Thirdly, the development of a procedure for high-level doping of ZnO nanowires was described in chapter 3. Literature review on ZnO material in general and ZnO nanowires was presented in section 3.1 – with emphasis on electronic properties, n-type doping and detection of oxygen vacancies in the material.

ZnO nanowires utilized for our experiments were grown via the AACVD method (aerosol-assisted CVD), more details of which were introduced in section 3.2. First, the as-grown nanowires were characterized (section 3.3). Based on Raman measurements, it is recommended to use only rod-like nanowires (as opposed to needle-like ones) from a single NW growth-batch for any further comparative study – for the sake of better repeatability of results. A widely-used method for the characterization of nanowires' electronic properties (including doping-level assessment) is the IV-curve measurement. Such a measurement of individual ZnO nanowire was demonstrated. However, an inappropriate metallization scheme was employed. A more complex study would need to be performed in order to optimize and tailor the process and to obtain reasonable results.

In the last part of section 3.3, the impact of nanowire annealing in various environments on the concentration of oxygen vacancies was demonstrated based on XPS measurements. Annealing in H_2O_2 gas substantially decreases the concentration of O vacancies in ZnO, compared to annealing in high vacuum.

Further, the procedure for diffusional doping of nanowires with gallium was described in section 3.4.1, including the basic results of Raman, XPS and HRTEM characterization of the gallium-treated nanowires. Based on these measurements, an optimized procedure was defined, implementing several improvements:

- Performing Ga deposition and annealing in UHV conditions in order to prevent gallium oxidation during the process.
- Leaving out Raman characterization as not effective for our samples, for which the nanowires are grown on silicon substrate. Strong Raman peaks of Si overlap with ZnO peaks and potential dopant-induced additional modes. This makes the assessment of doping levels virtually impossible. (A plausible way to overcome this limitation would be to grow ZnO nanowires on a sapphire substrate instead of silicon. This has not been performed for this thesis.)
- Combining the XPS and HRTEM results, gallium incorporation into ZnO nanowires was indirectly confirmed. For direct and conclusive assessment of Ga spatial distribution within the treated nanowire, STEM EDS of nanowire lamellas is used further.

Results obtained using the optimized doping procedure are discussed in section 3.4.2. The process of Ga incorporation into ZnO nanowires during annealing was documented in-situ in real time in the SEM/AES apparatus. The decrease in volume of deposited gallium (indicating its incorporation into zinc oxide) was evident already at 350 °C. Having increased the temperature to 450 °C, gallium completely incorporated and smooth ZnO facets were seen. When further increasing the annealing temperature, gallium-induced decomposition of ZnO nanowires was observed. This leads to the formation of etched-away pits on nanowires' facets on areas of previous Ga deposition; regardless of the pre-annealing conditions. The evidence for distinguishing between ZnO thermal decomposition

as such and Ga-induced process was shown and discussed. (Bare ZnO nanowires were stable up to 535 °C at least, when annealed in vacuum.)

Next, the STEM EDS characterization of nanowire cross-sectional lamellas is presented. The extent of Ga incorporation was studied for two distinct samples (with a high and a low concentration of oxygen vacancies, labelled V_O-rich (vacuum-preannealed) and V_O-poor (H_2O_2-preannealed), respectively) – in order to correlate Ga diffusion and the concentration of oxygen vacancies in the nanowires. Furthermore, a model for gallium diffusion into ZnO nanowires was implemented. Based on the diffusion model and EDS line spectra, diffusion coefficient and diffusion length were calculated for each sample. For both samples, a stronger Ga signal correlates with a weaker Zn signal, indicating substitutional doping. Gallium incorporation into ZnO nanowires was proved for both samples. For the V_O-rich sample, the diffusion coefficient of gallium in ZnO (and hence the diffusion length as well) is larger than for the V_O-poor sample. Also, the spatial distribution of Ga is more homogeneous within the V_O-rich nanowire.

To summarize, diffusional doping of ZnO nanowires with Ga was demonstrated and the suitability of various methods for doping-level analysis was assessed. The pre-annealing environment influences Ga incorporation into ZnO nanowires. The oxygen vacancies generated by vacuum-preannealing most likely promote higher and more homogenous gallium diffusion into ZnO material. By contrast, pre-annealing in H_2O_2 gas (which decreases the concentration of oxygen vacancies), suppresses Ga diffusion compared to oxygen-vacancy rich nanowires. Based on the EDS measurements, gallium concentration as high as $4 \cdot 10^{21}$ cm^{-3} was reached in the subsurface region of the V_O-rich ZnO nanowire and up to $2 \cdot 10^{21}$ cm^{-3} for the V_O-poor nanowire. Hence, the suitability of the presented diffusional-doping method for achieving high Ga doping levels in ZnO nanowires was demonstrated. Provided that Ga concentration homogeneity is improved by prolonged annealing time and the dopant activation is sufficient, the doping-method presented above is a viable option for reaching high doping levels of ZnO nanowires (in the order of 10^{21} cm^{-3}) needed for prospective applications, such as bio-sensing in the IR region.

As an outlook of the prospective direction of further activities, a few points are proposed hereafter:

- Compared with the optimized procedure from section 3.4.2, more optimal experimental conditions shall include lower annealing temperature (in the range 350–450 °C) and longer annealing time (several hours); with the aim of (i) preventing Ga-induced ZnO decomposition in order to achieve smoother surface morphology, enabling easier and more precise EDS evaluation, (ii) promoting more homogeneous gallium distribution within the nanowires (longer annealing time counterbalances the decreased temperature).
- More samples shall be inspected with STEM EDS to draw solid quantitative conclusions to Ga diffusion parameters. Surface effects shall be considered in more detail, if not reduced significantly by the previous point. Cross-calibration of EDS concentration of incorporated gallium with SIMS method (secondary-ion mass spectroscopy) would be beneficial.
- Within chapter 3, solid evidence was presented that gallium incorporates into ZnO nanowires when the optimized diffusional-doping procedure is applied – preserving the single-crystalline ZnO structure. However, the effect of Ga doping on the electronic properties of the nanowires (and the question of dopant activation) remains to be confirmed by transport measurements. An optimized metallization scheme was proposed in section 3.3.

- Further, a comparative study of Ga and Al dopant incorporation will be of high interest, based on the established procedure. Operating the apparatus that combines UHV deposition and in-situ real-time AES/SEM imaging may also bring valuable insight into the incorporation of other elements not only for electronic applications (mind, for example, doping with magnetic elements).

5 The gallery of unpublishable arts

As promised in the introduction, this chapter presents a few examples of the unused images acquired during the work on the thesis. Although they are virtually unpublishable – (note the contradiction in this very sentence, being published) – they still show an aesthetical aspect of scientific failures, which may please the eye and heart of the respected reader.
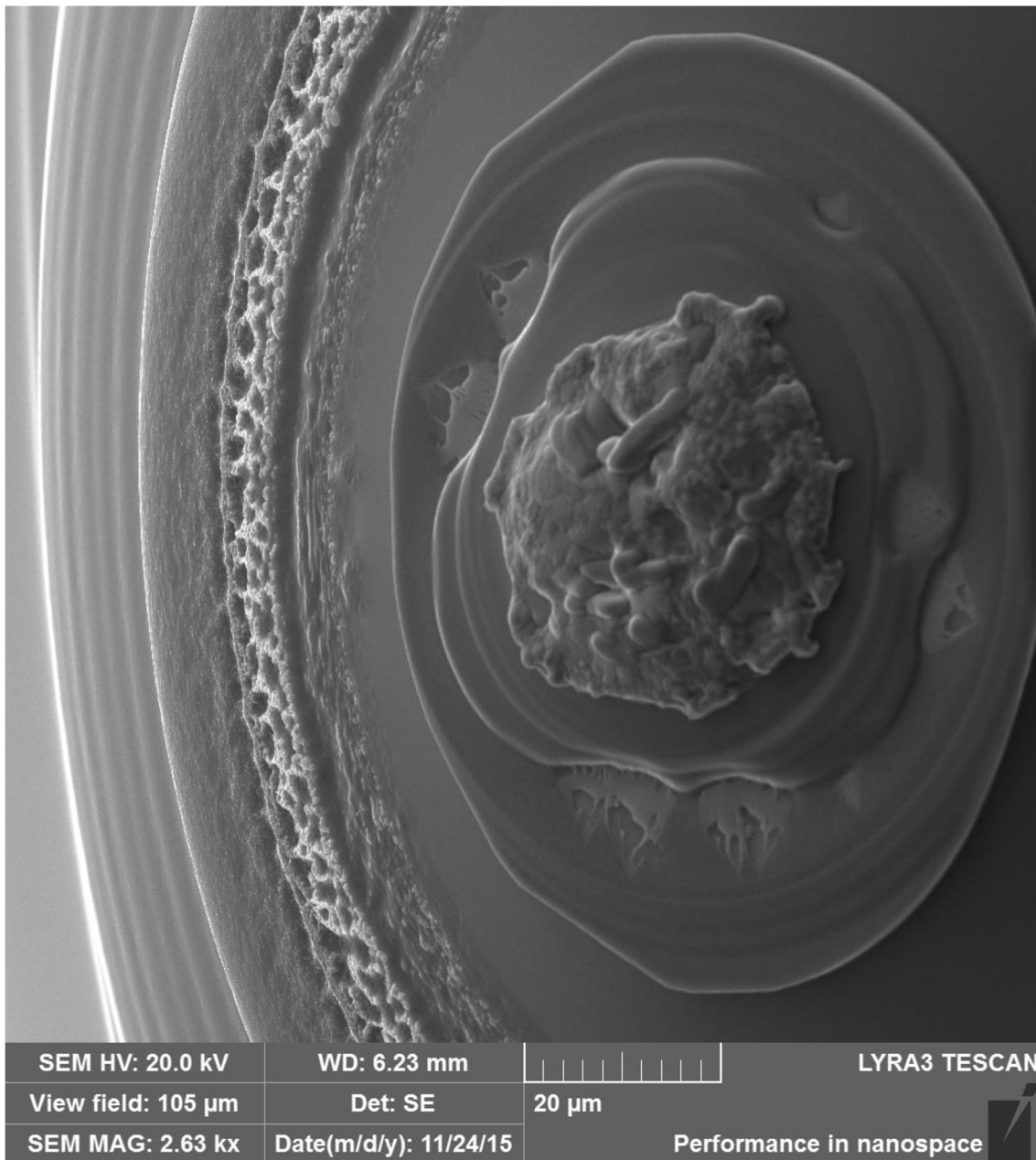
Fig. 60: Molten and re-solidified germanium wafer.

HV	curr	mag ☐	HFW	WD	det	mode	
5.00 kV	6.3 pA	82 877 x	5.00 µm	3.3 mm	TLD	SE	⊢———— 1 µm ————⊣
							CEITEC Nano
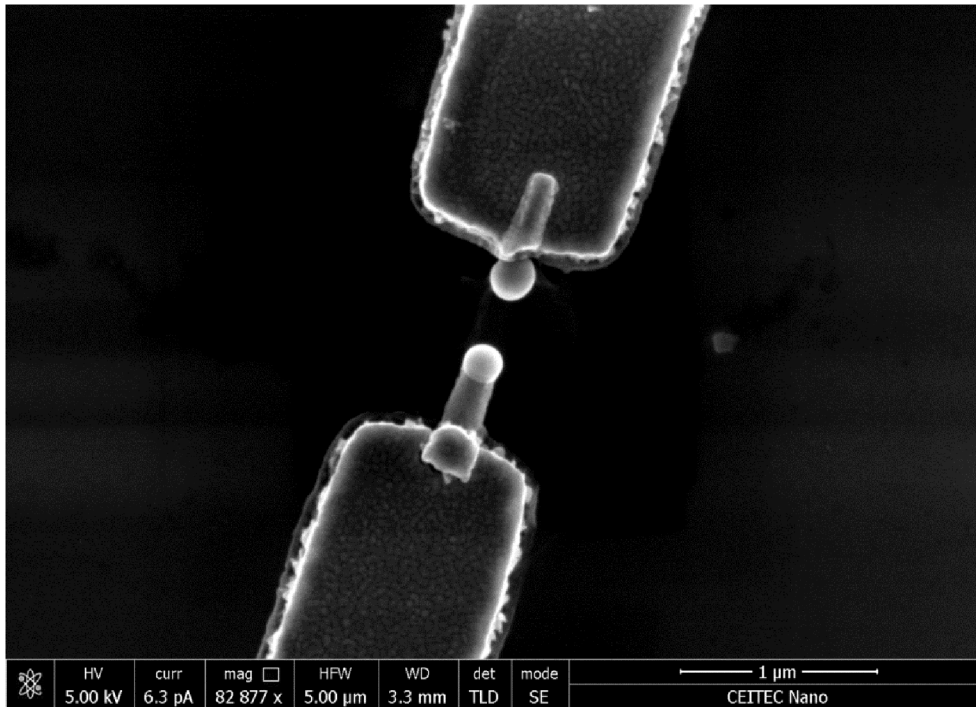
Fig. 61: Failed it has! (No I–V measurement today.)

SEM HV: 20.0 kV	WD: 13.06 mm		LYRA3 TESCAN
View field: 10.00 µm	Det: SE	2 µm	
SEM MAG: 27.7 kx	Date(m/d/y): 04/12/16		Performance in nanospace

Fig. 62: Vertical Au nanowalls on Ge prepared by EBL – a residue of the imperfect lift-off process.

86
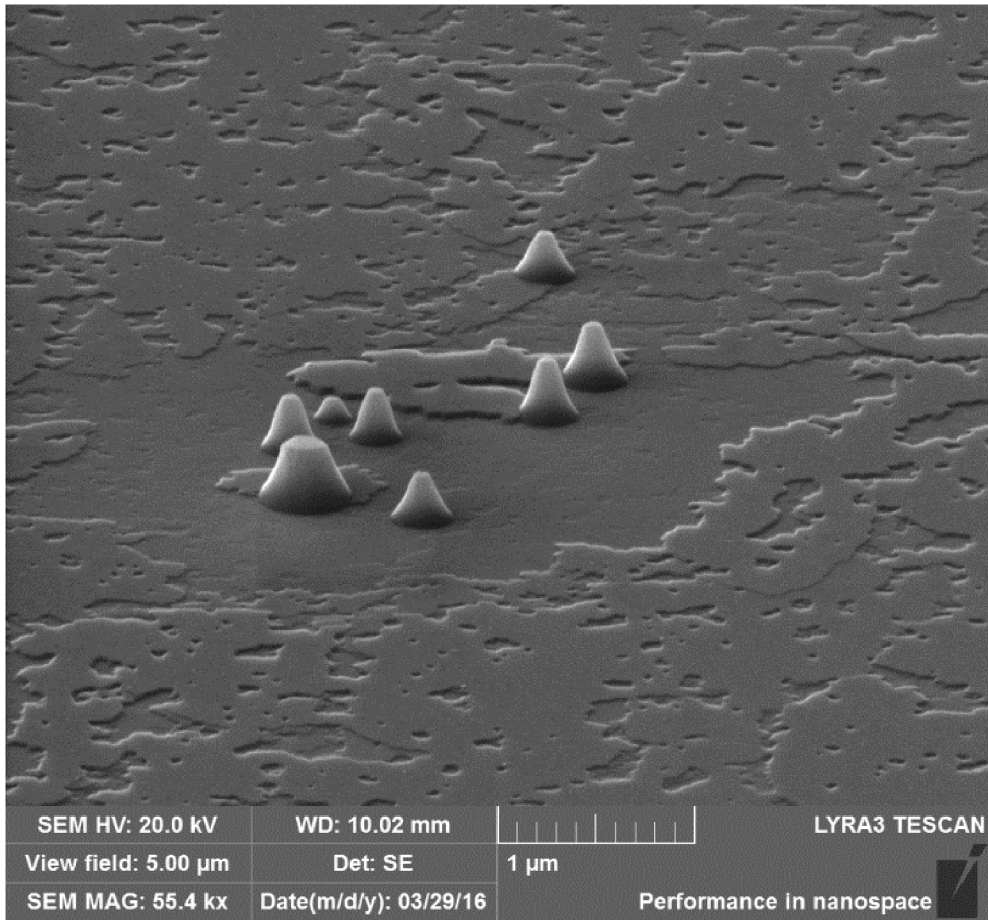
Fig. 63: A volcanic landscape: Is it Mars or České středohoří?
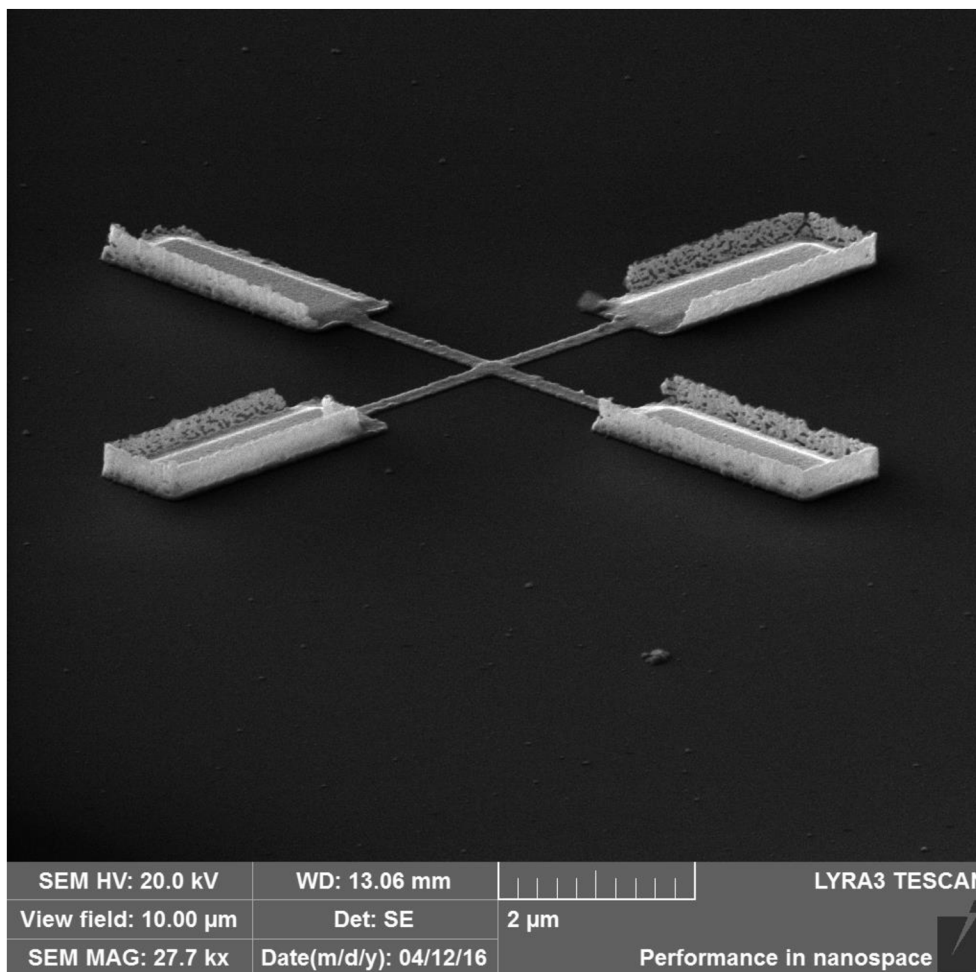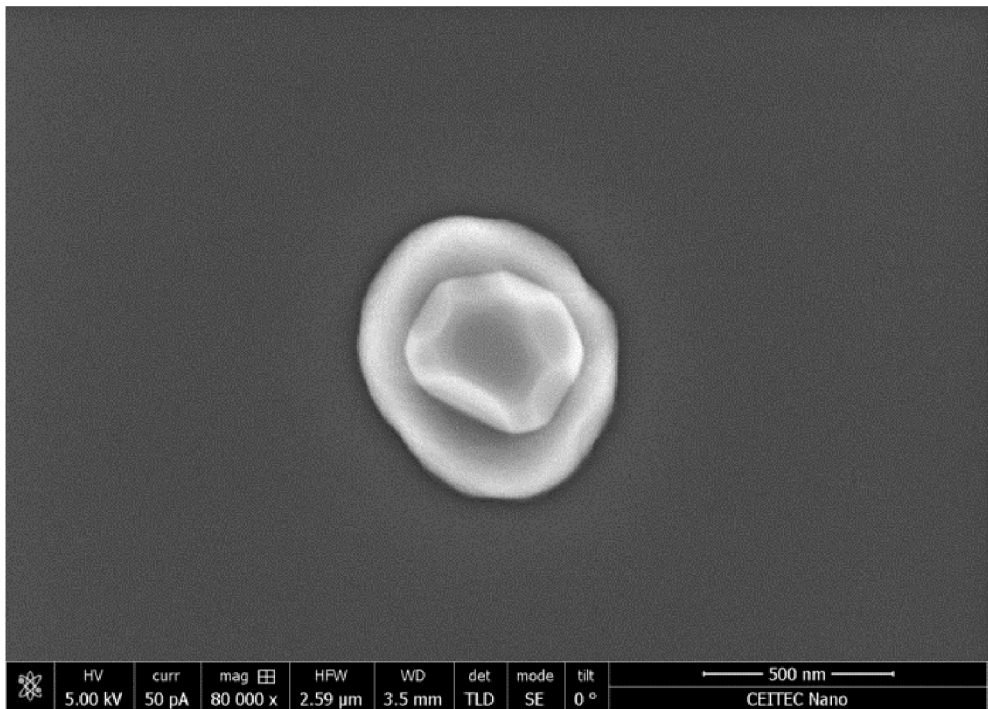

Fig. 64: A hidden gemstone – gold recrystallized within indium bath.
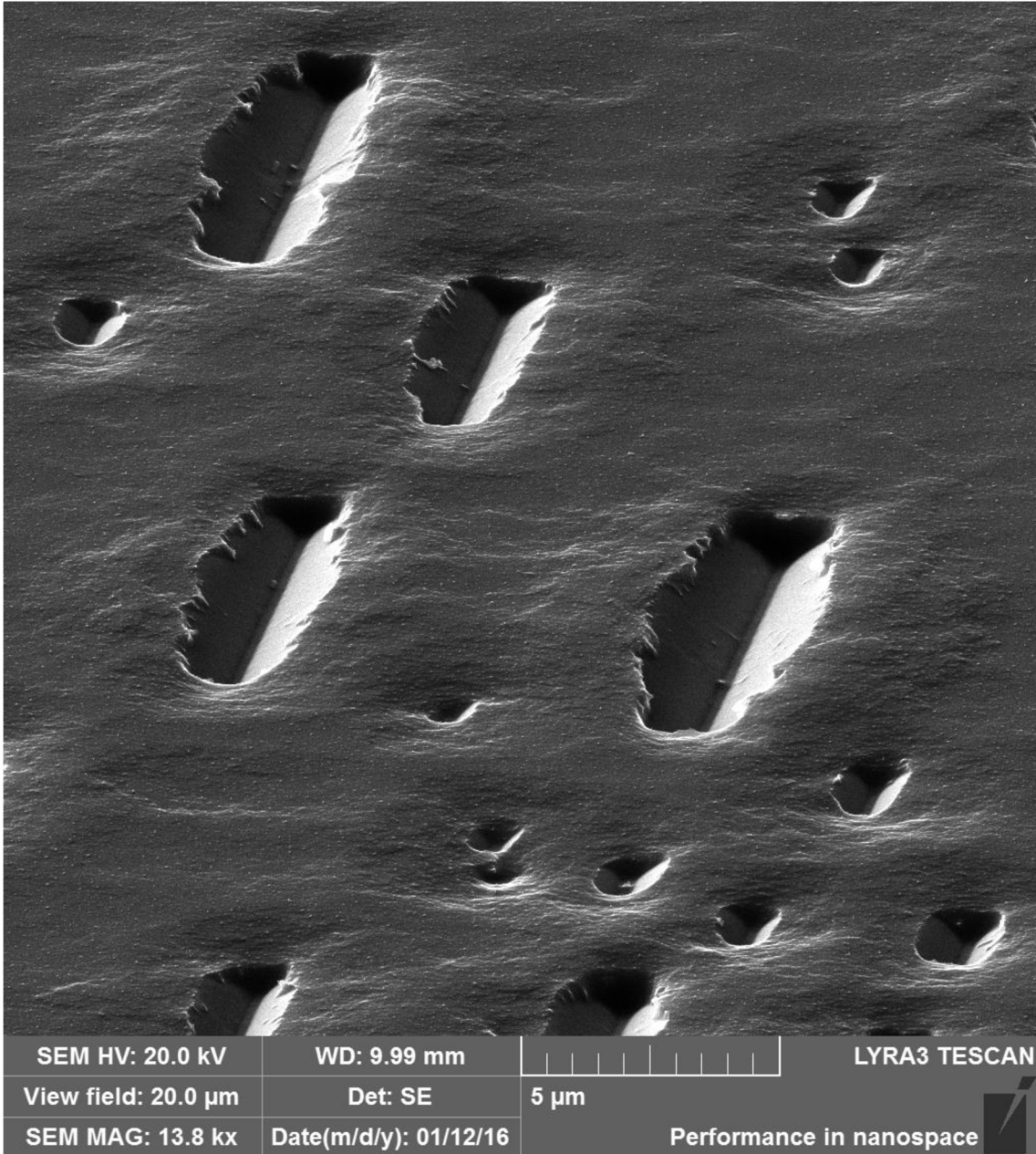
Fig. 65: Germanium {111} facets revealed by high-temperature anisotropic etching of Ge(110) substrate.

SEM HV: 10.0 kV	WD: 8.02 mm		LYRA3 TESCAN
View field: 5.00 µm	Det: SE	1 µm	
SEM MAG: 55.3 kx	Date(m/d/y): 06/03/15		Performance in nanospace

Fig. 66: Cu nanocubes self-assembled on graphene/Cu substrate after deposition of Au nanoparticles (bright dots) from colloidal solution.
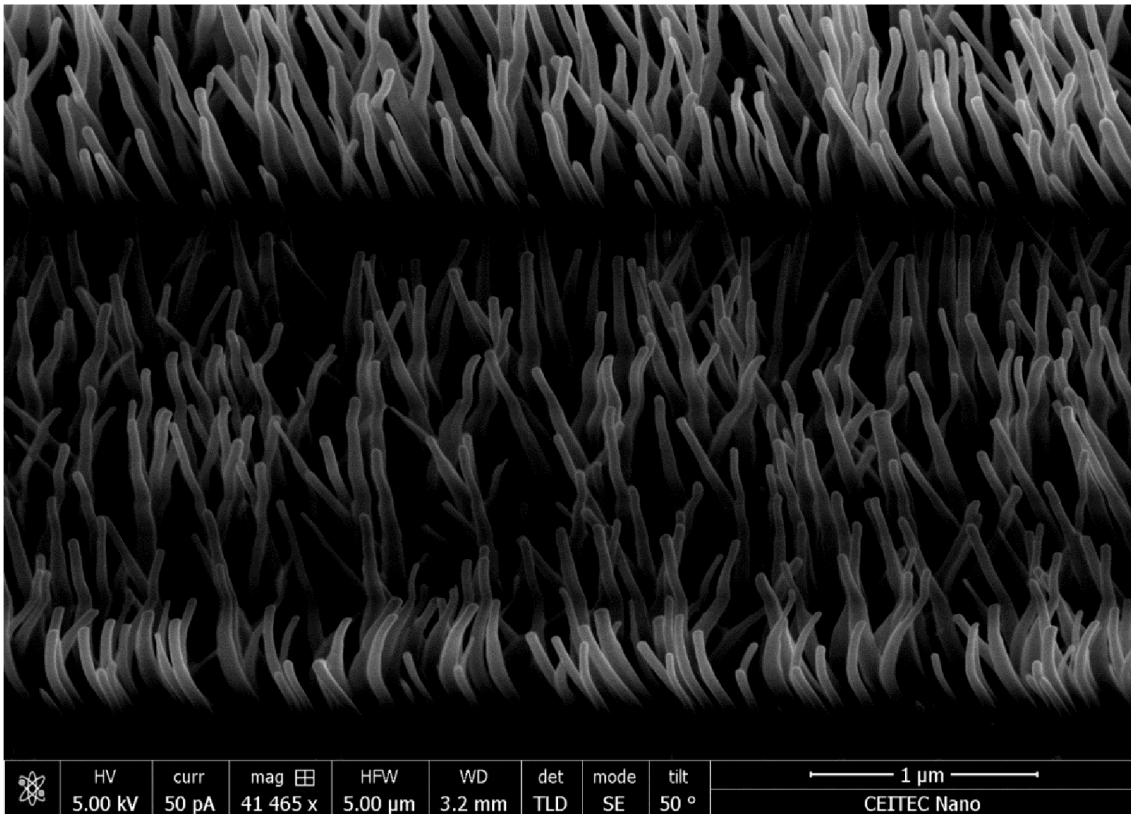
Fig. 67: Pick one: a) Blurry sight of the author. b) Charging effects in the microscope. c) Do they really grow like this?

Fig. 68: A lid of the Zn effusion cell blocked with zinc deposits.

References

1. **Hayden, O. et al.** Semiconductor nanowire devices. *Nano Today.* 2008, Vol. 3, 5-6, p. 12. https://doi.org/10.1016/S1748-0132(08)70061-6.

2. **Chou, L.-W. et al.** Optically Abrupt Localized Surface Plasmon Resonances in Si Nanowires by Mitigation of Carrier Density Gradients. *ACS Nano.* 2015, Vol. 9, 2, p. 1250. https://doi.org/10.1021/nn504974z.

3. **Naik, V. G. et al.** Alternative Plasmonic Materials: Beyond Gold and Silver. *Advanced Materials.* 2013, Vol. 25, 24, p. 3264. https://doi.org/10.1002/adma.201205076.
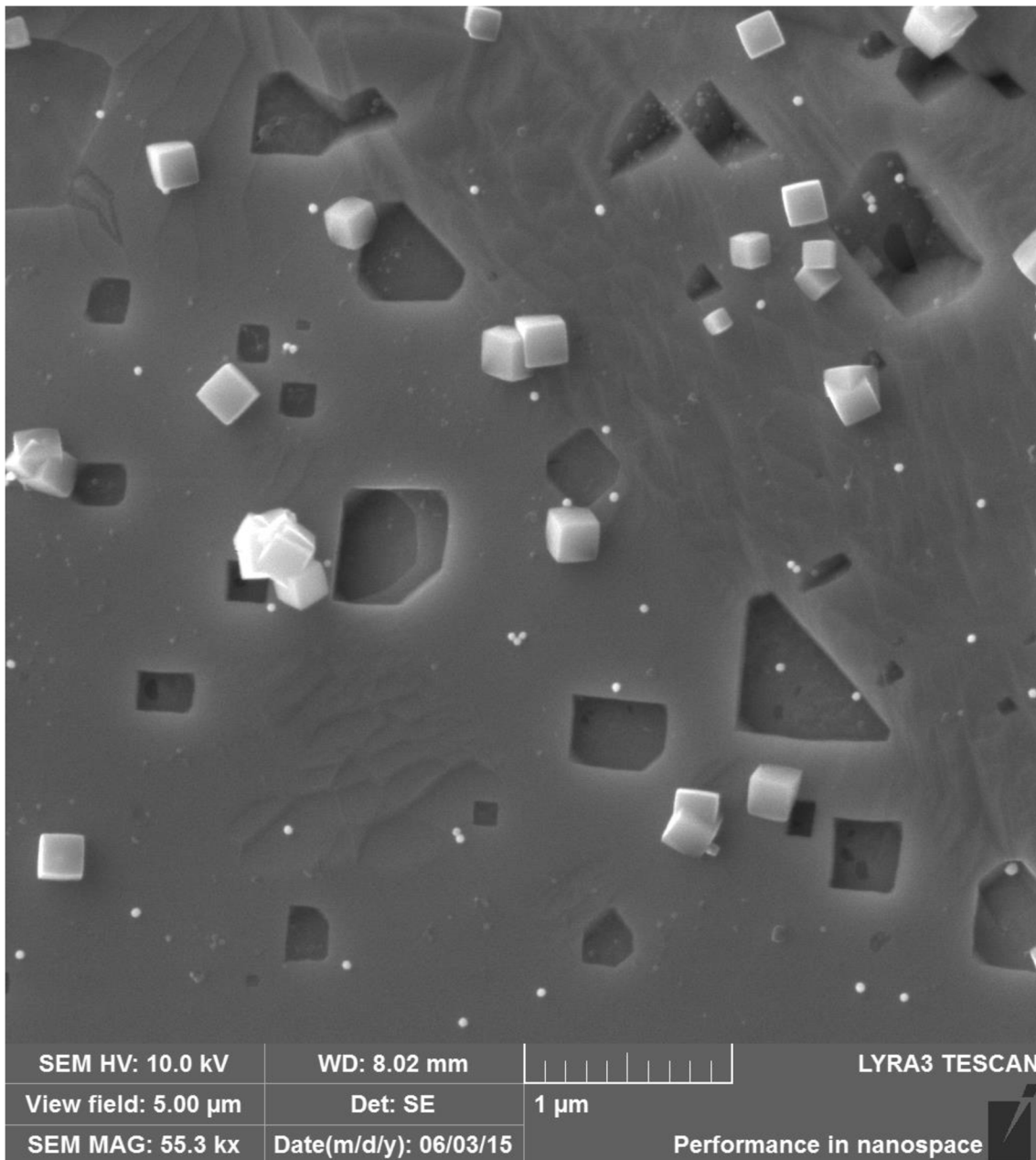
4. **Khurgin, J. and Boltasseva, A.** Reflecting upon the losses in plasmonics and metamaterials. *MRS Bulletin.* 2012, Vol. 37, 8, p. 768. https://doi.org/10.1557/mrs.2012.173.

5. **Amit, I. et al.** Spatially Resolved Correlation of Active and Total Doping Concentrations in VLS Grown Nanowires. *Nano Lett.* 2013, Vol. 13, 6, p. 2598. https://doi.org/10.1021/nl4007062.

6. **Perea, D. E. at al.** Direct measurement of dopant distribution in an individual vapour-liquid-solid nanowire. *Nature Nanotechnology.* 2009, Vol. 4, p. 315. https://doi.org/10.1038/nnano.2009.51.

7. **Connel, J. G. et al.** Identification of an intrinsic source of doping inhomogeneity in vapor-liquid-solid-grown nanowires. *Nano Lett.* 2013, Vol. 13, 1, p. 199. https://doi.org/10.1021/nl3038695.

8. **Erwin, S. et al.** Doping semiconductor nanocrystals. *Nature.* 2005, Vol. 436, p. 91. https://doi.org/10.1038/nature03832.

9. **Moutanabbir, O. et al.** Colossal injection of catalyst atoms into silicon nanowires. *Nature.* 2013, Vol. 496, p. 78. https://doi.org/10.1038/nature11999.

10. **Chen, W. et al.** Incorporation and redistribution of impurities into silicon nanowires during metal-particle-assisted growth. *Nature Communications.* 2014, Vol. 5, p. 1. https://doi.org/10.1038/ncomms5134.

11. **Kolíbal, M. et al.** In-situ observation of <110> oriented Ge nanowire growth and associated collector droplet behavior. *Appl. Phys. Lett.* 2011, Vol. 99, 14, p. 143113. https://doi.org/10.1063/1.3647774.

12. **Kolíbal, M. et al.** Controlled faceting in <110> germanium nanowire growth by switching between vapor-liquid-solid and vapor-solid-solid growth. *Appl. Phys. Lett.* 2012, Vol. 100, 20, p. 203102. https://doi.org/10.1063/1.4714765.

13. **Kolíbal, M. et al.** Real-Time Observation of Collector Droplet Oscillations during Growth of Straight Nanowires. *Nano Lett.* 2014, Vol. 14, 4, p. 1756. https://doi.org/10.1021/nl404159x.

14. **Wagner, R. S. and Ellis, W. C.** Vapor-liquid-solid mechanism of single crystal growth. *Appl. Phys. Lett.* 1964, Vol. 4, 5, p. 89. https://doi.org/10.1063/1.1753975.

15. **Wacaser, B. A. et al.** Preferential Interface Nucleation: An expansion of the VLS growth mechanism for nanowires. *Adv. Mater.* 2009, Vol. 21, 2, p. 153. https://doi.org/10.1002/adma.200800440.

16. **Sutter, E. and Sutter, P.** Phase diagram of nanoscale alloy particles used for vapor-liquid-solid growth of semiconductor nanowires. *Nano Lett.* 2008, Vol. 8, 2, p. 411. https://doi.org/10.1021/nl0719630.

17. **Wen, C.-Y. et al.** Step-flow kinetics in nanowire growth. *Phys. Rev. Lett.* 2010, Vol. 105, 19, p. 195502. https://doi.org/10.1103/PhysRevLett.105.195502.

18. **Jacobsson, D. et al.** Interface dynamics and crystal phase switching in GaAs nanowires. *Nature.* 2016, Vol. 531, p. 317. https://doi.org/10.1038/nature17148.

19. **Ross, F. M.** Controlling nanowire structures through real time growth studies. *Rep. Prog. Phys.* 2010, Vol. 73, 11, p. 114501. https://doi.org/10.1088/0034-4885/73/11/114501.

20. **Maliakkal, C. B. et al.** Independent control of nucleation and layer growth in nanowires. *ACS Nano.* 2020, Vol. 14, 4, p. 3868. https://doi.org/10.1021/acsnano.9b09816.

21. **Fortuna, S. A. and Li, X.** Metal-catalyzed semiconductor nanowires: A review on the control of growth directions. *Semicond. Sci. Technol.* 2010, Vol. 25, p. 024005. https://doi.org/10.1088/0268-1242/25/2/024005.

22. **Kamins, T. I. et al.** Growth and structure of chemically vapor deposited Ge nanowires on Si substrates. *Nano Lett.* 2004, Vol. 4, 3, p. 503. https://doi.org/10.1021/nl035166n.

23. **Adhikari, H. et al.** Germanium nanowire epitaxy: Shape and orientation control. *Nano Lett.* 2006, Vol. 6, 2, p. 318. https://doi.org/10.1021/nl052231f.

24. **Jagannathan, H. et al.** Nature of germanium nanowire heteroepitaxy on silicon substrates. *J. Appl. Phys.* 2006, Vol. 100, 2, p. 024318. https://doi.org/10.1063/1.2219007.

25. **Schmidt, V. et al.** Diameter-dependent growth direction of epitaxial silicon nanowires. *Nano Lett.* 2005, Vol. 5, 5, p. 931. https://doi.org/10.1021/nl050462g.

26. **Howe, J. M. and Saka, H.** In-situ transmission electron microscopy studies of the solid-liquid interface. *MRS Bulletin.* 2004, Vol. 29, p. 951. https://doi.org/10.1557/mrs2004.266.

27. **Wang, J. et al.** Reversible switching of InP nanowire growth direction by catalyst engineering. *Nano Lett.* 2013, Vol. 13, 8, p. 3802. https://doi.org/10.1021/nl401767b.

28. **Kuykendall, T. R. et al.** Catalyst-directed crystallographic orientation control of GaN nanowire growth. *Nano Lett.* 2014, Vol. 14, 12, p. 6767. https://doi.org/10.1021/nl502079v.

29. **Musin, I. R. and Filler, M. A.** Chemical control of semiconductor nanowire kinking and superstructure. *Nano Lett.* 2012, Vol. 12, 7, p. 3363. https://doi.org/10.1021/nl204065p.

30. **Kodambaka, S. et al.** Control of Si nanowire growth by oxygen. *Nano Lett.* 2006, Vol. 6, 6, p. 1292. https://doi.org/10.1021/nl060059p.

31. **Shin, N. and Filler, M. A.** Controlling silicon nanowire growth direction via surface chemistry. *Nano Lett.* 2012, Vol. 12, 6, p. 2865. https://doi.org/10.1021/nl300461a.

32. **Wu, Y. et al.** Controlled growth and structures of molecular-scale silicon nanowires. *Nano Lett.* 2004, Vol. 4, 3, p. 433. https://doi.org/10.1021/nl035162i.

33. **Yang, Z.-X. et al.** Approaching the Hole Mobility Limit of GaSb Nanowires. *ACS Nano.* 2015, Vol. 9, 9, p. 9268. https://doi.org/10.1021/acsnano.5b04152.

34. **Cai, Y. et al.** The size-dependent growth direction of ZnSe nanowires. *Adv. Mater.* 2006, Vol. 18, 1, p. 109. https://doi.org/10.1002/adma.200500822.

35. **Madras, P. et al.** Kinetically induced kinking of vapor–liquid–solid grown epitaxial Si nanowires. *Nano Lett.* 2009, Vol. 9, 11, p. 3826. https://doi.org/10.1021/nl902013g.

36. **Adhikari, H. et al.** Metastability of Au-Ge liquid nanocatalysts: Ge vapor-liquid-solid nanowire growth far below the bulk eutectic temperature. *ACS Nano.* 2007, Vol. 1, 5, p. 415. https://doi.org/10.1021/nn7001486.

37. **Hanrath, T. and Korgel, B. A.** Crystallography and surface faceting of germanium nanowires. *Small.* 2005, Vol. 1, 7, p. 717. https://doi.org/10.1002/smll.200500033.

38. **Gamalski, A. D. et al.** Cyclic supersaturation and triple phase boundary dynamics in germanium nanowire growth. *J. Phys. Chem. C.* 2011, Vol. 115, 11, p. 4413. https://doi.org/10.1021/jp1095882.

39. **Dayeh, S. A. and Picraux, S.T.** Direct observation of nanoscale size effects in Ge semiconductor nanowire growth. *Nano Lett.* 2010, Vol. 10, 10, p. 4032. https://doi.org/10.1021/nl1019722.

40. **Dick, K. A. and Caroff, P.** Metal-seeded growth of III–V semiconductor nanowires: towards gold-free synthesis. *Nanoscale.* 2014, Vol. 6, p. 3006. https://doi.org/10.1039/C3NR06692D.

41. **Zhuang, Q. D. et al.** Sb-induced phase control of InAsSb nanowires grown by molecular beam epitaxy. *Nano Lett.* 2015, Vol. 15, 2, p. 1109. https://doi.org/10.1021/nl5040946.

42. **Schönherr, P. et al.** Vapour-liquid-solid growth of ternary Bi2Se2Te nanowires. *Nanoscale Research Letters.* 2014, Vol. 9, p. 127. https://doi.org/10.1186/1556-276X-9-127.

43. **Zhang, Z. et al.** Controlling the growth mechanism of ZnO nanowires by selecting catalysts. *J. Phys. Chem. C.* 2007, Vol. 111, 47, p. 17500. https://doi.org/10.1021/jp075296a.

44. **Sze, S. M. and Irvin, J. C.** Resistivity, mobility and impurity levels in GaAs, Ge, and Si at 300°K. *Solid-State Electronics.* 1968, Vol. 11, 6, p. 599. https://doi.org/10.1016/0038-1101(68)90012-9.

45. **Moutanabbir, O. et al.** Atomically smooth p-doped Si NWs catalysed by Al at low temperature. *ACS Nano.* 2011, Vol. 5, 2, p. 1313. https://doi.org/10.1021/nn1030274.

46. **Wang, Y. et al.** Epitaxial growth of silicon nanowires using an aluminum catalyst. *Nature Nanotechnology.* 2006, Vol. 1, p. 186. https://doi.org/10.1038/nnano.2006.133.

47. **Wacaser, B. A. et al.** Growth system, structure and doping of Al seeded epitaxial Si NWs. *Nano Lett.* 2009, Vol. 9, 9, p. 3296. https://doi.org/10.1021/nl9015792.

48. **Choi, S.-Y. et al.** Growth and electrical properties of Al-catalyzed Si NWs. *Appl. Phys. Lett.* 2011, Vol. 98, 3, p. 033108. https://doi.org/10.1063/1.3544933.

49. **Kohen, D. et al.** Aluminum catalyzed growth of silicon nanowires: Al atom location and the influence of silicon precursor pressure on the morphology. *J. Cryst. Growth.* 2012, Vol. 341, 1, p. 12. https://doi.org/10.1016/j.jcrysgro.2011.12.057.

50. **Ke, Y. et al.** Carrier gas effects on aluminum-catalyzed nanowire growth. *Nanotechnology.* 2016, Vol. 27, 13, p. 135605. https://doi.org/10.1088/0957-4484/27/13/135605.

51. **Yu, L. et al.** Stability and evolution of low-surface-tension metal catalyzed growth of silicon nanowires. *Appl. Phys. Lett.* 2011, Vol. 98, 12, p. 123113. https://doi.org/10.1063/1.3569817.

52. **Bianco, G. V. et al.** Plasma-plasmonics synergy in the Ga-catalyzed growth of Si-nanowires. *Mat. Sci. Eng. B.* 2012, Vol. 177, 10, p. 700. https://doi.org/10.1016/j.mseb.2011.09.030.

53. **Iacopi, F. et al.** CVD growth of Si nanowires with low melting point metal catalysts In and Al. *Nanotechnology.* 2007, Vol. 18, 50, p. 505307. https://doi.org/10.1088/0957-4484/18/50/505307.

54. **Zardo, I. et al.** Gallium assisted plasma enhanced chemical vapor deposition of silicon nanowires. *Nanotechnology.* 2009, Vol. 20, 15, p. 155602. https://doi.org/10.1088/0957-4484/20/15/155602.

55. **Conesa-Boj, S. et al.** Defect formation in Ga-catalyzed silicon nanowires. *Cryst. Growth Des.* 2010, Vol. 10, 4, p. 1534. https://doi.org/10.1021/cg900741y.

56. **Yu, L. et al.** Plasma enhanced low temperature growth of silicon nanowires and hierarchical structures by using tin and indium catalysts. *Nanotechnology.* 2009, Vol. 20, 22, p. 225604. https://doi.org/10.1088/0957-4484/20/22/225604.

57. **Sun, X. et al.** Synthesis of Ge NWs on insulator catalyzed by In or Sb. *J. Vac. Sci. Technol. B.* 2007, Vol. 25, 2, p. 415. https://doi.org/10.1116/1.2713407.

58. **Xiang, Y. et al.** Synthesis parameter space of bismuth catalyzed germanium nanowires. *Appl. Phys. Lett.* 2009, Vol. 94, 16, p. 163101. https://doi.org/10.1063/1.3116625.

59. **Yan, C. and Lee, P. S.** Bismuth-catalyzed growth of germanium nanowires in vapor phase. *J. Phys. Chem. C.* 2009, Vol. 113, 6, p. 2208. https://doi.org/10.1021/jp8111414.

60. **Yu, L. et al.** Bismuth-catalyzed and doped silicon nanowires for one-pump-down fabrication of radial junction solar cells. *Nano Lett.* 2012, Vol. 12, 8, p. 4153. https://doi.org/10.1021/nl3017187.

61. **Gamalski, A. D. et al.** Catalyst composition and impurity-dependent kinetics of nanowire heteroepitaxy. *ACS Nano.* 2013, Vol. 7, 9, p. 7689. https://doi.org/10.1021/nn402208p.

62. **Lugstein, A. et al.** GaAu alloy catalyst for single crystal Si NW epitaxy. *Appl. Phys. Lett.* 2007, Vol. 90, 2, p. 023109. https://doi.org/10.1063/1.2431468.

63. **Perea, D. E. et al.** Controlling heterojunction abruptness in VLS grown semiconductor NWs via in situ catalyst alloying. *Nano Lett.* 2011, Vol. 11, 8, p. 3117. https://doi.org/10.1021/nl201124y.

64. **Wen, C.-Y. et al.** Periodically changing morphology of the growth interface in Si, Ge and GaP NWs. *Phys. Rev. Lett.* 2011, Vol. 107, 2, p. 025503. https://doi.org/10.1103/PhysRevLett.107.025503.

65. **Han, N. et al.** Manipulated growth of GaAs nanowires. *Cryst. Growth Des.* 2012, Vol. 12, 12, p. 6243. https://doi.org/10.1021/cg301452d.

66. **Ko, Y.-D. et al.** Sn-induced low-temperature growth of Ge nanowire electrodes with a large. *Nanoscale.* 2011, Vol. 3, 8, p. 3371. https://doi.org/10.1039/C1NR10471C.

67. **Sun, Y.-L. et al.** Au–Sn catalyzed growth of Ge1–xSnx nanowires: Growth direction, crystallinity, and Sn incorporation. *Nano Lett.* 2019, Vol. 19, 9, p. 6270. https://doi.org/10.1021/acs.nanolett.9b02395.

68. **Wen, C.-Y. et al.** Formation of compositionally abrupt axial heterojunctions in silicon-germanium nanowires. *Science.* 2009, Vol. 326, 5957, p. 1247. https://doi.org/10.1126/science.1178606.

69. **Allen, J. E. et al.** High-resolution detection of Au catalyst atoms in Si nanowires. *Nature Nanotechnology.* 2008, Vol. 3, p. 168. https://doi.org/10.1038/nnano.2008.5.

70. **McIntyre, P. C. and Fontcuberta i Morral, A.** Semiconductor nanowires: to grow or not to grow? *Materials Today Nano.* 2020, Vol. 9, p. 100058. https://doi.org/10.1016/j.mtnano.2019.100058.

71. **Biswas, S. et al.** Non-equilibrium induction of tin in germanium: towards direct bandgap $Ge_{1-x}Sn_x$ nanowires. *Nature Communications.* 2016, Vol. 7, p. 11405. https://doi.org/10.1038/ncomms11405.

72. **Seifner, M. S. et al.** Drastic changes in material composition and electrical properties of gallium-seeded germanium nanowires. *Cryst. Growth Des.* 2019, Vol. 19, 5, p. 2531. https://doi.org/10.1021/acs.cgd.9b00210.

73. **Seifner, M. S. et al.** Direct Synthesis of Hyperdoped Germanium Nanowires. *ACS Nano.* 2018, Vol. 12, 2, p. 1236. https://doi.org/10.1021/acsnano.7b07248.

74. **Sivaram, S. V. et al.** Direct observation of transient surface species during Ge nanowire growth and their influence on growth stability. *J. Am. Chem. Soc.* 2015, Vol. 137, 31, p. 9861. https://doi.org/10.1021/jacs.5b03818.

75. **Gamalski, A. D. et al.** The Role of Surface Passivation in Controlling Ge Nanowire Faceting. *Nano Lett.* 2015, Vol. 15, 12, p. 8211. https://doi.org/10.1021/acs.nanolett.5b03722.

76. **Nebol'sin, V. A. and Shchetinin, A. A.** Role of surface energy in the Vapor-Liquid-Solid growth of silicon. *Inorganic Materials.* 2003, Vol. 39, 9, p. 899. https://doi.org/10.1023/A:1025588601262.

77. **Kolíbal, M. et al.** The Synergic Effect of Atomic Hydrogen Adsorption and Catalyst Spreading on Ge Nanowire Growth Orientation and Kinking. *Nano Lett.* 2016, Vol. 16, 8, p. 4880. https://doi.org/10.1021/acs.nanolett.6b01352.

78. **Briggs, D. and Grant, J. T.** *Surface Analysis by Auger and X-ray Photoelectron Spectroscopy.* s.l. : IM Publications and SurfaceSpectra Limited, 2003. ISBN: 1-901019-04-7.

79. **Porret, C. et al.** Importance of kinetics effects in the growth of germanium nanowires by vapour-liquid-solid Molecular Beam Epitaxy. *J. Cryst. Growth.* 2011, Vol. 323, 1, p. 334. https://doi.org/10.1016/j.jcrysgro.2010.11.056.

80. **Dubrovskii, V. G. et al.** Diffusion-controlled growth of semiconductor nanowires: Vapor pressure versus high vacuum deposition. *Surface Science.* 2007, Vol. 601, 18, p. 4395. https://doi.org/10.1016/j.susc.2007.04.122.

81. **Ross, F. M. et al.** Sawtooth faceting in silicon nanowires. *Phys. Rev. Lett.* 2005, Vol. 95, 14, p. 146104. https://doi.org/10.1103/PhysRevLett.95.146104.

82. **Ryu, S.-G. et al** On demand shape-selective integration of individual vertical germanium nanowires on a Si(111) substrate via laser-localized heating. *ACS Nano.* 2013, Vol. 7, 3, p. 2090. https://doi.org/10.1021/nn400186c.

83. **Cho, H. S. and Kamins, T. I.** In situ control of Au-catalyzed chemical vapor deposited (CVD) Ge nanocone morphology by growth temperature variation. *J. Cryst. Growth.* 2010, Vol. 312, 16-17, p. 2494. https://doi.org/10.1016/j.jcrysgro.2010.05.035.

84. **Wiethoff, C. et al.** Au stabilization and coverage of sawtooth facets on Si nanowires grown by vapor–liquid–solid epitaxy. *Nano Lett.* 2008, Vol. 8, 9, p. 3065. https://doi.org/10.1021/nl801146q.

85. **Hannon, J. B. et al.** The influence of the surface migration of gold on the growth of silicon nanowires. *Nature.* 2006, Vol. 440, p. 69. https://doi.org/10.1038/nature04574.

86. **Stekolnikov, A. A. and Bechstedt, F.** Shape of free and constrained group-IV crystallites: Influence of surface energies. *Phys. Rev. B.* 2005, Vol. 72, 12, p. 125326. https://doi.org/10.1103/PhysRevB.72.125326.

87. **Su, C. et al.** Interaction of atomic hydrogen with a Ge(111) surface: low-energy electron diffraction and surface Raman studies. *Surface Science.* 2000, Vol. 445, 2-3, p. 139. https://doi.org/10.1016/S0039-6028(99)00991-7.

88. **Akazawa, H. J.** Hydrogen induced roughening and smoothing in surface morphology during synchrotron-radiation-excited GeH4-source homoepitaxy on Ge(001). *J. Appl. Phys.* 2006, Vol. 99, 10, p. 103505. https://doi.org/10.1063/1.2194232.

89. **Scholz, S. M. et al.** The clean and hydrogenated Ge(113) surface studied by angle-resolved photo-electron spectroscopy. *Surface Science.* 1995, Vols. 331-333, p. 402. https://doi.org/10.1016/0039-6028(95)00297-9.

90. **Kolíbal, M. et al.** Catalyst–substrate interaction and growth delay in vapor–liquid–solid nanowire growth. *Nanotechnology.* 2018, Vol. 29, 20, p. 205603. https://doi.org/10.1088/1361-6528/aab474.

91. **Kaufman, S. M. and Whalen, T. J.** The surface tension of liquid gold, liquid tin, and liquid gold-tin binary solutions. *Acta Metallurgica.* 1965, Vol. 13, 7, p. 797. https://doi.org/10.1016/0001-6160(65)90144-6.

92. **Aqra, F. and Ayyad, A.** Surface tension of liquid alkali, alkaline, and main group metals: Theoretical treatment and relationship investigations. *Metallurgical and Materials Transactions A.* 2011, Vol. 42, p. 2680. https://doi.org/10.1007/s11661-011-0686-z.

93. **Elliott, R. P. and Shunk, F. A.** The Au–Ga (Gold-Gallium) system. *Bulletin of Alloy Phase Diagrams.* 1981, Vol. 2, 3, p. 356. https://doi.org/10.1007/BF02868293.

94. **Janotti, A. and Van de Walle, C. G.** Fundamentals of zinc oxide as a semiconductor. *Rep. Prog. Phys.* 2009, Vol. 72, 12, p. 126501. https://doi.org/10.1088/0034-4885/72/12/126501.

95. **Ellmer, K. and Bikowski, A.** Intrinsic and extrinsic doping of ZnO and ZnO alloys. *J. Phys. D: Appl. Phys.* 2016, Vol. 49, 41, p. 413002. https://doi.org/10.1088/0022-3727/49/41/413002.

96. **Mauit, O. et al.** Growth of ZnO:Al by atomic layer deposition: Deconvoluting the contribution of hydrogen interstitials and crystallographic texture on the conductivity. *Thin Solid Films.* 2019, Vol. 690, p. 137533. https://doi.org/10.1016/j.tsf.2019.137533.

97. **Li, F. et al.** High-mobility In and Ga co-doped ZnO nanowires for high-performance transistors and ultraviolet photodetectors. *Nanoscale.* 2020, Vol. 12, 30, p. 16153. https://doi.org/10.1039/D0NR03740K.

98. **Agrawal, A. et al.** Control of localized surface plasmon resonances in metal oxide nanocrystals. *Annu. Rev. Mater. Res.* 2017, Vol. 47, p. 1. https://doi.org/10.1146/annurev-matsci-070616-124259.

99. **Wang, Z. L.** ZnO nanowire and nanobelt platform for nanotechnology. *Materials Science and Engineering R.* 2009, Vol. 64, 3-4, p. 33. https://doi.org/10.1016/j.mser.2009.02.001.

100. **Chen, Y. et al.** Plasma assisted molecular beam epitaxy of ZnO on c-plane sapphire: Growth and characterization. *J. Appl. Phys.* 1998, Vol. 84, 7, p. 3912. https://doi.org/10.1063/1.368595.

101. **Zúñiga-Pérez, J. et al.** Polarity in GaN and ZnO: Theory, measurement, growth, and devices. *Appl. Phys. Rev.* 2016, Vol. 3, 4, p. 041303. https://doi.org/10.1063/1.4963919.

102. **Morkoç, H. and Özgür, Ü.** *Zinc Oxide: Fundamentals, Materials and Device Technology.* s.l. : Wiley-VCH, 2009. ISBN: 978-3-527-40813-9.

103. [Online] [Cited: 29 April 2020] http://www.materials.ac.uk/elearning/matter/crystallography/indexingdirectionsandplanes/indexing-of-hexagonal-systems.html.

104. **Lai, E. et al.** Vertical nanowire array-based light emitting diodes. *Nano Research.* 2008, Vol. 1, p. 123. https://doi.org/10.1007/s12274-008-8017-4.

105. **Chu, S. et al.** Electrically pumped waveguide lasing from ZnO nanowires. *Nature Nanotechnology.* 2011, Vol. 6, p. 506. https://doi.org/10.1038/nnano.2011.97.

106. **Kim, K.-K. et al.** Realization of p-type ZnO thin films via phosphorus doping and thermal activation of the dopant. *Appl. Phys. Lett.* 2003, Vol. 83, 1, p. 63. https://doi.org/10.1063/1.1591064.

107. **Brauer, G. et al.** Activities towards p-type doping of ZnO. *J. Phys.: Conf. Ser.* 2011, Vol. 265, p. 012002. https://doi.org/10.1088/1742-6596/265/1/012002.

108. **Sun, F. et al.** On the origin of intrinsic donors in ZnO. *Applied Surface Science.* 2010, Vol. 256, 11, p. 3390. https://doi.org/10.1016/j.apsusc.2009.12.040.

109. **Liu, L. et al.** Oxygen vacancies: The origin of n-type conductivity in ZnO. *Phys. Rev. B.* 2016, Vol. 93, 23, p. 235305. https://doi.org/10.1103/PhysRevB.93.235305.

110. **Tang, K. et al.** Recent progress of the native defects and p-type doping of zinc oxide. *Chin. Phys. B.* 2017, Vol. 26, 4, p. 047702. https://doi.org/10.1088/1674-1056/26/4/047702.

111. **Borysiewicz, M. A.** ZnO as a functional material, a review. *Crystals.* 2019, Vol. 9, 10, p. 505. https://doi.org/10.3390/cryst9100505.

112. **Look, D. C. et al.** Characterization of homoepitaxial p-type ZnO grown by molecular beam epitaxy. *Appl. Phys. Lett.* 2002, Vol. 81, 10, p. 1830. https://doi.org/10.1063/1.1504875.

113. **Villafuerte, J. et al.** Zinc vacancy–hydrogen complexes as major defects in ZnO nanowires grown by chemical bath deposition. *J. Phys. Chem. C.* 2020, Vol. 124, 30, p. 16652. https://doi.org/10.1021/acs.jpcc.0c04264.

114. **Kim, K. et al.** Fabrication and characterization of Ga-doped ZnO nanowire gas sensor for the detection of CO. *Thin Solid Films.* 2009, Vol. 518, 4, p. 1190. https://doi.org/10.1016/j.tsf.2009.03.229.

115. **Pan, Z. et al.** Properties of fluorine and tin co-doped ZnO thin films deposited by sol–gel method. *Journal of Alloys and Compounds.* 2013, Vol. 576, p. 31. http://dx.doi.org/10.1016/j.jallcom.2013.04.132.

116. **Namgung, G. et al.** Diffusion-driven Al-doping of ZnO nanorods and stretchable gas sensors made of doped ZnO nanorods/Ag nanowires bilayers. *ACS Appl. Mater. Interfaces.* 2019, Vol. 11, 1, p. 1411. https://doi.org/10.1021/acsami.8b17336.

117. **Zhou, H. et al.** Ordered n-type ZnO nanorod arrays. *Appl. Phys. Lett.* 2008, Vol. 92, 13, p. 132112. https://doi.org/10.1063/1.2907197.

118. **Yuan, G. D. et al.** p-type ZnO nanowire arrays. *Nano Lett.* 2008, Vol. 8, 8, p. 2591. https://doi.org/10.1021/nl073022t.

119. **Brillson, L. J. and Lu, Y.** ZnO Schottky barriers and Ohmic contacts. *J. Appl. Phys.* 2011, Vol. 109, 12, p. 121301. https://doi.org/10.1063/1.3581173.

120. **Schmidt, O. et al.** Effects of an electrically conducting layer at the zinc oxide surface. *Japanese Journal of Applied Physics.* 2005, Vol. 44, 10, p. 7271. https://doi.org/10.1143/JJAP.44.7271.

121. **Look, D. C.** Quantitative analysis of surface donors in ZnO. *Surface Science.* 2007, Vol. 601, 23, p. 5315. https://doi.org/10.1016/j.susc.2007.09.030.

122. **Djurišić, A. B. et al.** ZnO nanostructures for optoelectronics: Material properties and device applications. *Progress in Quantum Electronics.* 2010, Vol. 34, 4. https://doi.org/10.1016/j.pquantelec.2010.04.001.

123. **Heo, Y. W. et al.** Electrical transport properties of single ZnO nanorods. *Appl. Phys. Lett.* 2004, Vol. 85, 11, p. 2002. https://doi.org/10.1063/1.1792373.

124. **Cossuet, T. et al.** Well-ordered ZnO nanowires with controllable inclination on semipolar ZnO surfaces by chemical bath deposition. *Nanotechnology.* 2018, Vol. 29, 47, p. 475601. https://doi.org/10.1088/1361-6528/aadf62.

125. **Galdámez-Martinez, A.** Photoluminescence of ZnO Nanowires: A review. *Nanomaterials.* 2020, Vol. 10, 5, p. 857. https://doi.org/10.3390/nano10050857.

126. **Lavrov, E. V. et al.** Identification of two hydrogen donors in ZnO. *Phys. Rev. B.* 2009, Vol. 79, 16, p. 165210. https://doi.org/10.1103/PhysRevB.79.165210.

127. **Hasuike, N. et al.** Raman scattering studies on ZnO doped with Ga and N (codoping), and magnetic impurities. *J. Phys.: Condens. Matter.* 2004, Vol. 16, 48, p. S5807. https://doi.org/10.1088/0953-8984/16/48/053.

128. **Escobedo-Morales, A. and Pal, U.** Effect of In, Sb and Ga doping on the structure and vibrational modes of hydrothermally grown ZnO nanostructures. *Current Applied Physics.* 2011, Vol. 11, 3, p. 525. https://doi.org/10.1016/j.cap.2010.09.007.

129. **Verrier, C. et al.** Tunable morphology and doping of ZnO nanowires by chemical bath deposition using aluminum nitrate. *J. Phys. Chem. C.* 2017, Vol. 121, 6, p. 3573. https://doi.org/10.1021/acs.jpcc.6b11104.

130. **Bundesmann, C. et al.** Raman scattering in ZnO thin films doped with Fe, Sb, Al, Ga, and Li. *Appl. Phys. Lett.* 2003, Vol. 83, 10, p. 1974. https://doi.org/10.1063/1.1609251.

131. **Milano, G. et al.** Tuning ZnO nanowire dissolution by electron beam modification of surface wetting properties. *J. Phys. Chem. C.* 2018, Vol. 122, 14, p. 8011. https://doi.org/10.1021/acs.jpcc.8b01158.

132. **Gabás, M. et al.** Differences in n-type doping efficiency between Al- and Ga-ZnO films. *J. Appl. Phys.* 2013, Vol. 113, 16, p. 163709. https://doi.org/10.1063/1.4803063.

133. **Pineda-Hernández, G. et al.** Morphology evolution of hydrothermally grown ZnO nanostructures on gallium doping and their defect structures. *Materials Chemistry and Physics.* 2012, Vol. 135, 2-3, p. 810. https://doi.org/10.1016/j.matchemphys.2012.05.062.

134. **Sky, T. N. et al.** Gallium diffusion in zinc oxide via the paired dopant-vacancy mechanism. *J. Appl. Phys.* 2018, Vol. 123, 5, p. 055701. https://doi.org/10.1063/1.5000123.

135. **Chen, C.-Y. et al.** Low resistivity and low compensation ratio Ga-doped ZnO films grown by plasma-assisted molecular beam epitaxy. *J. Cryst. Growth.* 2015, Vol. 425, p. 216. https://doi.org/10.1016/j.jcrysgro.2015.02.034.

136. **Ha, B. et al.** Photoluminescence of ZnO nanowires dependent on O2 and Ar annealing. *Journal of Physics and Chemistry of Solids.* 2008, Vol. 69, 10, p. 2453. https://doi.org/10.1016/j.jpcs.2008.04.041.

137. **Park, S.-M. et al.** Effects of substrate temperature on the properties of Ga-doped ZnO by pulsed laser deposition. *Thin Solid Films.* 2006, Vol. 513, 1-2, p. 90. https://doi.org/10.1016/j.tsf.2006.01.051.

138. **Das, D. and Mondala, P.** Low temperature grown ZnO:Ga films with predominant c-axis orientation in wurtzite structure demonstrating high conductance, transmittance and photoluminescence. *RSC Adv.* 2016, Vol. 6, 8, p. 6144. https://doi.org/10.1039/C5RA22288E.

139. **Fan, J. C. C. and Goodenough, J. B.** X-ray photoemission spectroscopy studies of Sn-doped indium-oxide films. *J. Appl. Phys.* 1977, Vol. 48, 8, p. 3524. https://doi.org/10.1063/1.324149.

140. **Vallejos, S. et al.** ZnO rods with exposed {100} facets grown via a self-catalyzed vapor–solid mechanism and their photocatalytic and gas sensing properties. *ACS Appl. Mater. Interfaces.* 2016, Vol. 8, 48, p. 33335. https://doi.org/10.1021/acsami.6b12992.

141. **Vallejos, S. et al.** Tuning of the humidity-interference in gas sensitive columnar ZnO structures. *Proceedings.* 2017, Vol. 1, 4, p. 417. https://doi.org/10.3390/proceedings1040417.

142. **Mikula, M.** Příprava nanodrátů pro fotoniku. 2019. Brno: Vysoké učení technické v Brně, Fakulta strojního inženýrství. (Diploma thesis. Supervisor: doc. Ing. Miroslav Kolíbal, PhD.).

143. **Fedorov, P. P. and Volkov, S. N.** Au–Cu phase diagram. *Russ. J. Inorg. Chem.* 2016, Vol. 61, p. 772. https://doi.org/10.1134/S0036023616060061.

144. **El-Shaer, A. et al.** High-quality ZnO layers grown by MBE on sapphire. *Superlattices and Microstructures.* 2005, Vol. 38, 4-6, p. 265. https://doi.org/10.1016/j.spmi.2005.08.025.

145. **Hesse, R. et al.** Peak shape analysis of core level photoelectron spectra using UNIFIT for WINDOWS. *Fresenius' Journal of Analytical Chemistry.* 1999, Vol. 365, p. 48. https://doi.org/10.1007/s002160051443.

146. **Saint-Exupéry, A.** *Malý princ.* s.l. : Albatros, 1994. ISBN: 80-00-00023-7.

147. **Gao, Y. H. et al.** Synthesis, Raman scattering and defects of β-Ga2O3 nanorods. *Appl. Phys. Lett.* 2002, Vol. 81, 18, p. 2267. https://doi.org/10.1063/1.1507835.

148. **Kumar, S. and Singh, R.** Nanofunctional gallium oxide (Ga2O3) nanowires/nanostructures and their applications in nanodevices. *Phys. Status Solidi RRL.* 2013, Vol. 7, 10, p. 781. https://doi.org/10.1002/pssr.201307253.

149. **Kumar, S. et al.** Study of iron-catalysed growth of β-Ga2O3 nanowires and their detailed characterization using TEM, Raman and cathodoluminescence techniques. *J. Phys. D: Appl. Phys.* 2014, Vol. 47, 43, p. 435101. https://doi.org/10.1088/0022-3727/47/43/435101.

150. **Tak, B. R. et al.** Point defects induced work function modulation of β-Ga2O3. *Applied Surface Science.* 2019, Vol. 465, p. 973. https://doi.org/10.1016/j.apsusc.2018.09.236.

151. **Ma, H.-P. et al.** Precise control of the microstructural, optical, and electrical properties of ultrathin Ga2O3 film through nanomixing with few atom-thick SiO2 interlayer via plasma enhanced atomic layer deposition. *J. Mater. Chem. C.* 2018, Vol. 6, 46, p. 12518. https://doi.org/10.1039/C8TC04335C.

152. **Kumar, R. et al.** Catalyst-free synthesis of a three-dimensional nanoworm-like gallium oxide–graphene nanosheet hybrid structure with enhanced optical properties. *RSC Adv.* 2016, Vol. 6, 21, p. 17669. https://doi.org/10.1039/C5RA24577J.

153. **Song, P. et al.** Self-consistent growth of single-crystalline (-201)β-Ga2O3 nanowires using a flexible GaN seed nanocrystal. *CrystEngComm.* 2017, Vol. 19, 4, p. 625. https://doi.org/10.1039/C6CE02319C.

154. **Hinkle, C. L. et al.** Detection of Ga suboxides and their impact on III-V passivation and Fermi-level pinning. *Appl. Phys. Lett.* 2009, Vol. 94, 16, p. 162101. https://doi.org/10.1063/1.3120546.

155. **Ivanco, J. et al.** Deoxidation of gallium arsenide surface via silicon overlayer: A study on the evolution of the interface state density. *J. Appl. Phys.* 2005, Vol. 97, 7, p. 073712. https://doi.org/10.1063/1.1873037.

156. **Kasap, S. and Capper, P.** *Springer Handbook of Electronic and Photonic Materials.* s.l. : Springer International Publishing, 2017. ISBN: 978-3-319-48931-5.

157. **Wang, D. and Reynolds, N.** Photoluminescence of zinc oxide nanowires: The effect of surface band bending. *ISRN Condensed Matter Physics.* 2012, Vol. 2012, p. 950354. https://doi.org/10.5402/2012/950354.

Author's publications and conference contributions

Publications in impact journals

- Kolíbal M., **Pejchal T.**, Vystavěl T., Šikola T.: The synergic effect of atomic hydrogen adsorption and catalyst spreading on Ge nanowire growth orientation and kinking. *Nano Letters* 2016, vol. 16, 8, p. 4880. [77]

  DOI: 10.1021/acs.nanolett.6b01352

  Impact factor (2016): 12.712

  My contribution:
  I have conducted the nanowire growth experiments in the vacuum chamber connected to the Auger Electron Spectroscopy system (AES). I have analyzed the nanowires with AES and ex-situ SEM and I have evaluated the results. I have been leading the discussions of the results with other authors and I have contributed to writing the manuscript.

- Kolíbal M., **Pejchal T.**, Musálek T., Šikola T.: Catalyst–substrate interaction and growth delay in vapor–liquid–solid nanowire growth. *Nanotechnology* 2018, vol. 29, 20, p. 205603. [90]

  DOI: 10.1088/1361-6528/aab474

  Impact factor (2018): 3.399

  My contribution:
  I have conducted the growth and catalyst-annealing experiments in the vacuum chamber connected to the Auger Electron Spectroscopy system (AES). I have analyzed the samples with AES and ex-situ SEM and I have evaluated the results. I have contributed to the discussions of the results with other authors and to writing the manuscript.

- **Pejchal T.**, Vallejos, S., Bukvišová K., Šikola, T., Kolíbal M.: Ga interaction with ZnO surfaces: diffusion and melt-back etching.

  To be submitted.

  My contribution:
  I have conducted the deposition, annealing and melt-back-etching experiments. I have analyzed the nanowires with SEM and AES, including the real-time imaging. I have evaluated the results including the XPS, TEM and EDS STEM analysis. I have been leading the discussions of the results with other authors and I have contributed to writing the manuscript.

Active conference contributions

- Nanowire Growth Workshop & Nanowires Workshop 2015
  26th – 30th October 2015, Barcelona, Spain

  Pejchal T., Kolíbal M., Šikola T.: *The role of hydrogen in Ge nanowire growth.* Poster presentation.

- NANOCON 2016 – 8th International Conference on Nanomaterials - Research & Application
  19th – 21st October 2016, Brno, Czech Republic

  Pejchal T., Kolíbal M., Vystavěl T., Šikola T.: *The synergic of atomic hydrogen and catalyst spreading on Ge nanowire growth orientation and kinking.* Poster presentation.

- Nanowire Week 2017 – 10th Nanowire Growth Workshop + 9th Nanowires
  29th May – 2nd June 2017, Lund, Sweden

  Pejchal T., Musálek T., Šikola T., Kolíbal M.: *Group-III catalysts: Preparation and Ge nanowire growth.* Poster presentation.

- Austrian MBE Workshop 2017
  28th – 29th September 2017, Vienna, Austria

  Pejchal T., Musálek T., Kachtík L., Šikola T., Kolíbal M.: *MBE-grown Ge nanowires: The co-effect of atomic hydrogen and Au catalyst spreading.* Oral presentation (15 min).

- CEITEC PhD and Postdoc Retreat 2018
  26th – 27th April 2018, Telč, Czech Republic

  Pejchal T., Musálek T., Kachtík L., Šikola T., Kolíbal M.: *Bimetallic catalysts for MBE-grown Ge nanowires.* Poster presentation.

- Nanowire Week 2018
  11th – 15th June 2018, Hamilton, Canada

  Pejchal T., Kachtík L., Musálek T., Šikola T., Kolíbal M.: *Bimetallic catalysts for MBE-grown Ge nanowires.* Poster presentation.

- ICN+T 2018 – International Conference on Nanoscience + Technology
  22nd – 27th July 2018, Brno, Czech Republic

  Pejchal T., Kachtík L., Musálek T., Šikola T., Kolíbal M.: *Bimetallic catalysts for MBE-grown Ge nanowires.* Poster presentation.